Department of Precision and Microsystems Engineering

Contactless Piezo-Magnetic Actuator: Reluctance Tuning as a Novel Alternative to Coils to Reduce Heat Dissipation

Y.J.T. Niessink

Report no	:	2023.102
Coach	:	Dr. S.H. HosseinNia
Professor	:	Dr. S.H. HosseinNia
Specialisation	:	Mechatronic System Design
Type of report	:	MSc Thesis
Date	:	December 11 2023

Delft
University of
Technology

Challenge the future

Contactless Piezo-Magnetic Actuator

Reluctance Tuning as a Novel Alternative to Coils to Reduce Heat Dissipation

by

Yorick J.T. Niessink

to obtain the degree of Master of Science
at the Delft University of Technology,
to be defended publicly on Monday December 11, 2023 at 11:00 AM.

Project Duration:	September 1, 2022 - December 11, 2023
Student number:	5419948

TU Delft

Preface

This thesis is my final report to obtain the degree of Master of Science at the Delft University of Technology with the specialization in Mechatronic System Design. My path in obtaining this degree was different compared to other students. After I obtained my Bachelor of Science in mechanical engineering, I went straight into the industry. I started to work as a project engineer in sustainable energy technology and electrical engineering. However, after 2 years of working full-time, I found myself doubting my future career. Simply said, I wanted to become better at what I like to do. I began to look into Master's degrees and slowly became interested in the High-tech Engineering Master of Delft University. It seemed like the perfect combination of mechanical and electrical engineering. I chose to work part-time and started the mandatory pre-master with much motivation. After one year I finished the pre-master and began to study for the Master's degree. I met interesting and diverse students during the classes, and some even introduced me to additive manufacturing with a simple installation at home. I started to become more independent with a lot more self-confidence. In addition, I now know where to look for information if I miss crucial knowledge. My final project, the master thesis, gave me much more than only the time to dive into a single subject. It allowed me to put all my learned skills into the engineering of a novel actuator. The developed design, with much joy, is now being patented. This is something that I did not see coming at this age and it makes me feel proud of myself. My final message to all students and persons who read this preface is: ”If you want something, go for it. You have to do it yourself, someone else is not going to do it for you.”

I want to thank Hassan Hossein Nia Kani and Jo Spronck for their guidance and for having deep discussions. I always had new ideas on how to continue and what to explore next after our meetings. In addition, I want to thank my fellow students I met during my whole study. They made my experience with Delft University enjoyable and fruitful.

Summary

The high-precision industry demands the next generation of contactless actuators. These actuators must be able to generate high forces, while having a high bandwidth and being energy efficient. The state-of-the-art contactless actuators, such as Lorentz and hybrid reluctance actuators, use current-driven coils for generating the magnetic force. The usage of coils leads to significant heating, which is a limitation in reaching higher precision at this moment. As a result, these actuators fall short of meeting the criteria of the next generation of actuators.

This thesis introduces a novel alternative to replace the coils of a hybrid reluctance actuator. The alternative, referred to as reluctance tuning, is based on the control of tunable air gaps within the stator of a hybrid reluctance actuator. Adjusting the length of these air gaps alters the reluctance, causing an unbalance in the magnetic flux and inducing a magnetic force on the central mover of the actuator. Piezoelectric actuators are utilized to control the lengths of the air gaps. Figure 1 shows an overview of the complete design. The result of this new design is an actuator with the best of both worlds of reluctance actuators and piezoelectric actuators. Reluctance actuators offer the advantage of contactless high magnetic forces but come with high heat dissipation due to the driven coils. On the other hand, piezoelectric actuators have relatively low heat dissipation but suffer from their very stiff mechanical connection with the object that needs to be displaced, resulting in poor disturbance rejection of vibrations. By integrating both types of actuators into a unified design, it becomes possible to create an actuator that by the motion of a piezoelectric actuator can apply a contactless magnetic force on a mover with minimal heat dissipation, thereby earning it the title of the contactless piezo-magnetic actuator. Furthermore, piezoelectric actuators exhibit a high bandwidth, enabling the piezo-magnetic actuator to be employed at very high frequencies.

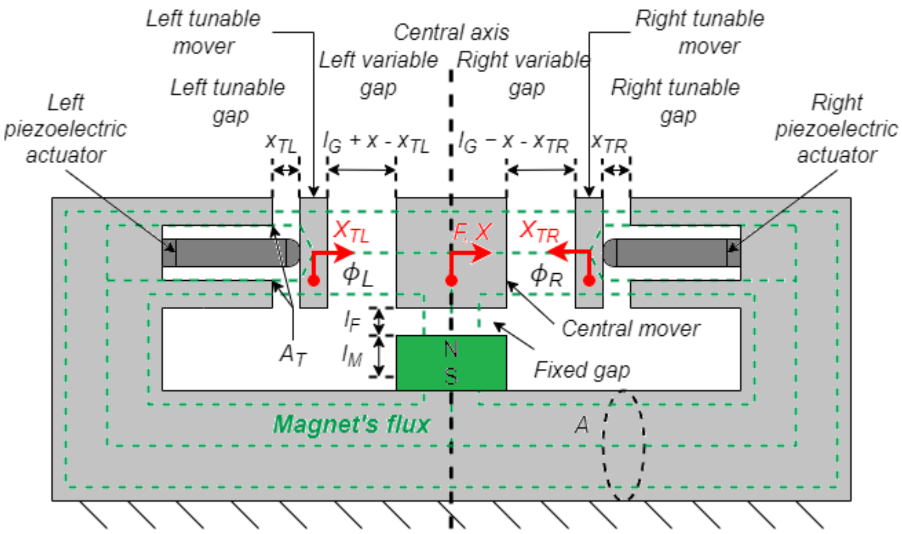

Figure 1: The developed Piezo-Magnetic Actuator

The magnetic force output of the designed piezo-magnetic actuator is evaluated by an analytical model and validated by a 3D finite element analysis model. The analytical model shows that the non-linear magnetic force exhibits highly linear behavior in case the displacement of the piezoelectric actuators is below $100\,\mu\mathrm{m}$. The experimental demonstrator verified the ability of the actuator to magnetically displace the central mover through the displacement of piezoelectric actuators, and not by using coils.

Moreover, it establishes the existence of a ratio between these displacements, termed as magnetic displacement amplification. The currently built piezo-magnetic actuator is capable of displacing the central mover magnetically by $54.61\,\mu\mathrm{m}$, utilizing a single piezoelectric actuator with a displacement of $18.2\,\mu\mathrm{m}$. The open-loop frequency response of the experimental demonstrator shows similarities for various voltage amplitudes applied to the piezoelectric actuators below $100\,\mathrm{Hz}$, enabling an approximation by a single mass-spring-damper system. The first resonance peak of the experimental demonstrator is at $23\,\mathrm{Hz}$. This is attributed to the low stiffness of utilized flexures, which were essential for the open-loop stability of the experimental demonstrator. However, in practice, by using control the flexures are not required anymore and therefore improved dynamics can be achieved. The open-loop time response reveals that, at lower frequencies, the displacement of the mover can accurately follow a voltage signal. However, due to the low first resonance peak at $23\,\mathrm{Hz}$, a significant phase lag arises between the two signals, even at low frequencies.

The maximum force output of the currently designed piezo-magnetic actuator is rather low compared to an equivalent hybrid reluctance actuator. However, in terms of energy efficiency, the piezo-magnetic actuator dissipates no energy in steady state to maintain the magnetic force, while the hybrid reluctance actuator does. An energy-efficiency bandwidth metric is used to compare the heat dissipation of both actuators during dynamic operations aimed at generating the same magnetic force. It shows that for relatively low peak-to-peak voltage applied to the piezoelectric actuators, the piezo-magnetic actuator is more energy efficient, even at high frequencies.

The developed piezo-magnetic actuator can be characterized as an energy-efficient short-stroke reluctance actuator. Its minimal heat dissipation makes it particularly suitable for applications in vacuum, space, and cryogenic environments, where high-precision stage positioning or vibration isolation with low heat dissipation is essential. Additionally, there is potential for its utilization as a replacement for piezoelectric actuators in systems that necessitate contactless actuation or a larger displacement range.

Contents

1 Introduction 1
1.1 Background . . . 1
1.2 Problem definition . . . 1
1.3 Prior art: energy-efficient reluctance actuators . . . 2
1.3.1 Magnet tuning . . . 2
1.3.2 Smart material implementation . . . 3
1.4 Problems of prior art . . . 3
1.5 Research goal and objectives . . . 4
1.6 Outline . . . 4

2 Preliminary knowledge: basics of magnetics 6
2.1 Magnetization . . . 6
2.2 BH-curve . . . 7
2.3 Magnetic circuit method . . . 8
2.3.1 Current source . . . 8
2.3.2 Magnet source . . . 9
2.3.3 Equivalent magnet source . . . 10
2.3.4 Kirchhoff's circuit laws for magnetic circuits . . . 11
2.3.5 Flux factors . . . 11
2.3.6 Maxwell stress tensor . . . 12
2.4 Energy losses in electromagnetic actuators . . . 12
2.4.1 Joule heating . . . 12
2.4.2 Eddy currents . . . 12
2.4.3 Magnetic hysteresis losses . . . 13

3 Reluctance tuning 14
3.1 Hybrid Reluctance Actuator analysis . . . 14
3.2 Unbalancing magnetic flux without coils . . . 15
3.3 Reluctance of air gaps . . . 16
3.4 Reluctance tuning principles . . . 16
3.4.1 Principle A: exchange of reluctance . . . 17
3.4.2 Principle B: expansion of gap length . . . 17
3.4.3 Principle C: reduction of gap cross-section . . . 18
3.4.4 Comparison of principles . . . 19
3.5 Conclusion chapter 3 . . . 19

4 Actuator design and modeling 20
4.1 Design and working principle . . . 20
4.1.1 Piezoelectric actuator implementation . . . 21
4.2 Analytical model . . . 21
4.2.1 Magnetic force analysis . . . 23
4.2.2 Maximum magnetic force potential . . . 24
4.2.3 Linearity analysis analytical model. . . . 25
4.3 Hybrid Reluctance Actuator and Piezo-Magnetic Actuator comparison . . . 26
4.3.1 Force comparison . . . 26
4.3.2 Heat dissipation comparison . . . 27
4.4 Finite Element Analysis model . . . 28
4.4.1 Comparison analytical model and Finite Element Analysis model . . . 29
4.4.2 Magnetic force on tunable movers. . . . 30
4.5 Conclusion Chapter 4 . . . 30

5 **Experimental Demonstrator and Tests** **32**
5.1 Piezo-Magnetic Actuator setup . . . 32
5.1.1 Actuator . . . 33
5.1.2 Central mover. . . . 33
5.1.3 Tunable movers . . . 34
5.2 Method . . . 34
5.2.1 Pre-loading the piezoelectric actuators . . . 34
5.2.2 Displacement behavior . . . 34
5.2.3 Open-loop frequency response . . . 35
5.2.4 Open-loop time response . . . 35
5.3 Experimental results and discussion . . . 35
5.3.1 Displacement behavior: magnetic displacement amplification . . . 35
5.3.2 Comparison analytical model and experimental results . . . 36
5.3.3 Open-loop frequency response . . . 36
5.3.4 Open-loop time response . . . 37
5.4 Conclusion chapter 5 . . . 39

6 **Conclusion, recommendations, future research, potential, and applications** **40**
6.1 Conclusion . . . 40
6.2 Recommendations and further research . . . 41
6.2.1 Recommendations . . . 41
6.2.2 Future research. . . . 43
6.3 Actuator potential and applications . . . 44

A **Actuators using magnetostrictive and piezoelectric material** **45**
A.1 Coilless rotating actuator. . . . 45
A.2 Coilless actuator using a composite core . . . 46
A.3 Multilayer composite core . . . 47
A.4 Analytical model HRA with magnetrostrictive cores . . . 48
A.4.1 Magnetic force analysis . . . 50

B **Analytical model Hybrid Reluctance Actuator** **51**

C **Reluctance tuning parameters** **53**

D **Analytical model Piezo-Magnetic Actuator** **54**
D.1 Network equations . . . 54
D.2 Magnetic flux in variable right air gap . . . 55
D.3 Magnetic flux in variable left air gap . . . 56
D.4 Total reluctance of all gaps. . . . 56
D.5 Simplified magnetic flux equation . . . 57
D.6 The magnetic force . . . 57
D.7 Magnetic force terms . . . 57

E **Actuator design parameters** **59**

F **Settings FEA model** **60**

G **Finite Element Analysis model convergence results** **62**

H **Magnetic saturation, flux leakage, and fringing flux** **63**
H.1 Magnetic saturation . . . 63
H.2 Flux leakage . . . 64
H.3 Fringing flux. . . . 65

I **LabVIEW model** **66**

J **Stiffness measurement** **68**

K **MATLAB settings and validation** **69**
K.1 MATLAB settings . . . 69
K.2 Complete frequency reponse . . . 69

K.3 MATLAB validation 70

L PiezoDrive 150V stacked piezoelectric actuator 72

List of Figures

1 The developed Piezo-Magnetic Actuator ii

1.1 Energy efficient reluctance actuators based on magnet tuning 2
1.2 Energy efficient reluctance actuators based on smart material implementation 3

2.1 Magnetization [9] 6
2.2 BH-curve [6] 7
2.3 C-shape actuator with a magnet as MMF source [8] 9
2.4 The operation point of a magnet visualized in the BH-curve [6] 10
2.5 Fringing flux and flux leakage [22] 11

3.1 Schematic overview of a Hybrid Reluctance Actuator [3] 14
3.2 The effect of the reduction of the length and cross-section of an air gap on the magnetic field 16
3.3 Reluctance tuning principle A 17
3.4 Reluctance tuning principle B 18
3.5 Reluctance tuning principle C 18
3.6 Analytical comparison of the reluctance tuning principles 19

4.1 The Piezo-Magnetic Actuator 20
4.2 Pre-loading technique piezoelectric actuator [27] 21
4.3 Analytical model of the magnetic circuit of the PMA 22
4.4 Evaluation of the analytical model for increasing position of the left tunable mover x_{TL}, while varying the position of the central mover x. 24
4.5 Maximum magnetic force potential of the PMA incorporating smart material that can displace $800\,\mu\mathrm{m}$ 25
4.6 Linearity analysis of the magnetic force of the PMA 26
4.7 Magnetic force comparison PMA and HRA 26
4.8 Heat dissipation comparison of a HRA and PMA 28
4.9 3D model of the actuator in COMSOL Multiphysics® 29
4.10 Comparison analytical model and FEA model 29
4.11 Magnetic force investigation on the tunable movers by using the 3D FEA model 30

5.1 Overview of the built PMA demonstrator 32
5.2 Overview of the built actuator 33
5.3 Overview of the built central mover 33
5.4 Overview of the built tunable movers 34
5.5 Open-loop diagram of the experimental setup 34
5.6 Displacement behavior of the system for increasing voltage 35
5.7 Measured displacement of the central mover compared to the analytical model 36
5.8 Open-loop Frequency response of the built demonstrator for different voltage amplitudes including an equivalent mass-spring-damper system 37
5.9 Open-loop time response of the built demonstrator for sinusoidal voltage signals with different frequencies 38
5.10 Open-loop time response of the built demonstrator for triangular voltage signals with different frequencies 38
5.11 Open-loop time response of the built demonstrator for step input voltage signals with different frequencies 39

6.1 The developed PMA 40

A.1 Overview of the coilless rotating actuator 45
A.2 Experimental results based on the coilless rotating actuator 46
A.3 The magnetic force control device 46
A.4 Experimental results based on the magnetic force control device 47
A.5 Overview of a core made of multiple layers of PZT/Metglas units [46] 47
A.6 Devices based on PZT/Metglas composite core 48
A.7 Measured relative permeability by varying the applied voltage on the PZT sheets [45] . 48
A.8 Overview and analytical model of an Hybrid Reluctance Actuator and two integrated composite cores 49
A.9 Evaluation of the analytical model for increasing relative permeability of the left composite core, while keeping the position of the mover at $x = 0$ 50

B.1 Analytical model of the magnetic circuit of an HRA 51

D.1 Analytical model of the magnetic circuit of PMA 54

F.1 3D model with dimensions 60
F.2 Selected components in blue for the local adaptive mesh refinements 61

G.1 Percentage error between the mesh refinements for increasing position of the left tunable mover while varying the position of the central mover 62

H.1 The magnetic flux density in the 3D FEA model, with the left tunable mover positioned at T_{TL} = $240\,\mu\text{m}$ and the central mover is in its center position 63
H.2 The magnetic flux density in the 3D FEA model with the left tunable mover positioned at T_{TL} = $240\,\mu\text{m}$ and the central mover at x = $600\,\mu\text{m}$ 64
H.3 Fringin flux in the 3D FEA model 65

I.1 The LabVIEW block diagram used for performing the experiments - part A 66
I.2 The LabVIEW block diagram used for performing the experiments - part B 66
I.3 The LabVIEW front panel used for performing the experiments 67

J.1 Experimental setup for measuring the stiffness of central mover 68
J.2 Experimental setup for measuring the stiffness of tunable movers 68

K.1 The complete frequency responses of the system estimated by MATLAB for different voltage amplitudes 70
K.2 Comparison of the estimated transfer function by MATLAB representing the $15\,\text{V}$ to $150\,\text{V}$ voltage signal to a calculated gain based on a frequency response measurement 71

List of Tables

3.1 Advantages and disadvantages of the reluctance tuning principles 19

4.1 Parametric analysis of magnetic force 24
4.2 BTI and energy-efficiency bandwidth 28

C.1 Parameter values for comparison reluctance principles 53

E.1 PMA design parameters 59

F.1 Material Properties 61

K.1 MATLAB settings 69

L.1 Specifications of the PiezoDrive SA050520 $150\,\mathrm{V}$ piezoelectric actuator [36] 72

Glossary

BTI Break-even Tuning Interval.

DF Dissipation Factor.

EMF Electro Motive Force.

FEA Finite Element Analysis.

HRA Hybrid Reluctance Actuator.
HTMA Hybrid Tunable Magnet Actuator.

MCM Magnetic Circuit Method.
MMF Magneto Motive Force.
MSM Magnetic Shape Memory.

NdFeB Neodymium-Ferite-Boron.

PLA PolyLactic Acid.
PMA Piezo-Magnetic Actuator.
PZT Lead Zirconium Titanate.

TMA Tunable Magnet Actuator.

1

Introduction

1.1. Background

In order for the high-precision industry to enhance throughput and manufacture smaller features on products, the next generation of contactless actuators is needed. These actuators must be able to generate high forces while having a high bandwidth and being energy efficient [1]. Contactless actuators refer to actuators where the stiffness between the stator and mover is low or even zero. This offers the capability to effectively reject vibrations transmitted from the stator to the mover, thereby enhancing precision.

The widely implemented Lorentz actuator falls short of meeting the criteria of the next generation of actuators [1]. This actuator is based on the Lorentz force exerted on a current-driven coil within a magnetic field [2]. Typically, the coil is mechanically decoupled from the stator or suspended by low-stiffness wires. Lorentz actuators are favored for their linear relation between force and current, irrespective of the position of the mover within a uniform flux density. Moreover, they provide a large displacement range and offer high disturbance rejection. Nevertheless, a drawback lies in their low motor constant, the force-to-current ratio, resulting in significant heating of the coil when large forces are needed [2][3][4].

A promising candidate for satisfying the needs of the high-precision industry is the Hybrid Reluctance Actuator (HRA). This actuator is based on the attraction force between a soft ferromagnetic mover and stator magnetized by coils and a permanent magnet [2]. It is characterized as a short-stroke contactless actuator. HRAs offer a higher motor constant compared to Lorentz actuators, and this constant is relatively proportional to the coil current [4]. As a result, generating the same magnetic force as Lorentz actuators demands less current, making HRAs more energy-efficient [1]. However, HRAs have not been implemented extensively in the past, because they suffer from large parasitic effects including magnetic hysteresis and eddy currents, impacting their predictability and controllability [1][2][5]. In addition, their force output depends on the position of the mover and exhibits negative stiffness behavior. This requires the implementation of stiff flexures to ensure open-loop stability [4]. Most recently, however, researchers have investigated and tackled most of these challenges with advanced control strategies [2][4]. HRAs are therefore a compelling choice for meeting the evolving standards of the high-precision industry.

1.2. Problem definition

Despite the advantages of HRAs over Lorentz actuators, they still have the drawback of heat dissipation leading to an increase in temperature. The heat dissipation mainly arises from the current that flows through the coils of an HRA, referred to as Joule heating. Other sources of heat dissipation are eddy currents and magnetic hysteresis [6][7]. The heat dissipation fluctuates in dynamic operations, which adds complexity to prediction and compensation efforts. Increasing temperatures negatively impact the performance of HRAs for several reasons:

- Thermal expansion of components, resulting in deformations and unmeasured changes of air gaps [1][6][7].
- Changes in ferromagnetic properties, which are temperature dependent [7].
- Temperature dependency of Hall sensors, this will affect the magnetic flux measurements [7].
- Demagnetization of permanent magnets. At temperatures above a critical temperature, the Curie temperature, the remanent flux density reduces permanently [8].

The heat dissipation of HRAs is a significant problem in high-precision systems operating in vacuum, space, and cryogenic environments. Under these conditions it is challenging to cool the actuators, allowing the heat to disperse throughout the entire system. This not only reduces the performance of the HRAs but also adversely affects the overall system performance [9]. All the mentioned problems underscore the importance of minimizing heat dissipation in HRAs to enhance their performance and attain greater precision for applications in high-precision industries.

1.3. Prior art: energy-efficient reluctance actuators

In recent studies, researchers have proposed new designs of energy-efficiency reluctance actuators. These actuators use alternatives to the coils, which can be categorized in magnet tuning and smart material implementation.

1.3.1. Magnet tuning

Knaian introduced the electropermanent magnet device depicted in Figure 1.1a [10]. This device applies an electrical pulse with a fixed amount of energy to the coil wrapped around the semi-hard and hard magnet. This pulse only magnetizes or demagnetizes the semi-hard magnet. Depending on the polarity of the electrical pulse, the generated magnetic field either cancels or amplifies the field of the hard magnet. When amplified, a static magnetic force is generated on the soft ferromagnetic target.

At University of Technology, recent studies have led to the development of the Tunable Magnet Actuator (TMA) [6][9][11] [12][13]. Functioning similarly to the electropermanent magnet device, this actuator consists only of a semi-hard magnet as illustrated in Figure 1.1b. It uses a variable current, determined by a tuning algorithm, to magnetize or demagnetize the magnet. As such, different magnetization states can be achieved resulting in a variable magnetic force on the soft ferromagnetic mover.

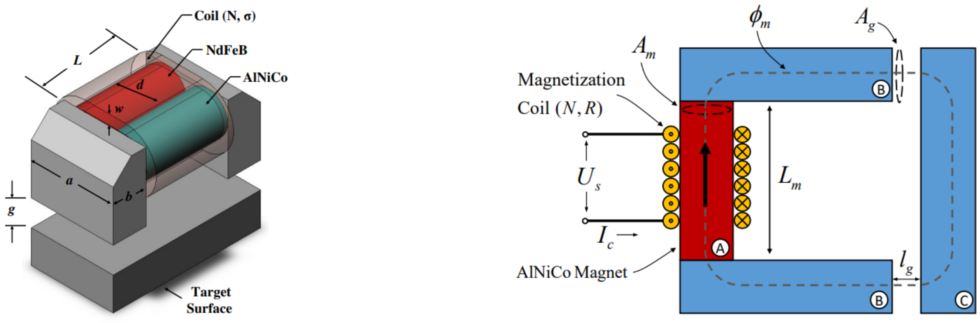

(a) The electropermanent magnet device [10]

(b) The Tunable Magnet Actuator [11]

Figure 1.1: Energy efficient reluctance actuators based on magnet tuning

1.3.2. Smart material implementation

Hutter et al. introduced a reluctance actuator that incorporates Magnetic Shape Memory (MSM) sticks. This design utilizes a permanent magnet with a magnetic field distributed in two parallel paths, as illustrated in Figure 1.2a [14]. By compressing the MSM sticks the magnetic resistance, also referred to as reluctance, increases in one of the paths. For this reason, the magnetic field distribution changes, resulting in a variable magnetic force on the soft ferromagnetic armature. The compression force on the MSM sticks is performed by a thermal shape memory alloy mechanism.

Ueno et al. developed a magnetic device featuring a composite core made of magnetostrictive material, Terfenol-D, and two stacked piezoelectric actuators as depicted in Figure 1.2b [15]. Similar to the previously introduced design, the magnetic field of the permanent magnet is distributed in two parallel paths. The composite core is initially compressed by two bolts. Pre-stressing increases the reluctance of the magnetostrictive material. Applying voltage to the stacked piezoelectric actuators causes the material to deform, reducing the compressive stress on the magnetostrictive material. This effect reduces the reluctance of the magnetostrictive material, altering the magnetic field distribution and resulting in a variable magnetic force on the soft ferromagnetic moveable yoke. An in-depth evaluation of actuators combining magnetostrictive and piezoelectric materials into the design is presented in Appendix A.

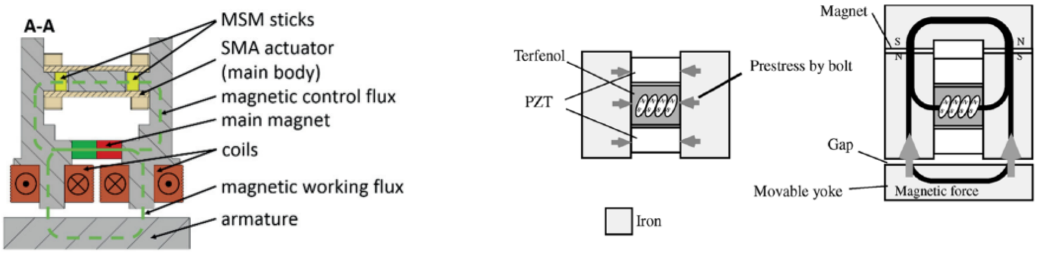

(a) Reluctance actuator based on MSM sticks [14]

(b) Relutance actuator based on magnetostrictive Terfenol-D and two stacked piezoelectric actuators [15]

Figure 1.2: Energy efficient reluctance actuators based on smart material implementation

1.4. Problems of prior art

The electropermanent magnet device and the TMA do not require energy to maintain the magnetic force. Nonetheless, both systems experience significant energy losses while tuning the magnet state, resulting in heat dissipation. While improvements in the tuning approach can mitigate these losses to some extent, they are inevitable. For this reason, these actuators are only interesting to use at low-tuning frequencies or in parallel combination with an electromagnetic actuator.

An issue of the actuator based on the MSM sticks is the thermal shape memory alloy mechanism needed for the compression force. This mechanism is a significant heat source during actuation, limiting the overall performance of the actuator. The choice of a direct heat source in an actuator designed for zero heat dissipation raises questions, necessitating a reconsideration of the working principle for this actuator.

The magnetic device that uses the composite core made of magnetostrictive and piezoelectric material does not dissipate energy in static operation, excluding current leakage. During the actuation of the piezoelectric actuators, there is a transfer of charge leading to Joule heating. Additionally, the actuation of the piezoelectric material generates mechanical, dielectric, and piezoelectric losses [16][17][18]. Nevertheless, the heat dissipation of piezoelectric material, when actuated below its resonance frequency, is significantly lower compared to a coil driven with a high current. A drawback of the composite core is its placement inside the stator of the actuator, contributing higher reluctance than common soft ferromagnetic materials like iron. This increased reluctance lowers the maximum magnetic force output of the actuator.

1.5. Research goal and objectives

Based on the problem definition and the identified issues in prior art, the research goal is formulated as follows:

”To design, validate, and build a Hybrid Reluctance Actuator with a new alternative to the coils, that is energy-efficient in both static and dynamic operations and does not contribute to the total reluctance of the actuator when uncontrolled.”

The developed actuator, if successful, holds the potential to represent the next generation of actuators in the high-precision industry. Besides reducing heat dissipation and thus having better performance, it opens up the possibility of controlling a magnetic force in a new way. From here, new research opportunities can come forth.

To achieve the research goal, the following objectives are outlined:

1. **Analyze the design of a Hybrid Reluctance Actuator** . Gain insight into the parameters influencing the magnetic force of a Hybrid Reluctance Actuator before delving into the development of a new energy-efficient actuator.
2. **Develop alternative concepts to replace the coils.** The initiation of the design phase involves a Hybrid Reluctance Actuator without the coils, yet capable of exerting a magnetic force on the mover. This necessitates the exploration of novel methods for generating the magnetic force. Once developed, the concepts will be compared to identify the most promising concept.
3. **Design an actuator with implementation of the most promising concept**. The best concept will be integrated into the design of an HRA. This could require creative and unconventional approaches.
4. **Derive an analytical model to evaluate the designed actuator**. Once a final design is determined, the actuator will be analyzed by using a lumped parameter model of the magnetic circuit. The model will be used to get insight into the relationship between the design parameters and the magnetic force of the developed actuator.
5. **Compute a Finite Element Analysis (FEA) model of the designed actuator**. Use FEA software to validate the analytical model, accounting for factors such as fringing flux, flux leakage, and magnetic saturation that are often simplified in lumped parameter models.
6. **Build an experimental demonstrator of the designed actuator.** Recognizing that models are approximations, an experimental demonstrator will serve as a proof of concept. In this setup, the behavior of the actuator will be evaluated. Moreover, the open-loop frequency and time response of the actuator will be measured.
7. **Compare the designed actuator to an equivalent Hybrid Reluctance Actuator**. The developed actuator will be compared to an equivalent HRA. The magnetic force and the difference in heat dissipation during static and dynamic operations will be investigated.

1.6. Outline

This thesis is structured into the following sections. Chapter 2 delves into the fundamentals of magnetics and explores energy losses in electromagnetic actuators. In Chapter 3, the novel alternative to the coils in an HRA is introduced. Chapter 4 offers a comprehensive overview of the designed actuator, providing detailed analyses through an analytical model and FEA model. Additionally, it compares the designed actuator with an equivalent HRA. Chapter 5 details the construction of the experimental demonstrator and presents the conducted measurements. Chapter 6 serves as the conclusion, offering recommendations and suggesting future research topics. It emphasizes the potential applications in which the developed actuator could excel.

An in-depth evaluation of actuators combining magnetostrictive and piezoelectric materials into the design is presented in Appendix A. Appendix B contains the complete derivation of the magnetic force of an HRA. Appendix C presents a table of parameter values used for evaluating the developed alternatives to the coils. Appendix D provides the complete derivation of the magnetic force of the developed actuator. Design parameter values used in the analytical model, FEA model, and experimental demonstrator are outlined in Appendix E. Appendix F summarizes the settings used in the FEA model, and the validation of the FEA model is discussed in Appendix G. Appendix H provides insights into the magnetic saturation, flux leakage, and fringing flux of the FEA model. The LabVIEW model utilized for experimental measurements is outlined in Appendix I. Appendix J summarizes the stiffness measurements of certain sub-assemblies of the experimental demonstator. MATLAB settings for estimating transfer functions are detailed in Appendix K. Finally, Appendix L presents specifications for the stacked piezoelectric actuator used in the experimental demonstrator.

2

Preliminary knowledge: basics of magnetics

This chapter provides a foundational understanding of magnetics, laying the groundwork necessary for understanding the reasoning presented in the subsequent chapters.

2.1. Magnetization

Ferromagnetic materials are characterized by their strong interaction with external magnetic fields. Within ferromagnetic materials are magnetic domains, referred to as Weiss domains. These domains are areas where the magnetic dipole moments are all aligned in a consistent direction, even in the absence of an external magnetic field. When a ferromagnetic material has not been magnetized before, the resultant magnetic flux density B_m inside the material is usually zero. This is because the alignment of the Weiss domains varies inside the material, leading to a cancellation of the magnetic fields. B_m is proportional to the number of magnetic field lines per unit area [19].

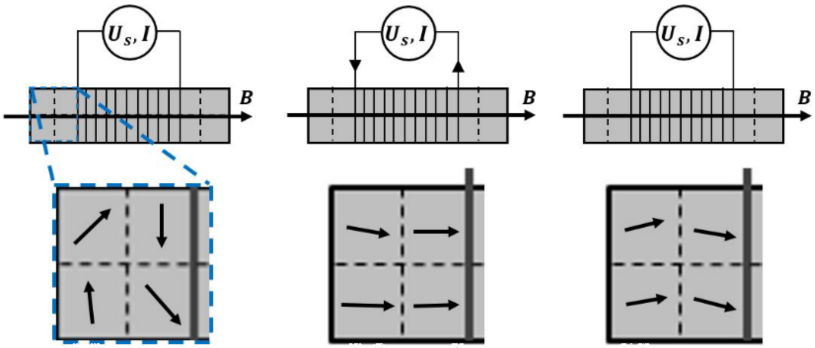

1. Zero-state $B \approx 0$

2. Saturated $B = \mu_0(H_{sat} + M)$

3. Rest state $B = B_r$

Figure 2.1: Magnetization [9]

However, when a ferromagnetic material is placed in an external magnetic field B_{app}, such as that of a coil depicted in Figure 2.1, the domain boundaries of Weiss domains can shift or the direction of alignment can change. This leads to a resultant magnetic flux density in the direction of B_{app} and the material is then said to be magnetized [19]. The external field of the coil magnetizes the material such that it has a magnetization M. The overall magnetic flux density at a point located within the coil and distant from its ends is [6]:

$$B_m = B_{app} + \mu_0 M \tag{2.1}$$

where μ_0 is the magnetic permeability of air or vacuum ($4\pi \times 10^{-7}$ H/m). It is a reference for the magnetic permeability of other materials and mediums, and its value is constant. When all Weiss domains are aligned in the direction of B_{app}, the material is saturated by H_{sat} and the magnetic flux density is equal to B_{sat}. When the external magnetic field is removed, many Weiss domains will remain in their new alignment. This results in a residual magnetization of the material. The magnetic flux density that remains is equal to the remanent flux density B_r, which is lower than B_{sat} [6].

2.2. BH-curve

The explained magnetization process of a ferromagnetic material can be visualized in a BH-curve as shown in Figure 2.2. In case an increasing DC current is applied to a coil, the magnetic field strength H_m of the material increases and therefore the magnetic flux density B_m increases. When a material has not been magnetized before it follows the virgin curve, represented by the blue line shown in Figure 2.2. It can be noticed that B_m does not vary linearly with H_m, which indicates that the relative magnetic permeability μ_r of the material is not constant [19]. As the curve levels off, it indicates that the magnetization M is reaching its saturation value B_{sat}, here all Weiss domains are aligned in the direction of B_{app}. Beyond saturation, the magnetic flux density inside the material increases only due to the increase of the external magnetic flux density of the coil. This side of the BH-curve is called the magnetization curve. By reducing the DC current of the coil to zero, the magnetic field strength decreases to zero. However, the magnetic field density does not reduce to zero, because many Weiss domains remain in their new orientation. This is referred to as magnetic hysteresis as depicted in Figure 2.2. At this juncture, the magnetic flux density corresponds to the remanent flux density B_r, indicating that the material functions now as a magnet [20][19].

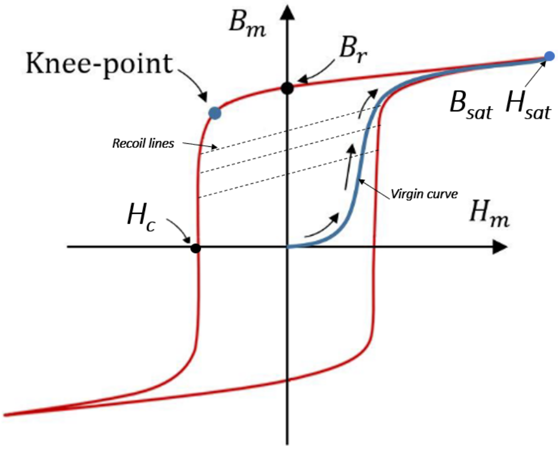

Figure 2.2: BH-curve [6]

By changing the polarity of the DC current of the coil, the magnetic flux density decreases. This side of the BH-curve is called the demagnetization curve and it depends on the history of the magnetization curve. The point at which the magnetic flux density intersects with the axis of H_m is called the coercive field intensity H_c. It is a measure of a magnetic material to resist demagnetization [6]. Material is referred to as soft ferromagnetic when the BH-curve is narrow, while those with a wide curve are considered hard ferromagnetic. The lines inside the BH-curve are called recoil lines, which are linearized in Figure 2.2. When a magnet gets demagnetized from saturation to a point beyond the knee-point, it will follow a recoil line once the DC current of the coil is reduced to zero [6]. The residual magnetization of the material is in this case lower than B_r.

2.3. Magnetic circuit method

To solve for magnetic fluxes and fields inside a magnetic circuit, Ampere's law can be used as a lumped parameter model for estimations, which from now on is called the Magnetic Circuit Method (MCM). In a magnetic circuit, the main components typically include soft ferromagnetic materials, air gaps, coils, and magnets. These elements can be connected in series and parallel. The MCM assumes that the direction of the magnetic fluxes and fields is known. Furthermore, it assumes that the magnetic field lines prefer to follow a path with high permeability. When a section with low permeability needs to be traversed, the magnetic field lines will follow the most direct route. By taking into account magnetic hysteresis, magnetic saturation, eddy currents, flux leakage, and fringing flux the estimations of the MCM become more accurate.

2.3.1. Current source

The method starts with Ampere's law, which relates the magnetic field strength H summed around a closed loop C of a magnetic circuit to the total current I_c that passes through any surface bounded by loop C [19]:

$$\oint_C \boldsymbol{H} d\boldsymbol{l} = I_c \tag{2.2}$$

In Equation 2.2, the closed loop C is made up of line segments dl, which represent the individual components of the magnetic circuit. The length of a line segment is approximated by the average path length of the magnetic field lines passing through the component. The direction of the line segment is the same as the magnetic field lines. The source of I_c can be a coil with N turns and I current. The magnetic field strength H of a component is equal to the magnetic field density B in the component divided by its magnetic permeability μ $(= \mu_0 \mu_r)$. With this in mind, the closed loop integral of Equation 2.2 can be rewritten to the sum of i individual components of a magnetic circuit [20]:

$$\sum_{n=1}^{i} \frac{B_i l_i}{\mu_i} = NI \tag{2.3}$$

In this equation NI is also known as the Magneto Motive Force (MMF), it is the source of magnetic fluxes and fields inside a magnetic circuit. Equation 2.3 can be compared to an electric circuit in which the MMF is related to the Electro Motive Force (EMF). The summation can be interpreted as the MMF drop due to each component along the path of the magnetic field lines [20]. Each component of a magnetic circuit carries a magnetic flux ϕ_i, where the surface area A_i of that component is normal to its magnetic flux density B_i [19]:

$$\phi_i = B_i A_i \tag{2.4}$$

Magnetic flux is analogous to electrical current. The way current flows through a series of connections, having the same value throughout, is similar to how magnetic flux behaves as it passes through a series of magnetic circuit elements, if flux leakage is neglected. Substituting Equation 2.4 into Equation 2.3 gives [20]:

$$\sum_{n=1}^{i} \phi_i \Re_i = NI \tag{2.5}$$

$$\Re_i = \frac{l_i}{A_i \mu_i} \tag{2.6}$$

The term $\Re_i$ is called reluctance and it represents the resistance of a material to magnetic flux. It can be compared to the resistance of an electric circuit. Just as resistance, reluctance can be added in series. When multiple components are connected in parallel, the total reluctance is the reciprocal of the sum of the reciprocals of the individual reluctances [20]. Equation 2.5 can be simplified when the MMF source is a coil, flux leakage is neglected, and all components of the circuit are in series:

$$\frac{NI}{\sum_{n=1}^{i} \Re_i} = \phi \tag{2.7}$$

This equation is referred to as Hopkinson's magnetic law. By using Equation 2.4 and Equation 2.7, the magnetic flux densities within each component along the magnetic flux path can be determined.

2.3.2. Magnet source

Instead of using current as the MMF source in a magnetic circuit, a magnet can be used. However, the magnetic field strength H_m of a magnet is not known beforehand and depends on the operation point of the magnet (B_0, H_0) [8]. Also, the magnet is part of the magnetic circuit and adds to the total reluctance of the circuit. Determining the operation point of a magnet starts with using Ampere's law. In this instance, the actuator illustrated in Figure 2.3 is employed consisting of a soft ferromagnetic stator and mover, two identical air gaps, and a magnet. The terms l_g, l_m, A, μ, and x are the lengths of the air gaps, the length of the magnet, the cross-section area of all components, the magnetic permeability of the components, and the position of the mover, respectively.

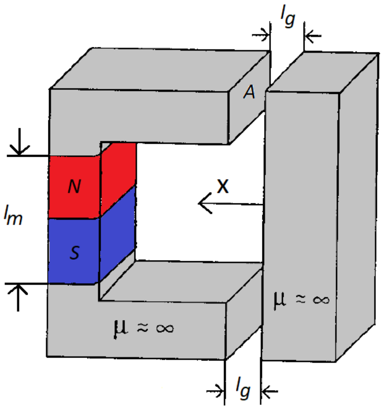

Figure 2.3: C-shape actuator with a magnet as MMF source [8]

Both the mover and stator are assumed to have a relative permeability that is sufficiently large, so the MMF drop of these components can be neglected. As a result, using Ampere's law gives the following:

$$2H_g l_g = -H_m l_m \tag{2.8}$$

where H_g and H_m are the magnetic field strength of an air gap and magnet, respectively. By considering that $B_g = H_g \mu_0$ holds for the air gaps, Equation 2.8 can be rewritten to:

$$B_g = \left(-\frac{\mu_0 l_m}{2 l_g}\right) H_m \tag{2.9}$$

If assumed that there is no flux leakage, in other words $B_m A_m = B_g A_g$, Equation 2.10 can be rewritten to:

$$B_m = \left(-\frac{\mu_0 l_m A_g}{2 l_g A_m}\right) H_m \tag{2.10}$$

The found equation is also known as the load line of a magnet, with a negative slope inside the brackets. The slope depends only on the geometric parameters of the magnetic circuit components. The operation point of the permanent magnet (B_0, H_0) is the point where the load line intersects with the BH-curve of the magnet as illustrated in Figure 2.4 [6].

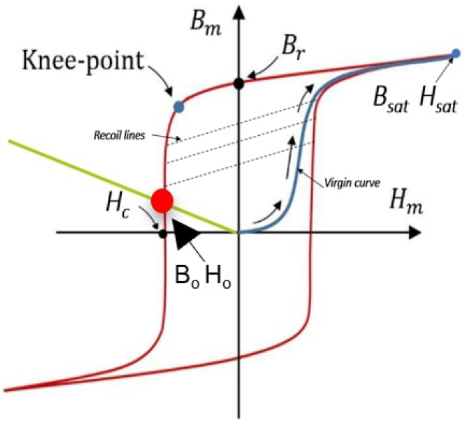

Figure 2.4: The operation point of a magnet visualized in the BH-curve [6]

The second quadrant demagnetization curve of the magnet, as depicted in Figure 2.4, can be estimated by the following linear expression [8]:

$$B_m = B_r + \mu_m H_m \tag{2.11}$$

where B_m, B_r, μ_m, and H_m are the magnetic flux density, the remanent flux density, the magnetic permeability of the magnet, and the magnetic field strength of the magnet, respectively. Note that μ_m is assumed to be linear and equal to B_r divided by H_c. Using Equation 2.10 and Equation 2.11 to find the point of intersection gives the following relation:

$$H_m = \frac{-B_r}{\left(\frac{\mu_0 l_m A_g}{2 l_g A_m}\right) + \mu_m} \tag{2.12}$$

Notice that when l_g goes to infinity, H_m tends to approach H_c. When l_g goes to zero, H_m tends to approach zero. This is also in agreement with the BH-curve shown in Figure 2.4. To find an expression for the magnetic flux through the magnetic circuit, Equation 2.8 can be rewritten to:

$$\frac{-H_m l_m}{2\Re_g} = \phi \tag{2.13}$$

where $\Re_g$ is the reluctance of an air gap. By multiplying Equation 2.12 by l_m and substituting into Equation 2.13, the magnetic flux can be calculated for the actuator employed in this case.

2.3.3. Equivalent magnet source

Assuming a magnet with a linear second quadrant demagnetization curve described by Equation 2.11, the magnetic flux can be determined through a simplified method. If flux leakage is disregarded, the MMF source is represented by a magnet, and all circuit elements are in series, the following expression can be directly applied to compute the magnetic flux in the magnetic circuit [8]:

$$\frac{H_c l_m}{\sum_{n=1}^{i} \Re_i} = \phi \tag{2.14}$$

where H_c, l_m, $\Re_i$ and ϕ are the coercive field intensity of the magnet, the length of the magnet, the reluctance of each component in the circuit, and the magnetic flux, respectively. It is important to highlight that the reluctance of the magnet must be added to the overall reluctance of the circuit and is equal to the length of the magnet l_m divided by its surface area A_m and magnetic permeability μ_m.

2.3.4. Kirchhoff's circuit laws for magnetic circuits

When dealing with more complex magnetic circuits, it is more common to apply Kirchhoff's laws for magnetic circuits, which are analogous to Kirchhoff's laws for electrical circuits, to solve for magnetic fluxes and fields in a magnetic circuit. These laws state that within a closed magnetic circuit loop, the total MMF equals the sum of the product of the magnetic flux and the reluctance for each element in the loop. Furthermore, these laws assert that at any node in a magnetic circuit, the sum of the magnetic flux entering the node equals the sum of the magnetic flux leaving the node [8]. These principles give rise to network equations governing the closed loops and nodes in a magnetic circuit.

2.3.5. Flux factors

Fringing flux is the phenomenon of a magnetic field in a soft ferromagnetic core to disperse as it enters an air gap as depicted in Figure 2.5. This causes an increase in the surface area A_{eff} observed by the magnetic field in the air gap and can lead to a decrease in reluctance. Fringing flux can be neglected when the air gap path length is small compared to the surface area observed by the magnetic field in the air gap. The fringing flux factor is defined as follows [7]:

$$k_{fringe} = \frac{A_{eff}}{A} \tag{2.15}$$

where A is the cross-section of the soft ferromagnetic core next to the air gap and A_{eff} is the surface area observed by the magnetic field in the air gap. This factor is in most cases greater than 1 [20].

Flux leakage is the phenomenon of magnetic field lines generated by an MMF source not reaching an intended air gap as depicted in Figure 2.5. The flux leakage factor can be defined as the ratio of the magnetic flux generated by an MMF source to the flux that passes through the intended air gap [21]:

$$k_{leakage} = \frac{\phi_{MMF}}{\phi_{gap}} \tag{2.16}$$

This factor is typically larger than 1. By considering both flux factors, the load line of a magnet in a magnetic circuit similar to Figure 2.3 will have the following expression:

$$B_m = \frac{k_{fringe}}{k_{leakage}} \left(-\frac{\mu_0 l_m A_g}{2 l_g A_m} \right) H_m \tag{2.17}$$

In the case of a change in the length of an air gap, the change in magnetic flux is non-linear, influenced by both flux factors [21]. Analytical determination of these loss factors is complex, leading to the widespread use of FEA software for precise modeling of magnetic fields in electromagnetic actuators.

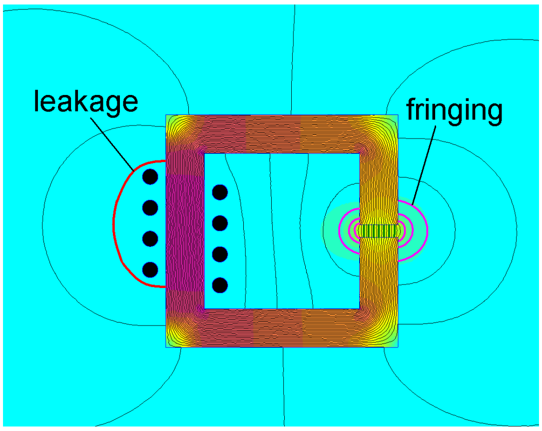

Figure 2.5: Fringing flux and flux leakage [22]

2.3.6. Maxwell stress tensor

An air gap is essential in an actuator to establish unobstructed space, allowing a soft ferromagnetic mover or coil to undergo displacement within this gap. The Maxwell stress tensor is used to compute the magnetic force exerted on soft ferromagnetic material within the gap in the presence of magnetic fields. The attractive force acting on the soft ferromagnetic material in the air gap region is determined as follows [8]:

$$\boldsymbol{F} = \frac{1}{2\mu_0} \oint_S {B_n}^2 \hat{\boldsymbol{n}} ds = \frac{1}{2\mu_0 A^2} \oint_S {\phi_n}^2 \hat{\boldsymbol{n}} ds \tag{2.18}$$

where $\hat{\boldsymbol{n}}$ is the outward unit normal to the bounding surface of the soft ferromagnetic material in the air gap, S is the surface area of the soft ferromagnetic material in the gap, and B_n is the magnetic field density within the air gap in the same direction as $\hat{\boldsymbol{n}}$.

2.4. Energy losses in electromagnetic actuators

The energy losses with electromagnetic actuators can be categorized into mechanical and electromagnetic losses. In this section, only the electromagnetic losses are considered.

2.4.1. Joule heating

When a current flows through a conductive wire, heat gets dissipated due to resistivity. This phenomenon is known as Joule heating:

$$E_{Joule} = \int_0^T I(t)^2 R dt \tag{2.19}$$

where the amount of energy loss is related to the applied current $I(t)^2$, time T, and resistance R of the wire.

2.4.2. Eddy currents

If the magnetic flux through a surface bounded by conductive material changes, an EMF ε, equal in magnitude to the rate of change of the magnetic flux with respect to time, is induced inside the material. This EMF induces a circulating current, also known as eddy current, which generates undesired Joule heating in the conductive material. The change in magnetic flux can be effected by moving a permanent magnet towards or away from the surface or by changing the MMF due to a current. Other ways of changing the flux are varying the surface area or by a change in orientation of the magnetic field or the surface. Faraday's law expresses the induced EMF as follows: [19]:

$$\varepsilon = IR = -\frac{d\phi_m}{dt} \tag{2.20}$$

where I is the eddy current, R is the resistance of the material, and $\frac{d\phi_m}{dt}$ is the rate of change of the magnetic flux with respect to time. An EMF caused by the motion of a conductive material in a region with a magnetic field or a permanent magnet moving towards or away from a conducting loop is called a motional EMF. A changing magnetic flux due to a current drop induces an EMF that tends to oppose the change in magnetic flux, this is called self-induced EMF. A method to reduce the effect of eddy current is to laminate the conductive material. The conductive material is made up of small slabs. The resistance of each slab is higher than the resistance of one solid piece, due to the smaller area per slab. This reduces the eddy current. In between the slabs can be air or a surface treatment like glue. Due to this the current cannot flow from one slab to another and is contained within each slab [20].

2.4.3. Magnetic hysteresis losses

Magnetic hysteresis losses are caused by the magnetization and demagnetization of ferromagnetic materials. If a coil is wrapped around a ferromagnetic material and the current increases, the magnetic flux density inside the material increases as well. The increase in current is in this case referred to as the magnetizing force. As soon as the magnetizing force reaches zero, the magnetic flux density inside the ferromagnetic material still has a positive value and is equal to the remanent flux density. In order for the remanent flux density to reduce to zero, the magnetizing force must be applied in the opposite direction. Thus, the magnetic flux density of a ferromagnetic material is related to its magnetic field strength and history. This phenomenon is known as magnetic hysteresis and it results in a loss of energy when ferromagnetic materials are subjected to alternating magnetic fields. The amount of energy loss in a uniformly ferromagnetic material with volume V is equal to the area of the trajectory along its BH-curve [10]:

$$E_{hyst} = V \oint \boldsymbol{H} d\boldsymbol{B} \tag{2.21}$$

3

Reluctance tuning

This chapter provides insight into the working principle of an HRA. Furthermore, it delves into new alternatives for controlling a magnetic force without using coils.

3.1. Hybrid Reluctance Actuator analysis

HRAs consist of a soft ferromagnetic stator and mover, two variable air gaps, a permanent magnet, and two serial-connected coils wrapped around the stator as seen in Figure 3.1. In addition, there is an air gap between the mover and magnet, assumed to be fixed. The configuration is symmetric with reference to the central axis of the actuator. The permanent magnet generates a magnetic flux distributed to the left and right air gap next to the mover. This is also called biasing flux and it is denoted by the green lines in Figure 3.1. Applying a current to the coils generates a magnetic flux, denoted by the orange lines in Figure 3.1. The direction of the flux of the coils is the opposite of the flux of the magnet in one of the variable gaps. These fluxes cancel each other. Consequently, the total flux in one of the variable gaps is weaker than that in the other variable gap on the opposite side of the mover. The unbalanced flux on opposite sides of the mover results in a magnetic force on the mover in the direction of the flux of the coils [3]. This force is referred to as the motor constant of the actuator.

The biasing flux of the magnet itself also exerts a magnetic force on the mover towards the stator, that varies with the position of the mover. This force remains at zero when the mover is at its central position (x = 0) but progressively strengthens as the displacement of the mover from the center position increases [23]. This results in the negative stiffness behavior of the actuator also referred to as the actuator stiffness.

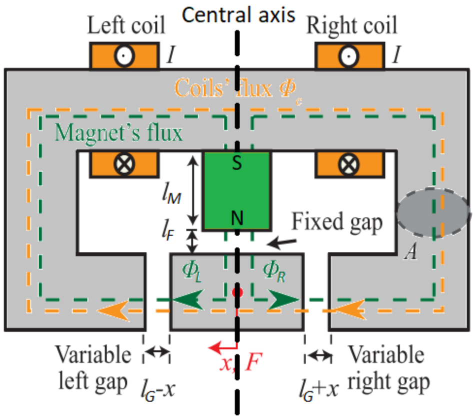

Figure 3.1: Schematic overview of a Hybrid Reluctance Actuator [3]

Utilizing the Maxwell stress tensor, an analytical expression is derived for the magnetic force acting on the mover for a single Degree of Freedom (DoF) in the direction of x. The complete derivation is presented in Appendix B. The magnetic force depends on the applied current I and the position x of the mover [3][4][24]:

$$F_{HRA} = K_M I + k_a x \tag{3.1}$$

where K_M is the motor constant and k_a is the actuator stiffness, given by [3]:

$$K_M = \frac{2H_c l_M \lambda A \mu_0 N}{2L_G l_M + 2L_G l_F + L_G^2 - x^2} \quad \text{and} \quad k_a = \frac{2H_c^2 l_M^2 \lambda^2 A \mu_0 L_G}{(2L_G l_M + 2L_G l_F + L_G^2 - x^2)^2} \tag{3.2}$$

where H_c is the coercivity field strength of the magnet, l_M is the length of the magnet, λ is the flux leakage of the magnet, A is the cross-section area of the materials, μ_0 is the permeability of air or vacuum, N is the number of windings of the coils, I is the current in the coils, x is the variable position of the mover relative to its center position, l_G is the size of the left and right air gap when the mover is in its center position, and l_F is the fixed air gap length.

3.2. Unbalancing magnetic flux without coils

If the coils of an HRA are taken out and the mover is in its center position ($x = 0$), Equation 3.1 becomes zero. In this configuration, no magnetic force can be exerted on the mover, because there is no variable input for unbalancing the magnetic flux.

This challenge has been addressed in research involving the Hybrid Tunable Magnet Actuator (HTMA) [6]. This actuator incorporates an additional magnet in the design and controls the remanent flux density of the magnet. As a result, a variable magnetic force can be produced on the mover without relying on the constant actuation of coils. Similarly, in the research focused on the reluctance actuators utilizing the MSM sticks and the composite core made of magnetostrictive and piezoelectric materials, control over the magnetic permeability of the magnetostrictive material is achieved. The magnetic permeability of a material denotes its capability to conduct magnetic flux. By regulating the magnetic permeability, it becomes possible to generate a variable magnetic force on a mover.

Currently, there is no HRA that incorporates an air gap within the stator, apart from the existing air gaps situated next to the mover. The control of the extra air gap in the stator changes the reluctance on one side of the actuator with respect to the central axis. As a result, the magnetic flux unbalances on opposite sides of the mover and a magnetic force is induced on the mover. As presented before, the reluctance of an element in a magnetic circuit is calculated as:

$$\Re = \frac{l}{\mu_0 \mu_r A} \tag{3.3}$$

where l is the length of the element, μ_0 is the permeability of air or vacuum, μ_r is the relative permeability of the element, and A is the cross-section of the element. This equation illustrates that as the relative permeability increases, the conductivity for magnetic flux also increases, and conversely decreases as relative permeability decreases. An air gap possesses a relative permeability of 1, while pure iron, in comparison, has a relative permeability of 200,000. This indicates that even a small air gap can significantly influence the reluctance of a magnetic circuit. Controlling the length or cross-sectional area of an air gap within a stator is presently referred to as reluctance tuning.

3.3. Reluctance of air gaps

The reluctance of an air gap within a stator can be changed by varying the air gap length or cross-section. Its magnetic permeability is fixed. The cross-section of an air gap depends on both surface areas of the stator next to the air gap. By reducing one or both surface areas of the stator, the air gap cross-section decreases, and therefore its reluctance increases. This effect is depicted in Figure 3.2. As one surface area of the stator decreases, there is a corresponding increase in magnetic flux density in that region. If the magnetic flux density surpasses a certain threshold, known as magnetic saturation, further reductions in the surface area of the stator cease to yield any additional benefits. The cross-section of an air gap is not equal to the surface area of the stator due to fringing flux and this effect is complex to derive analytically. For this reason, it is common in actuator designs to keep the length of an air gap small and the surface area of the stator on both sides of the air gap large. This significantly reduces the effect of fringing flux. In these conditions, it can be assumed that the cross-section of the air gap is equal to the surface area of the stator.

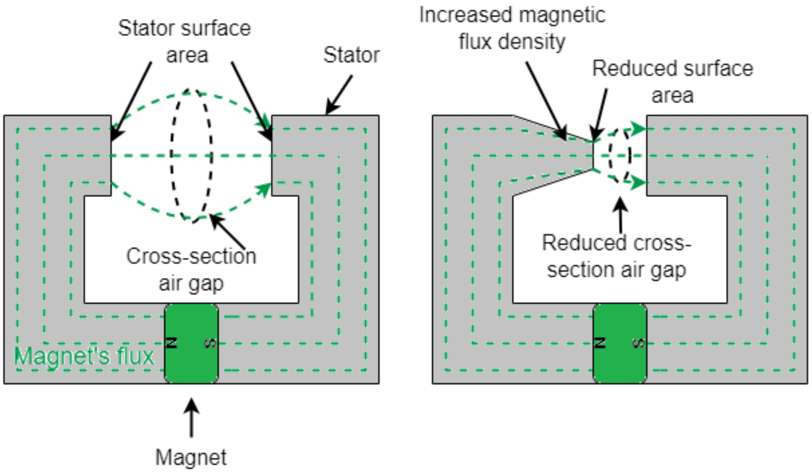

Figure 3.2: The effect of the reduction of the length and cross-section of an air gap on the magnetic field

3.4. Reluctance tuning principles

To develop reluctance tuning principles, two design guidelines are considered:

1. To keep the initial length of the controlled air gaps in the stator as small as possible. This reduces the total reluctance of the system, consequently enhancing the magnetic flux within the magnetic circuit, which is a favorable outcome.
2. To keep the expansion of the controlled air gaps in the stator to a relatively small extent. This minimizes the effect of fringing flux. An increase in surface area observed by the magnetic field in an air gap leads to a decrease in the change of reluctance by the expansion of the air gap, resulting in a drawback.

By respecting these guidelines, three reluctance tuning principles have been developed as seen in the sections below. Each principle consists of a soft ferromagnetic stator and mover, so as to provide variable air gaps between them. The stator is always connected to the world and a permanent magnet provides the magnet flux in the magnetic circuit, as denoted by the green lines. For simplicity, only one DoF for the mover is considered. In addition, non-linear effects such as magnetic saturation and flux leakage are ignored in the reluctance tuning principles.

3.4.1. Principle A: exchange of reluctance

Principle A is based on the exchange of reluctance between two air gaps in a stator, as illustrated in Figure 3.3. The mover has the capability to move upward and its movement is represented by x. The displacement of the mover results in a reduction in the length of air gap 1 and an equal increase in the length of air gap 2. In the initial state, there is no air gap 2. If the surface areas of the stator and mover are identical, the total reluctance will remain constant as x changes. However, by reducing the surface area of the stator next to air gap 2, the change in the reluctance of air gap 2 is larger compared to the change in the reluctance of air gap 1. Thus, the total reluctance will increase as x changes. In case the displacement of x is sufficiently small compared to surface area A_R, the cross-section of air gap 2 can be approximated by A_R. Therefore, the increase in total reluctance $\Delta\mathfrak{R}_A$ by the movement of x is calculated as:

$$\Delta\mathfrak{R}_A = \frac{x(\frac{A}{A_R} - 1)}{\mu_0 A} \tag{3.4}$$

The ratio $\frac{A}{A_R}$ represents the reduction of the surface area and it starts to have a significant effect when A_R is at least two times smaller than A.

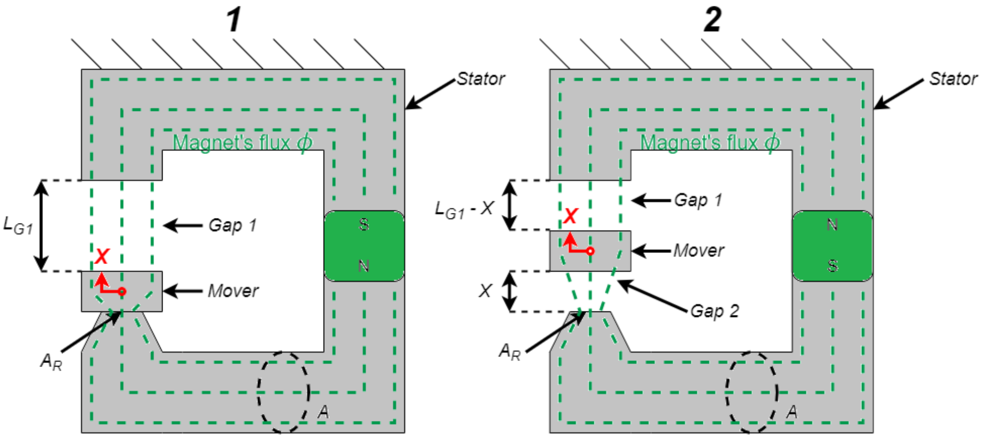

Figure 3.3: Reluctance tuning principle A

3.4.2. Principle B: expansion of gap length

Principle B is based on the expansion of the length of an air gap in a stator, as illustrated in Figure 3.4. The mover possesses the ability to move downward, and its displacement is represented by x. By movement of x the length of air gap 1 increases and therefore the total reluctance. In the initial state, there is no air gap 1. The change in total reluctance can be increased by a reduction of the surface area of the mover. Again, by assuming that the displacement of x is sufficiently small compared to A_R, the cross-section of air gap 1 can be approximated by A_R. To facilitate the displacement of the mover, a sliding surface A_S between the stator and mover is required. It is assumed that the surface area A_S remains unaffected by the displacement x because the length of the mover is sufficiently long. As a result, the reluctance of air gap 2 does not change by movement of x. Therefore, the increase in total reluctance $\Delta\mathfrak{R}_B$ by the movement of x is calculated as:

$$\Delta\mathfrak{R}_B = \frac{x}{\mu_0 A_R} \tag{3.5}$$

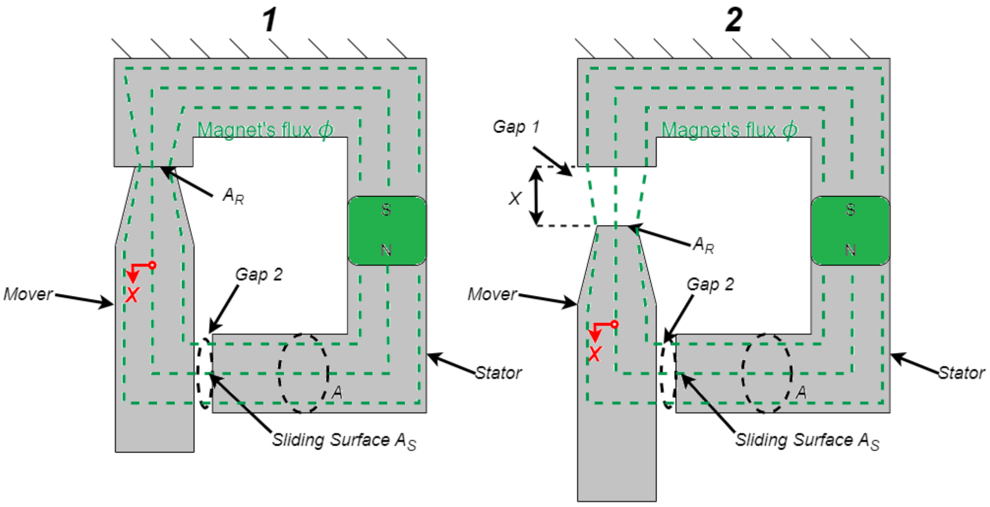

Figure 3.4: Reluctance tuning principle B

3.4.3. Principle C: reduction of gap cross-section

Principle C is based on the reduction of the cross-section of air gaps in a stator, as illustrated in Figure 3.5. The mover shifts to the left or right, and its displacement is denoted by x. Consequently, the width W of the air gaps between the stator and mover changes by the movement of x. Assuming $L_{G1} = L_{G2}$, the increase in total reluctance $\Delta\Re_C$ by the movement of x is calculated as:

$$\Delta\Re_C = \frac{2L_{G1}}{\mu_0(W-x)H} \tag{3.6}$$

where H is the height of the cross-section of the air gaps.

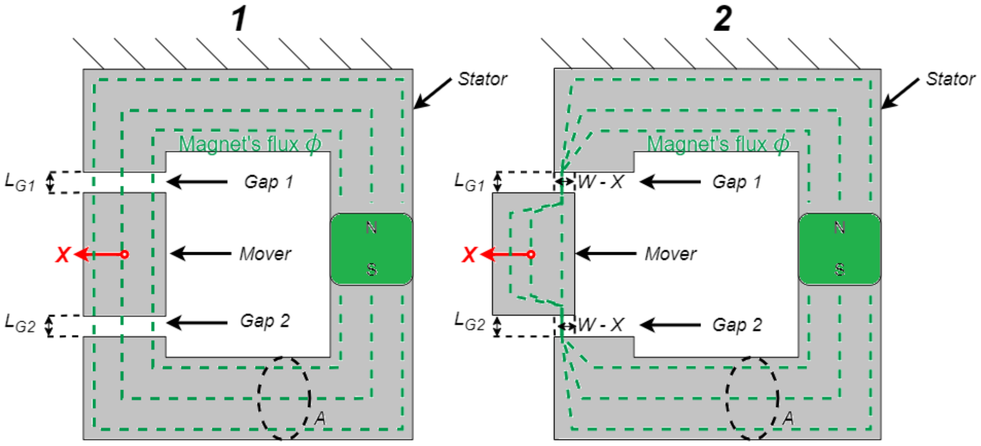

Figure 3.5: Reluctance tuning principle C

3.4.4. Comparison of principles

The effect of each principle on the change of total reluctance $\Delta\Re$ by the movement of x in $\mu\mathrm{m}$ is visualized in Figure 3.6. The parameter values used for the evaluation are based on realistic values commonly applied in reluctance actuators as seen in Appendix C.

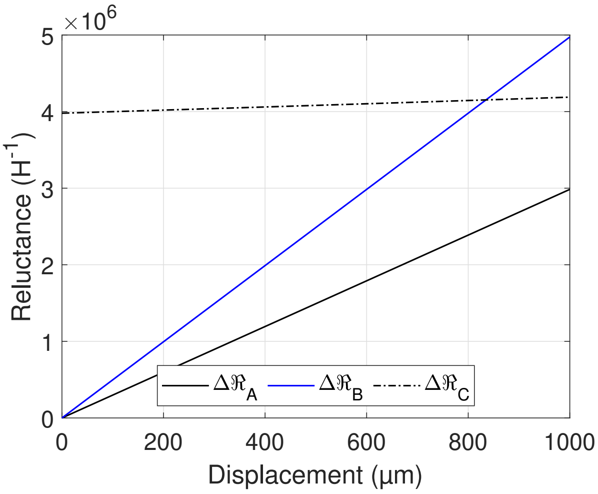

Figure 3.6: Analytical comparison of the reluctance tuning principles

Figure 3.6 clearly illustrates that principle B exhibits the steepest slope in $\Delta\Re$ relative to the other principles. The key advantages and disadvantages of each reluctance tuning principle are consolidated in Table 3.1. Despite principle B having the steepest slope in $\Delta\Re$, it involves the displacement of the largest mass compared to the other principles. This can have a detrimental impact on the dynamics, as a higher mass limits achievable acceleration. Principle A, on the other hand, concerns the displacement of a relatively small mass and it has a relatively modest difference in slope compared to principle B. Therefore, it is considered as the most interesting principle.

Table 3.1: Advantages and disadvantages of the reluctance tuning principles

Reluctance principle	Advantage	Disadvantage
A	Small mass of mover	Air gap 1 adds extra reluctance
B	Steepest slope in $\Delta\Re$	High mass of mover The sliding surface adds extra reluctance
C		Air gaps 1 and 2 add extra reluctance Least steepest slope in $\Delta\Re$

3.5. Conclusion chapter 3

The concept of reluctance tuning is introduced, involving the control of the length or cross-sectional area of an air gap within a stator. By controlling an air gap within the stator of an HRA, apart from the existing air gaps situated next to the mover, the reluctance can be changed on one side of the actuator with respect to the central axis. As a result, the magnetic flux unbalances on opposite sides of the mover and a magnetic force is induced on the mover. Three principles are formulated for reluctance tuning, each characterized by differences in the rate of change in reluctance they can generate and the size of the mover that needs displacement.

Principle A emerges as the most promising for integration into the design of an HRA. It relies on the displacement of a relatively small mass, advantageous for dynamic considerations. Additionally, Principle A exhibits a high rate of change in reluctance, though not the highest among the principles. Due to these favorable characteristics, it is considered to develop an HRA that incorporates principle A.

4

Actuator design and modeling

This chapter introduces the HRA design incorporating the selected reluctance tuning principle. It offers a perspective on examining the magnetic force of the actuator, utilizing both an analytical model and FEA model.

4.1. Design and working principle

Figure 4.1 shows the schematic overview of the developed actuator, referred to as the Piezo-Magnetic Actuator (PMA). It is based on the design of a HRA, however, without the coils and with the selected reluctance tuning principle. It consists of a soft ferromagnetic stator including a permanent magnet, three movers, four air gaps, and two piezoelectric actuators. In addition, there is an air gap between the mover and magnet, assumed to be fixed. The permanent magnet produces magnetic flux, which is distributed into two parallel magnetic circuits, resulting in flux on both sides of the central mover. In the initial state, the central mover is at its central position (x = 0) and both circuits are symmetric with reference to the central axis of the actuator. Thus, the magnetic flux on both sides of the central mover is equal and no magnetic force is exerted on the central mover.

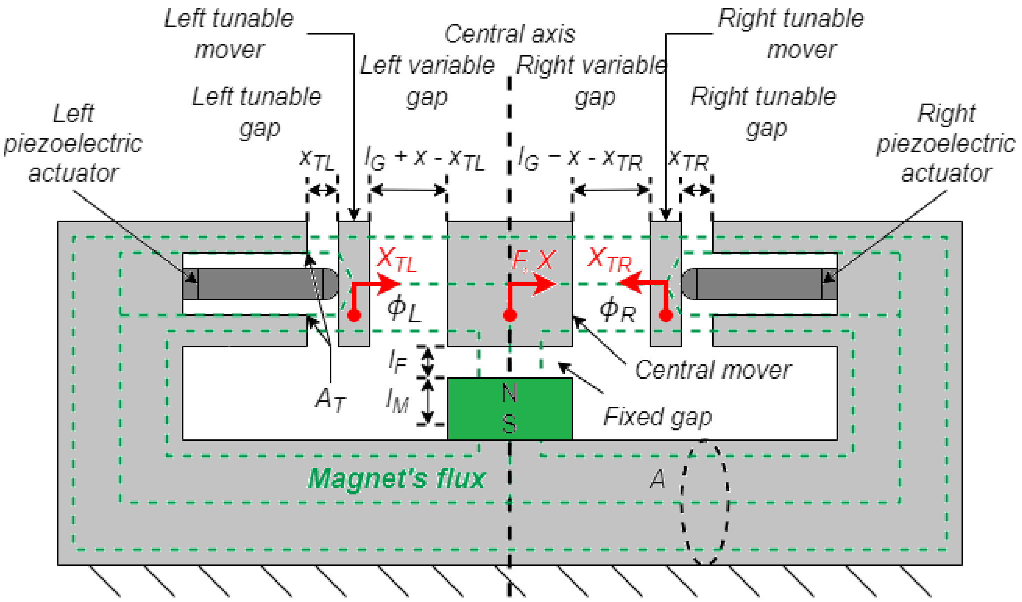

Figure 4.1: The Piezo-Magnetic Actuator

To unbalance the magnetic flux, the reluctance in one of the two parallel magnetic circuits is tuned. On each side of the central axis, the stator is connected to a mover driven by a piezoelectric actuator, referred to as a tunable mover. By actuation of the piezoelectric actuator, a tunable air gap is set between the stator and the tunable mover. This reduces the length of the already existing air gap next to the central mover. The generated tunable air gap has a smaller cross-section than the already existing air gap, thus the magnetic flux is now forced to pass through higher reluctance. As a result, the magnetic flux gets unbalanced near opposite sides of the central mover. This component is attracted to the stator with the higher magnetic flux. The magnetic force on the central mover increases as its displacement increases from the center position. By using the piezoelectric actuators in the said manner, as part of the HRA instead of the coils, the reluctance of the actuator can be tuned and the central mover can be directed to a required position.

4.1.1. Piezoelectric actuator implementation

The advantage of using piezoelectric actuators in this design is their relatively small volume, high force, high bandwidth, and low heat dissipation [3][4]. These actuators are material-based and by applying a voltage on the surface the material expands or contracts, depending on the polarity of the electric field [25]. Due to the small size, they fit into the stator as illustrated in Figure 4.1. Regarding energy losses, piezoelectric actuators do not dissipate any energy in a steady state, except for minimal current leakage. Consequently, the PMA can sustain a constant magnetic force on the central mover without experiencing heat dissipation. The tunable movers need to be displaced by piezoelectric actuators. Due to the small size of the generated tunable air gaps, a high magnetic force is exerted on the tunable movers. Piezoelectric actuators possess a high level of stiffness, thus making it relatively easy to compensate for the associated strong magnetic forces. Normally, piezoelectric actuators suffer from their poor disturbance rejection of vibrations transmitting through the piezoelectric actuator to the stage that needs to be positioned. However, in this design, there is no mechanical connection between the piezoelectric actuator and the central mover. A drawback of piezoelectric actuators is their limited actuation strain of order 0.1%. [26]. However, as mentioned before, a small air gap within a stator can already have a large impact on the total reluctance of a magnetic circuit.

Implementing pre-loading for piezoelectric actuators is essential for protection against tensile loads and enhancing strain output [27]. In this particular design, the chosen pre-loading technique is illustrated in Figure 4.2. The pre-load force is applied by tightening the leadscrew, causing the piezoelectric actuator to press against the flexure. While this method is straightforward and avoids inducing lateral forces on the piezoelectric actuator, it is important to highlight that the flexure, leadscrew, and preload block function as a mass-spring system with a resonance frequency lower than that of the piezoelectric actuator. This limitation tends to restrict the dynamic performance of the system [27]. The application of the selected pre-loading technique results in the initial length of the tunable air gaps within the developed actuator being not zero but rather a gap ranging from approximately $0.1\,\mathrm{mm}$ to $0.3\,\mathrm{mm}$.

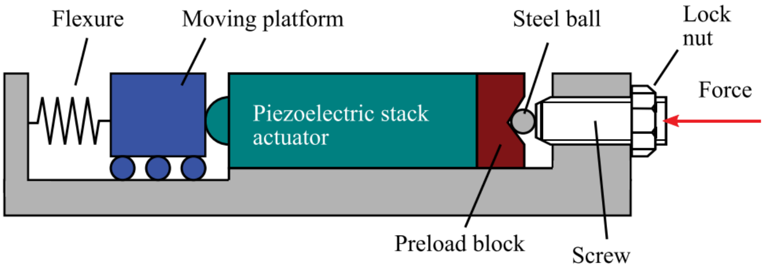

Figure 4.2: Pre-loading technique piezoelectric actuator [27]

4.2. Analytical model

To assess the magnetic force generated by the PMA, an analytical model of the magnetic circuit is developed as seen in Figure 4.3. In this model, it is assumed that the relative permeability of the soft ferromagnetic components is sufficiently large, such that the reluctance of the stator and movers can be ignored. The direct magnetic flux path from the magnet into the surrounding air is ignored. Non-linear effects such as magnetic hysteresis, fringing flux, and saturation are also neglected. Consequently, the derived model is only valid for flux densities smaller than the saturation flux density of the stator. In addition, the relative permeability of the magnet is assumed to be one. Due to the low relative magnetic permeability of piezoelectric actuators, it is assumed that no magnetic flux passes through the piezoelectric actuators.

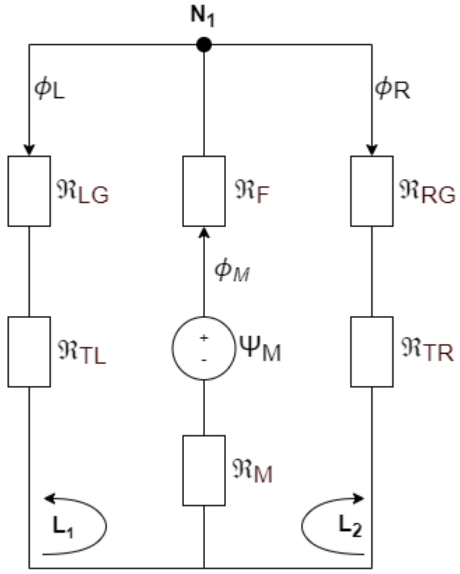

Figure 4.3: Analytical model of the magnetic circuit of the PMA

The reluctance of the left variable air gap $\Re_{LG}$, right variable air gap $\Re_{RG}$, left tunable air gap $\Re_{TL}$, right tunable air gap $\Re_{TR}$, fixed air gap $\Re_F$, and permanent magnet $\Re_M$ are modeled as:

$$\Re_{LG} = \frac{l_G + x - x_{TL}}{A_G \mu_0}, \Re_{RG} = \frac{l_G - x - x_{TR}}{A_G \mu_0}, \Re_{TL} = \frac{x_{TL}}{A_T \mu_0}, \Re_{TR} = \frac{x_{TR}}{A_T \mu_0}, \Re_F = \frac{l_F}{A_F \mu_0}, \Re_M = \frac{l_M}{A_M \mu_0} \quad (4.1)$$

where x is the variable position of the central mover relative to its center position, x_{TL} is the position of the left tunable mover, x_{TR} is the position of the right tunable mover, A_G is the cross-section the variable air gaps, A_T is the cross-section of the tunable air gaps, A_F is the cross-section of the fixed air gap, A_M is the cross-section of the magnet, μ_0 is the permeability of air or vacuum, l_G is the length of the left and right variable air gap when the central mover is in its center position ($x = 0$) and both tunable movers are positioned against the stator ($x_{TL} = 0$ and $x_{TR} = 0$), l_F is the fixed air gap length, and l_M is the permanent magnet length. For simplicity, the cross-sections A_G, A_M, and A_F are equal and set to A. As mentioned before, the selected pre-loading technique results in the initial length of the tunable air gaps within the developed actuator not being zero. Thus, the position of the tunable movers could be rewritten to:

$$x_{TL} = l_{PR} + x_{PL} \quad \text{and} \quad x_{TR} = l_{PR} + x_{PR} \quad (4.2)$$

where l_{PR} is the initial length of the tunable air gaps needed for pre-loading the piezoelectric actuators, and x_{PL} and x_{PR} represent the actuated displacement of the left and right piezoelectric actuators. By assuming a linear second quadrant BH-curve of the permanent magnet, the magnetomotive force of the permanent magnet Ψ_m is given by [23]:

$$\Psi_M = -H_c l_M \lambda \quad (4.3)$$

where H_c is the coercivity field strength, l_M is the length of the permanent magnet, and λ is the flux leakage factor of the permanent magnet to the variable air gaps.

By utilizing Hopkinson's law of magnetics, the magnetic flux of the permanent magnet ϕ_m is determined as [6][23]:

$$\phi_M = \frac{-H_c l_M \lambda}{\Re_F + \Re_M + \Re_P} \quad (4.4)$$

where $\mathfrak{R}_P$ is the total reluctance of the left variable and tunable air gaps and the right variable and tunable air gaps connected in parallel. By using Kirchhoff's circuit laws for magnetic circuits, the network equations in the closed loops and node are:

$$N_1 : \phi_M - \phi_L - \phi_R = 0 \tag{4.5}$$

$$L_1 : \phi_M(\mathfrak{R}_M + \mathfrak{R}_F) + \phi_L(\mathfrak{R}_{LG} + \mathfrak{R}_{TL}) = \Psi_M \tag{4.6}$$

$$L_2 : \phi_M(\mathfrak{R}_M + \mathfrak{R}_F) + \phi_R(\mathfrak{R}_{RG} + \mathfrak{R}_{TR}) = \Psi_M \tag{4.7}$$

Solving these equations gives the magnetic flux in the variable air gaps next to the central mover. The magnetic force on the central mover for a single DoF in the direction of x is calculated by using the Maxwell stress tensor, the complete derivation is presented in Appendix D. The equation of the force can be formulated as an expression that depends on the position of the tunable movers x_{TL} and x_{TR}, as well as the position x of the central mover:

$$F_{PMA} = K_{PM}\left(x_{TL} - x_{TR} + \frac{\frac{A}{A_T} - 1}{2l_G}\left(x_{TL}^2 - x_{TR}^2\right) + \frac{x\left(x_{TL} + x_{TR}\right)}{l_G}\right) + k_a x \tag{4.8}$$

where K_{PM} is referred to as the piezo-magnetic coefficient and k_a is the actuator stiffness, given by:

$$K_{PM} = \left(\frac{H_C^2 l_M^2 \lambda^2 A \mu_0 l_G (\frac{A}{A_T} - 1)}{\left(\left(2l_G + (\frac{A}{A_T} - 1)x_{TL} + (\frac{A}{A_T} - 1)x_{TR}\right)\left(l_M + l_F\right) + \left(l_g + x + (\frac{A}{A_T} - 1)x_{TL}\right)\left(l_G - x + (\frac{A}{A_T} - 1)x_{TR}\right)\right)^2}\right) \tag{4.9}$$

$$k_a = \left(\frac{2H_C^2 l_M^2 \lambda^2 A \mu_0 l_G}{\left(\left(2l_G + (\frac{A}{A_T} - 1)x_{TL} + (\frac{A}{A_T} - 1)x_{TR}\right)\left(l_M + l_F\right) + \left(l_G + x + (\frac{A}{A_T} - 1)x_{TL}\right)\left(l_G - x + (\frac{A}{A_T} - 1)x_{TR}\right)\right)^2}\right) \tag{4.10}$$

The derived magnetic force equation is non-linear. In addition, notice that both the piezo-magnetic coefficient and actuator stiffness are non-linear and not constant. The flux leakage factor λ depends on the position of x, x_{TL}, and x_{TR}, which makes it difficult to determine this coefficient analytically. For this reason, FEA software is employed to assess and estimate the flux leakage factor. The FEA software is also utilized to explore the impact of fringing flux. This evaluation is summarized in Appendix H.

4.2.1. Magnetic force analysis

Figure 4.4 plots the derived magnetic force for increasing position of the left tunable mover in the range x_{TL} = $[200\,\mu\mathrm{m}, 220\,\mu\mathrm{m}, 240\,\mu\mathrm{m}, 260\,\mu\mathrm{m}, 280\,\mu\mathrm{m}, 300\,\mu\mathrm{m}]$, while varying the position x of the central mover in the range $-600\,\mu\mathrm{m}$ to $600\,\mu\mathrm{m}$ with increments of $30\,\mu\mathrm{m}$. The initial position of the tunable movers is set to $200\,\mu\mathrm{m}$, a value presumed to be sufficient for pre-loading the piezoelectric actuators. The increase in the position of the left tunable mover represents the actuated displacement of the left piezoelectric actuator. Typically, the order of displacement range of standard stacked piezoelectric actuators is ranging from $10\,\mu\mathrm{m}$ to $100\,\mu\mathrm{m}$, and therefore this displacement range is employed in the evaluation of the derived magnetic force. The used values for the design parameters of the actuator are presented in Appendix E. Figure 4.4 shows that the magnetic force on the central behaves highly linearly in the examined ranges. As the position of the left tunable mover increases, the magnetic force also increases, exhibiting negative stiffness behavior. The blue line depicts the points where the position of the central mover remains stable. With an increase in the position of the left tunable mover, the stable position of the central mover shifts to the left, thus towards the left tunable mover. A parametric evaluation is performed to identify the individual influence of the design parameters on the magnetic force on the central mover in its center position ($x = 0$) and the results are shown in Table 4.1

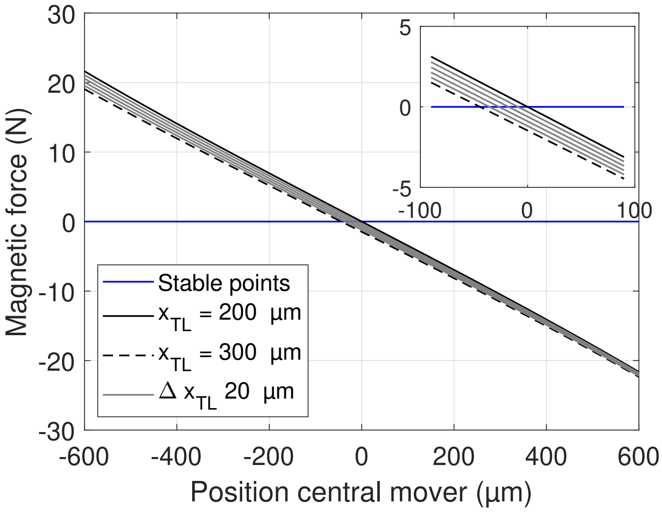

Figure 4.4: Evaluation of the analytical model for increasing position of the left tunable mover x_{TL}, while varying the position of the central mover x.

Table 4.1: Parametric analysis of magnetic force

Increase of parameter	Effect on magnetic force	Description
L_G	-	Variable air gap length
l_M	+	Magnet length
l_F	-	Fixed air gap length
H_c	+	Coercivity field strength of magnet
A	+	Area of stator, movers, variable air gaps, and magnet
A_T	-	Area of tunable air gaps

4.2.2. Maximum magnetic force potential

To get preliminary knowledge of the potential maximum force of the PMA, an evaluation is employed for the PMA incorporating a smart material that can displace $800\,\mathrm{mm}$. This is already possible for motion-amplified piezoelectric actuators, which are piezoelectric actuators in combination with flexures as depicted in Figure 4.5a [28]. However, to integrate such a mechanism into the PMA would require a redesign. Figure 4.5b plots the derived magnetic force for increasing position of the left tunable mover in the range $200\,\mu\mathrm{m}$ to $1000\,\mu\mathrm{m}$. In this configuration, the central mover can only be displaced to the right. Again, the initial position of the tunable movers is set to $200\,\mu\mathrm{m}$. The used values for the design parameters of the actuator are presented in Appendix E. These design parameters are not optimized. Figure 4.5b shows that a significantly higher magnetic force can be achieved, especially when the central mover is at its center position ($x = 0$). The increase in magnetic force is relatively small at the outer ends of the parameter range. It is crucial to emphasize that this evaluation disregards the impact of increasing fringing flux. When enlarging the tunable air gap, the influence of fringing flux also intensifies, leading to a reduction in the maximum magnetic force of the actuator.

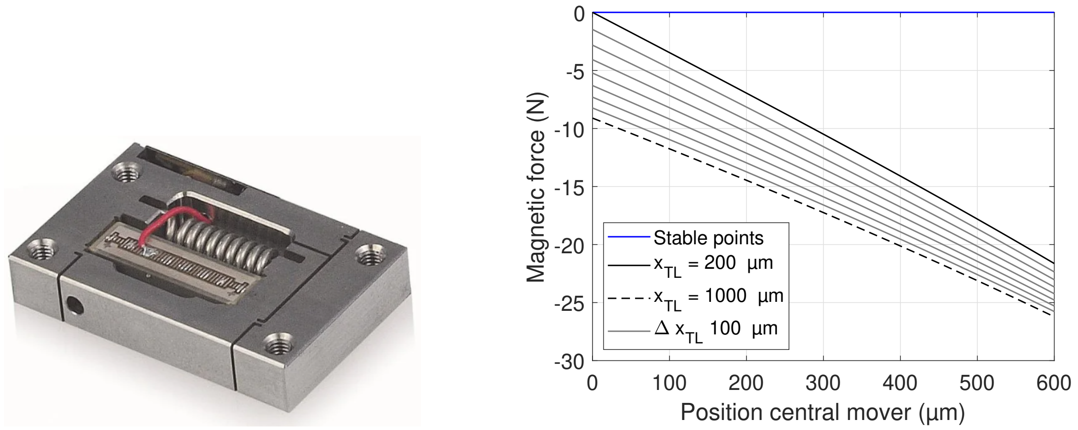

(a) Motion-amplified piezoelectric actuator [28]

(b) Maximum magnetic force potential analyisis

Figure 4.5: Maximum magnetic force potential of the PMA incorporating smart material that can displace $800\,\mu\text{m}$

4.2.3. Linearity analysis analytical model

By assuming that the position of the central mover is zero ($x = 0$) and the initial positions of the tunable movers are equal, Equation 4.8 can be rewritten to an expression that depends on a linear element, a nonlinear element, and the actuated displacement of the left piezoelectric actuator x_{PL}:

$$F_{PMA} = \underbrace{K_{PM}x_{PL}}_{\text{Linear element}} + \underbrace{K_{PM}\alpha x_{PL}^2}_{\text{Non-linear element}} \quad \text{and} \quad \alpha = \frac{\frac{A}{A_T} - 1}{2l_G} \tag{4.11}$$

Equation 4.11 is evaluated in Figure 4.6 for increasing displacements of the left piezoelectric actuator x_{PL} in the range $0\,\mu\text{m}$ to $800\,\mu\text{m}$ with increments of $10\,\mu\text{m}$. The used values for the design parameters of the actuator are presented in Appendix E. Again, the initial position of the tunable movers is set to $200\,\mu\text{m}$.

Figure 4.6 shows that with an increasing displacement of the piezoelectric actuator, the slope of the linear element decreases, while the slope of the non-linear element remains relatively constant. The reduction in the slope of the linear element is attributed to the variable nature of the piezo-magnetic coefficient concerning changes in x_{PL}. In the detailed view, it becomes apparent that both elements exhibit highly linear behavior when the range of the left piezoelectric actuator is less than $100\,\mu\text{m}$. Therefore, limiting the displacement of the piezoelectric actuator allows for the generation of a highly linear magnetic force on the central mover.

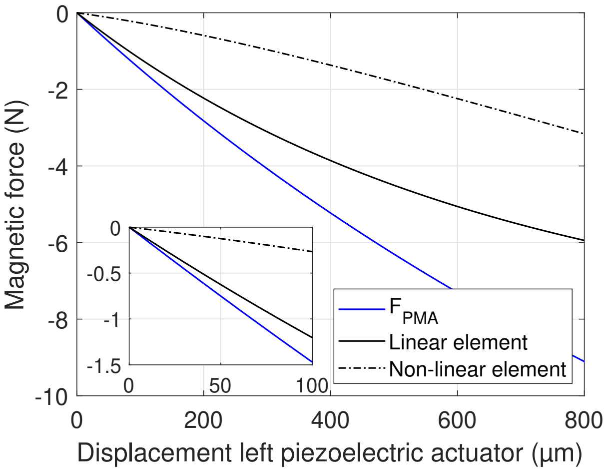

Figure 4.6: Linearity analysis of the magnetic force of the PMA

4.3. Hybrid Reluctance Actuator and Piezo-Magnetic Actuator comparison

The developed PMA is compared to an equivalent HRA. In this evaluation, the PMA design incorporates two standard Thorlabs PK4GA7P1 stacked piezoelectric actuators [29]. This specific actuator was chosen for its notable features, including a relatively large displacement range of $100\,\mu\mathrm{m}$, low capacitance of $16\,\mu\mathrm{F}$, and a low drive voltage of $150\,\mathrm{V}$. The HRA design under evaluation comprises two coils, each with 100 windings and a resistance of $2.4\,\Omega$ [30]. Both actuators adhere to the design parameters outlined in Appendix D. It is crucial to emphasize that the values used for these design parameters are not optimized.

4.3.1. Force comparison

If the central mover of both the PMA and the HRA is in the center position ($x = 0$), the magnetic force equations can be simplified to:

$$F_{HRA} = K_m I \quad \text{and} \quad F_{PMA} = K_{PM}(x_{PL} + \alpha x_{PL}^2) \tag{4.12}$$

These equations are examined in Figure 4.7. It is clear that the magnetic force produced by the HRA considerably exceeds that of the developed PMA, even within a relatively low current range.

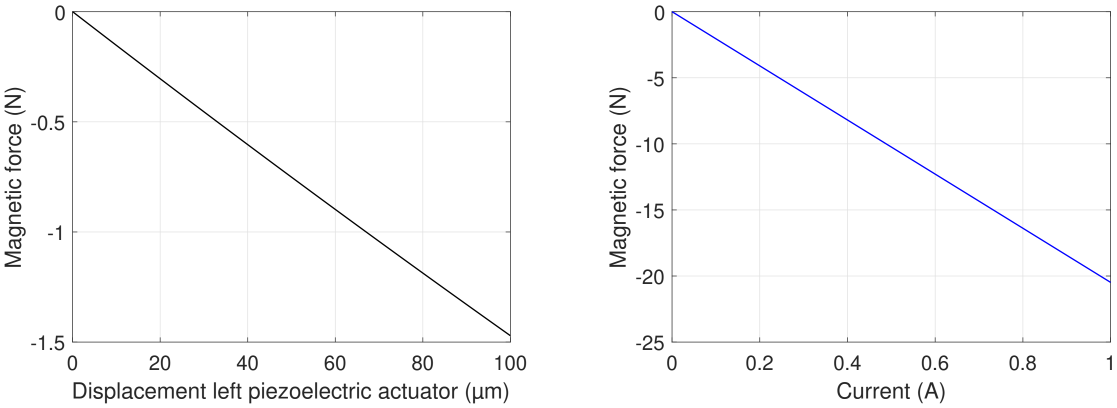

(a) Magnetic force of the developed PMA

(b) Magnetic force of an HRA with 100 windings per coil

Figure 4.7: Magnetic force comparison PMA and HRA

4.3.2. Heat dissipation comparison

When a piezoelectric actuator is set to maintain a static position, its one-time actuation cycle dissipates energy. Once in position, only its very low leakage current needs to be compensated. By disregarding this leakage current, the PMA can sustain a constant force on the central mover without any heat dissipation. An HRA can only maintain a constant force when it continuously supplies current to the coils. Thus, during static operations, the developed PMA will dissipate considerably less heat compared to an HRA.

To assess whether the developed PMA is an improvement to the HRA in dynamic heat dissipation, the Break-even Tuning Interval (BTI) metric is employed. This metric is also utilized in studies comparing the heat dissipation of Tunable Magnetic Actuators and electromagnetic permanent devices to equivalent electromagnetic actuators [9][10]. For the Tunable Magnetic Actuator, the interval is defined as the time required between magnetization tuning cycles, ensuring that the tunable magnetic actuator dissipates the same amount of energy as an equivalent electromagnetic actuator [9]. In this thesis, the metric is slightly adapted for the developed PMA to determine the time required between actuation cycles of the piezoelectric actuator in the PMA to match the energy loss of an equivalent HRA, and it is calculated as:

$$T_{BTI} = \frac{E_{PMA,cycle}}{P_{HRA}} \tag{4.13}$$

where $E_{PMA,cycle}$ is the energy dissipation of a piezoelectric actuator in one actuation cycle and is P_{HRA} the steady-state power dissipation of the HRA. For simplicity, heat dissipation by eddy currents and magnetic hysteresis are ignored.

According to piezoelectric actuator suppliers Thorlabs [31] and PI [32], the power dissipation P_{PMA} and the energy dissipation of a piezoelectric actuator in one actuation cycle $E_{PMA,cycle}$ can be approximated by:

$$P_{PMA} \approx \frac{\pi \tan(\delta) U_{pp}^2 f C}{4} \quad \text{and} \quad E_{PMA,cycle} \approx \frac{\pi \tan(\delta) U_{pp}^2 C}{4} \tag{4.14}$$

where $\tan\delta$ is the Dissipation Factor (DF), C is the capacitance of the actuator, and U_{pp} is the peak-to-peak driving voltage. The term DF in piezoelectric actuators denotes the ratio of the energy dissipated as heat to the energy stored in the material during each cycle of mechanical deformation, typically ranging from 0.01 to 0.02. This ratio depends on factors such as mechanical pre-load, temperature, control frequency, and the quantity of passive material [32]. As seen in Equation 4.14, power dissipation varies proportionally with the frequency of the applied voltage signal. In an HRA, heat is dissipated due to the current that flows through the conductive wire of the coils. This is calculated as:

$$P_{HRA} = I^2 R \tag{4.15}$$

where I is the applied current and R is the resistance.

As seen in Figure 4.7a, if one piezoelectric actuator in the developed PMA displaces $100\,\mu\text{m}$ the magnetic force on the central mover is $1.47\,\text{N}$. To achieve this force with an equivalent HRA, a relatively small continuous current of approximately $0.07\,\text{A}$ is required. The piezoelectric actuators inside the PMA dissipate more energy by applying a large peak-to-peak voltage. Therefore it is interesting to assess the BTI metric for increasing peak-to-peak voltage in the range of $1\,\text{V}$ to $150\,\text{V}$ with increments of $1\,\text{V}$, as depicted in Figure 4.8a. This figure illustrates that the BTI non-linearly increases as the peak-to-peak voltage rises. In the worst-case scenario of a $150\,\text{V}$ peak-to-peak voltage, the TBI is $2.4 \times 10^{-1}\,\text{s}$. In the best-case scenario of a $1\,\text{V}$ peak-to-peak voltage, the TBI is $1.07 \times 10^{-5}\,\text{s}$. Following basic sampling rules, it is possible to approximate a sinusoidal force trajectory using ten constant force samples taken at regular intervals. With this consideration, an energy-efficiency bandwidth F_{EBW} can be derived, for which the PMA dissipates less energy compared to an equivalent HRA, and it is calculated as [11]:

$$F_{EBW} = \frac{1}{10 T_{BTI}} \tag{4.16}$$

This equation is evaluated in Figure 4.8b, which demonstrates a substantial increase in the energy-efficiency bandwidth for smaller peak-to-peak voltages. It is crucial to note that the dissipation factor of a piezoelectric actuator is not constant for increasing frequencies. Therefore, Figure 4.8b only serves to illustrate the energy-efficiency bandwidth potential of the PMA.

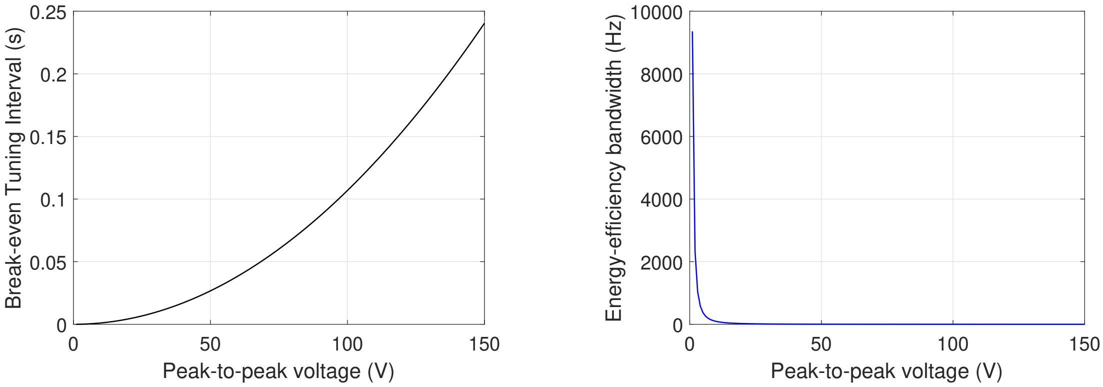

(a) Break-even Tuning Interval calculated for increasing peak-to-peak voltage applied to one of the piezoelectric actuators of the developed PMA

(b) Energy-efficiency bandwidth calculated for increasing peak-to-peak voltage applied to one of the piezoelectric actuators of the developed PMA

Figure 4.8: Heat dissipation comparison of a HRA and PMA

A more detailed representation of the calculated BTI and F_{EBW} values for various peak-to-peak voltages is shown in Table 4.2. It shows that for a realistic peak-to-peak voltage of $10\,\mathrm{V}$ an energy-efficiency bandwidth can be achieved of $93.58\,\mathrm{Hz}$. The comparison in heat dissipation is currently grounded on a magnetic force of $1.47\,\mathrm{N}$. Nevertheless, optimizing the PMA design will result in an enhanced energy-efficiency bandwidth. The greater the output force generated by the PMA using the same piezoelectric actuator, the more heat will be dissipated by the equivalent HRA due to the quadratic scaled current seen in Equation 4.15.

Table 4.2: BTI and energy-efficiency bandwidth

U_{pp}	T_{BTI}	F_{EBW}
$150\,\mathrm{V}$	$2.4 \times 10^{-1}\,\mathrm{s}$	$0.41\,\mathrm{Hz}$
$100\,\mathrm{V}$	$1.07 \times 10^{-1}\,\mathrm{s}$	$0.94\,\mathrm{Hz}$
$50\,\mathrm{V}$	$2.67 \times 10^{-2}\,\mathrm{s}$	$3.74\,\mathrm{Hz}$
$25\,\mathrm{V}$	$6.68 \times 10^{-3}\,\mathrm{s}$	$14.97\,\mathrm{Hz}$
$10\,\mathrm{V}$	$1.07 \times 10^{-3}\,\mathrm{s}$	$93.58\,\mathrm{Hz}$
$5\,\mathrm{V}$	$2.67 \times 10^{-4}\,\mathrm{s}$	$374.33\,\mathrm{Hz}$

4.4. Finite Element Analysis model

To accurately account for nonlinearities such as fringing flux, flux leakage, and saturation, a 3D model of the designed actuator is created and simulated using COMSOL Multiphysics® [33], as depicted in Figure 4.9. The actuator is positioned within a sizable air box to effectively model flux leakage and fringing flux. The soft ferromagnetic components are modeled by unlaminated S235JRC+C(SH) [34] and the permanent magnet is modeled as a sintered NdFeB N42 [35]. The discretization used for the magnetic field physics interface is second order Lagrange. In each simulation, local adaptive mesh refinement is employed to validate the accuracy of the model. Mesh refinements continue until the model results exhibit less than a 1% variation compared to the previous mesh. When this criterion is met in two successive refinements, convergence is achieved. The initial mesh utilizes a COMSOL built-in physics-controlled mesh set to a finer resolution. In this FEA model, local adaptive mesh refinement is applied to the mesh of the movers, air gaps, and the permanent magnet. A detailed explanation of the used settings in the FEA model is presented in Appendix F. The validation of convergence for each performed simulation is detailed in Appendix G.

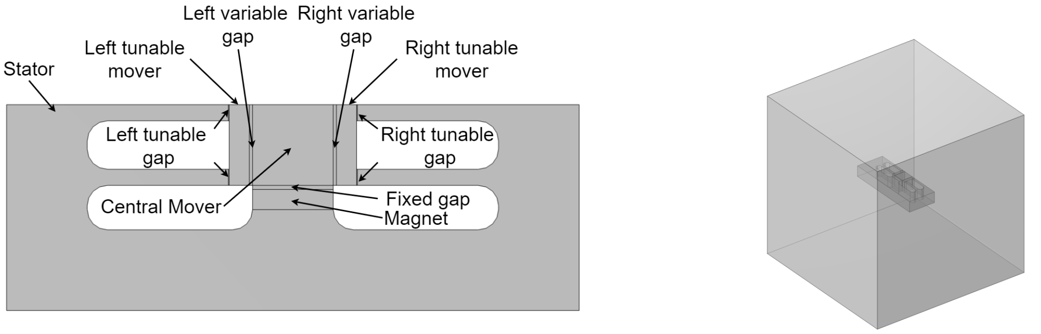

(a) Front view of the 3D model (b) Complete overview of the 3D model: actuator in an air box

Figure 4.9: 3D model of the actuator in COMSOL Multiphysics®

4.4.1. Comparison analytical model and Finite Element Analysis model

The magnetic force on the central mover is evaluated for both the analytical model and the FEA model for increasing position of the left tunable mover in the range x_{TL} = [200 µm, 210 µm, 220 µm, 230 µm, 240 µm], while varying the position x of the central mover in the range -600 µm to 600 µm with increments of 30 µm. Again, the initial position of the tunable movers is set to 200 µm, a value presumed to be sufficient for pre-loading the piezoelectric actuators. The increase in the position of the left tunable mover represents the actuated displacement of the left piezoelectric actuator. For this evaluation, the PMA design incorporates two PiezoDrive SA050520 stacked piezoelectric actuators [36], featuring a length of 20 mm, a maximum displacement range of 31 µm, and a drive voltage of 150 V. The used values for the design parameters of the actuator are presented in Appendix E. The computation of the flux leakage factor and the effect of fringing flux can be seen in Appendix H

The comparison of magnetic force between the analytical model and FEA model is illustrated in Figure 4.10a. This graph reveals that the magnetic force simulated by the FEA model widens at the outer ends of the position of the central mover. This outcome aligns with expectations, as the flux leakage factor and fringing flux are dependent on the position of the central mover. In the analytical model, these factors are treated as static values for simplicity. The percentage error between the results is graphed as a function of x in Figure 4.10b. In the range of -200 µm to 200 µm, the percentage error is below 4%. The percentage error increases towards the outer ends of the parameter range due to the influence of changing flux leakage and fringing flux. The elevated percentage error near $x = 0$ is attributed to the magnetic force approaching 0 N.

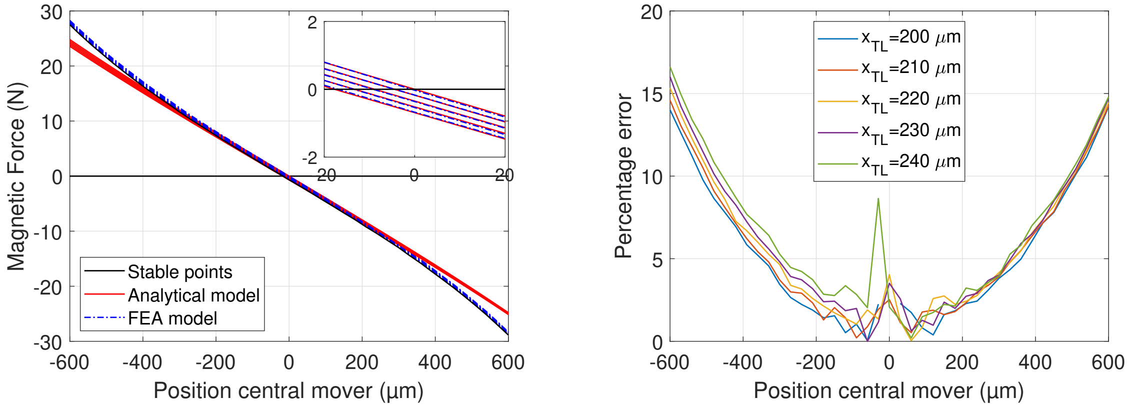

(a) The magnetic force on the central mover evaluated for both the analytical model and the FEA model (b) The percentage error between the results of the analytical model and the FEA model

Figure 4.10: Comparison analytical model and FEA model

4.4.2. Magnetic force on tunable movers

Besides using the FEA model to validate the analytical model, it is used to investigate the behavior of the tunable movers. The tunable movers also experience a magnetic force exerted upon them and this force changes with the position of the central mover and their own position. The magnetic force acting upon both tunable mover is simulated for increasing position of the left tunable mover in the range x_{TL} = $[200\,\mu\mathrm{m},\ 210\,\mu\mathrm{m},\ 220\,\mu\mathrm{m},\ 230\,\mu\mathrm{m},\ 240\,\mu\mathrm{m}]$, while varying the position x of the central mover in the range $-600\,\mu\mathrm{m}$ to $600\,\mu\mathrm{m}$ with increments of $30\,\mu\mathrm{m}$. The initial position of the tunable movers is set to 200 µm. Figure 4.11a depicts the force characteristics of the left tunable mover. Similar to the central mover, it exhibits negative stiffness behavior. As the position of the central mover approaches $600\,\mu\mathrm{m}$, the force acting on the left tunable mover reduces. It is anticipated that a turnover point exists, where the direction of the force on the tunable mover undergoes a change. The same phenomenon applies to the force exerted on the right tunable mover. Although not discernible in the graphs, in practical terms, this turnover point could signify that if the central mover is too close to one of the tunable movers, the latter may be drawn toward the central mover, resulting in an unwanted collision. Hence, flexures are essential not only for pre-loading the piezoelectric actuators but also for preserving the set position of the tunable movers.

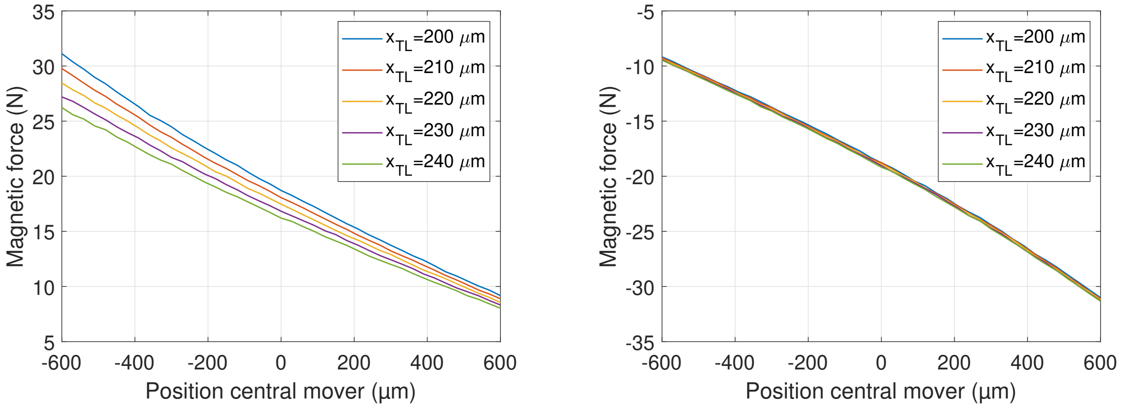

(a) Force behavior on the left tunable mover for varying positions of the central

(b) Force behavior on the right tunable mover for varying positions of the central

Figure 4.11: Magnetic force investigation on the tunable movers by using the 3D FEA model

4.5. Conclusion Chapter 4

The design and analysis of reluctance tuning in an HRA show that a magnetic force can be generated on a soft ferromagnetic mover without the implementation of coils. This design is referred to as the Piezo-Magnetic Actuator, in short PMA. The tuning of reluctance is realized by displacement of two tunable movers each driven by a piezoelectric actuator, creating a tunable air gap in the stator and locally changing the reluctance. The analytical model shows that the behavior of the magnetic force exerted on the central mover, the mover of interest, depends on two constants: the piezo-magnetic coefficient and the actuator stiffness. By ignoring the actuator stiffness, the magnetic force exhibits highly linear behavior for the displacement of one tunable mover in ranges below $100\,\mu\mathrm{m}$.

Comparing the magnetic force generated by the developed PMA with that of an equivalent HRA, the latter considerably surpasses the former. However, the PMA dissipates no energy in steady to maintain in comparison to the HRA for generating the same magnetic force. An energy-efficiency bandwidth metric is used to compare the heat dissipation of the PMA to an equivalent HRA in dynamic operations. It shows that for relatively low applied peak-to-peak voltage to the piezoelectric actuators in the PMA, the PMA is more energy efficient, even at high frequencies.

To validate the analytical model, it is compared to an FEA model of the PMA, revealing a 4% percentage error for central mover displacements within the range of $-200\,\mu\mathrm{m}$ to $200\,\mu\mathrm{m}$. The percentage error increases outside of this range due to the analytical model treating flux leakage and fringing flux as static values, whereas in reality, these factors depend on the position of the central mover.

5

Experimental Demonstrator and Tests

This chapter gives detailed insight into the constructed demonstrator of the developed PMA and the results of the performed measurements.

5.1. Piezo-Magnetic Actuator setup

An overview of the built PMA demonstrator is presented in Figure 5.1. It consists of three sub-assemblies: the actuator, central mover, and tunable movers. More comprehensive explanations for each sub-assembly are provided in the subsections that follow. The actuator dimensions are based on the design parameters presented in Appendix E. Each sub-assembly is separately mounted by bolts on an aluminum breadboard or construction rails of Thorlabs [37]. The position of the central mover is measured by an optoNCDT 2300 sensor, which is an optical system for measurements with a resolution of maximum $0.03\,\mu\mathrm{m}$ and offers an adjustable measuring rate of up to $49.14\,\mathrm{kHz}$ [38]. To set the piezoelectric actuators in motion, a function generator RS PRO RDSG 830 is employed [39]. The generated voltage signal is then amplified by a gain of 15 using a BPA100 Piezo Amplifier [40]. Both the signals from the generator and the optical system are logged by a USB-6008 DAQ device from National Instruments, featuring a maximum sample rate of $10\,\mathrm{kS/s}$ [41]. By logging two signals at the same time and using an oversample rate of ten to ensure accurate reproduction of the signals, the setup achieves a maximum measurement frequency of $500\,\mathrm{Hz}$. The data is processed in LabVIEW [42] and the used block diagram is presented in Appendix I.

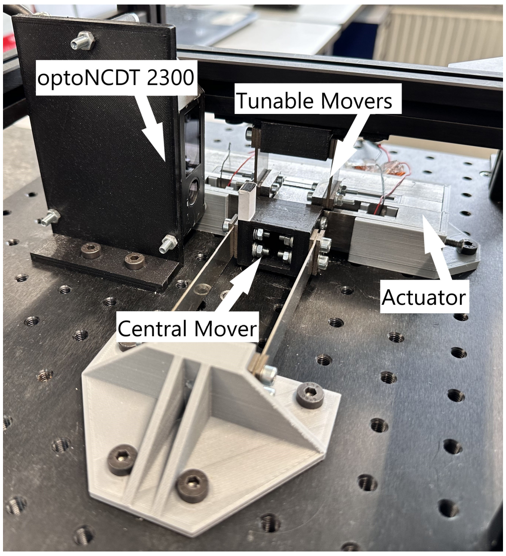

Figure 5.1: Overview of the built PMA demonstrator

5.1.1. Actuator

The constructed actuator is illustrated in [34]. The stator, consisting of S235JRC+C(SH), incorporates a sintered Neodymium-Ferite-Boron (NdFeB) N42 magnet [35]. Within the stator, two PiezoDrive SA050520 stacked piezoelectric actuators are positioned [36]. The leadscrews are utilized for preloading the piezoelectric actuators. All the components are held in place by the 3D-printed enclosure made of PolyLactic Acid (PLA).

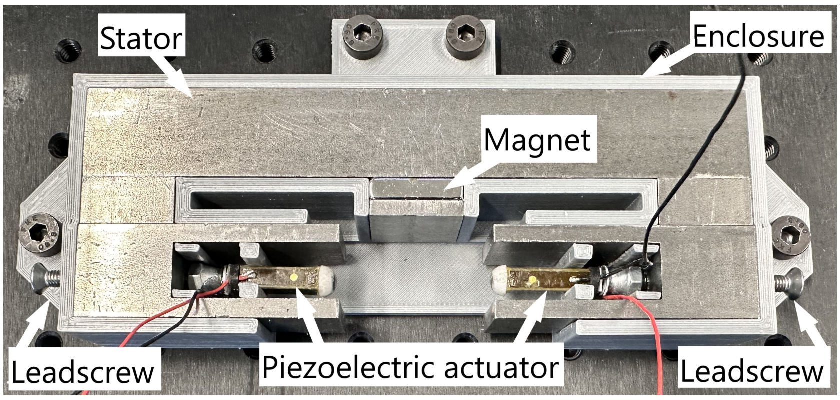

Figure 5.2: Overview of the built actuator

5.1.2. Central mover

The built central mover is depicted in Figure 5.3. The mover block, composed of S235JRC+C(SH) with a weight of $80.5\,\mathrm{g}$, is secured within a 3D-printed PLA holder using two bolts. To provide guidance and compensate for the negative stiffness, two parallel stainless steel flexures are employed. These flexures are mounted on a 3D-printed PLA fixture, which is linked to the breadboard. To perform open-loop measurements flexures are needed, otherwise the system is always unstable. Each flexure measures $100\,\mathrm{mm}$ in length, $16\,\mathrm{mm}$ in width, and $1\,\mathrm{mm}$ in thickness with a weight of $12\,\mathrm{g}$. The laser of the optoNCDT 2300 is focused on the white stick attached to the holder. It is presumed that this measuring point can accurately depict the displacement of the moving block caused by the linear guidance of the two parallel flexures. Furthermore, considering that the maximum displacement of the central mover is $1\,\mathrm{mm}$, any parasitic displacements in other directions are expected to be relatively small.

The stiffness of the central mover k_{CM} is evaluated through an experiment by loading and unloading the mover block in its center. See Appendix J for an explanation of the performed stiffness measurement. By utilizing a first-degree polynomial fit on the measurement data, the linear stiffness is estimated to be $7.73\,\mathrm{kN/m}$.

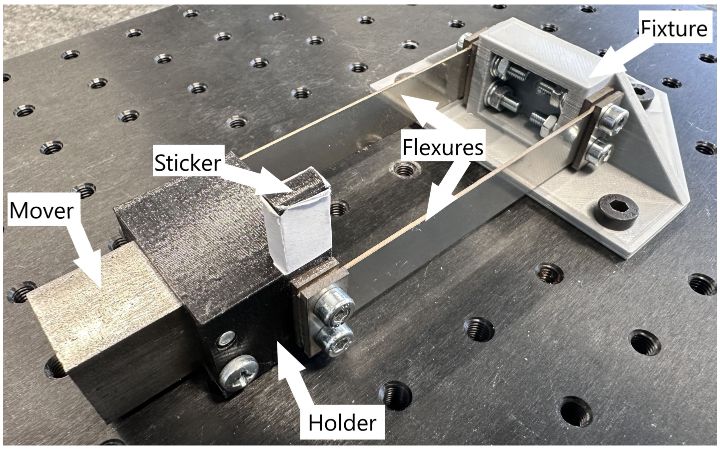

Figure 5.3: Overview of the built central mover

5.1.3. Tunable movers

The assembled tunable movers are depicted in Figure 5.4. Comprised of S235JRC+C(SH) with a weight of $20.5\,\mathrm{g}$, each tunable mover is attached to a stainless steel flexure. These flexures are mounted on the fixture, which is linked to the construction rail. By fastening the piezoelectric actuators against the tunable mover using the leadscrews of the actuator, the flexures provide the pre-loading force against the piezoelectric actuators. Dimensions for each flexure are $36\,\mathrm{mm}$ in length, $20\,\mathrm{mm}$ in width, and $1.5\,\mathrm{mm}$ in thickness with a weight of $8\,\mathrm{g}$.

The stiffness of the tunable movers k_{TM} is assessed in an experimental configuration by loading and unloading one of the tunable movers at its center. Refer to Appendix J for a description of the conducted stiffness measurement. Employing a first-degree polynomial fit on the measurement data gives an estimated linear stiffness of approximately $18.07\,\mathrm{kN/m}$.

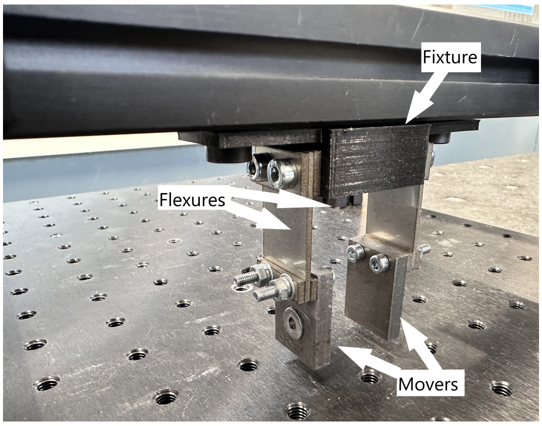

Figure 5.4: Overview of the built tunable movers

5.2. Method

The procedure for each conducted measurement is outlined in the following subsections. Figure 5.5 visualizes the open-loop diagram of the experimental setup.

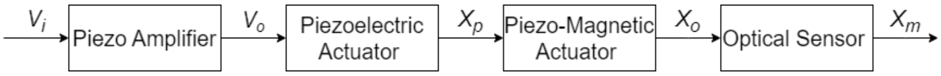

Figure 5.5: Open-loop diagram of the experimental setup

5.2.1. Pre-loading the piezoelectric actuators

Before conducting measurements, the piezoelectric actuators were pre-loaded by tightening the leadscrews by approximately $200\,\mu\mathrm{m}$. In this setup, the pre-loading force was approximately $3.6\,\mathrm{N}$. After applying the pre-loading, the nut on each leadscrew is fastened and secured in place with glue.

5.2.2. Displacement behavior

In the initial test, the displacement range of one of the piezoelectric actuators was measured by positioning the central mover against a tunable mover, which is connected to the piezoelectric actuator of interest. In this configuration, the negative stiffness of the actuator was dominant over the stiffness of the central mover. Consequently, the central mover connects indirectly to the piezoelectric actuator, and its displacement accurately mirrors the displacement of the piezoelectric actuator. The displacement range was assessed for a voltage signal starting from $15\,\mathrm{V}$ to $150\,\mathrm{V}$ in increments of $7.5\,\mathrm{V}$. The initial voltage setting was set to $15\,\mathrm{V}$ and not $0\,\mathrm{V}$ to improve the actuation behavior of the piezoelectric actuator. In the second test, the position of the central mover was measured in a free state. An increasing voltage signal is applied to the same piezoelectric actuator from the previous test. Once more, the voltage was incrementally raised, beginning at $15\,\mathrm{V}$ and reaching $150\,\mathrm{V}$ in increments of $7.5\,\mathrm{V}$.

5.2.3. Open-loop frequency response

In the third test, the open-loop frequency response of the system was assessed by applying a sequence of five sinusoidal voltage sweeps consecutively to one of the piezoelectric actuators. During this test, the position of the central mover was measured. Each sweep signal initiated from $1\,\mathrm{Hz}$ and progressed to $500\,\mathrm{Hz}$ while lasting for a duration of $60\,\mathrm{s}$. To investigate the non-linear behavior of the system, the frequency response is performed with different amplitudes of the sinusoidal voltage sweep. The low-level voltage of the signal was always set to $15\,\mathrm{volts}$, while the high-level voltage of the signal spans from $90\,\mathrm{V}$ to $150\,\mathrm{V}$ in increments of $15\,\mathrm{V}$. Subsequently, MATLAB software was employed to estimate the transfer functions of the frequency responses [43]. The used MATLAB settings and the validation of the results are presented in Appendix K.

5.2.4. Open-loop time response

In the fourth test, the open-loop time response of the setup was assessed for different voltage trajectory signals, including sinusoidal, triangular, and step responses. For each waveform, the frequency is varied to $1\,\mathrm{Hz}$, $5\,\mathrm{Hz}$, and $10\,\mathrm{Hz}$, which is slightly below the first resonance frequency of the system of about $23\,\mathrm{Hz}$. The used peak-to-peak voltage of the signals was set to $15\text{-}150\,\mathrm{V}$.

5.3. Experimental results and discussion

5.3.1. Displacement behavior: magnetic displacement amplification

Figure 5.6a shows the measured displacement of both the central mover and the piezoelectric actuator as the voltage is incrementally increased. At $150\,\mathrm{V}$ the piezoelectric actuator displaces approximately $18.2\,\mathrm{\mu m}$. This is slightly lower than the expected maximum displacement of approximately $20.92\,\mathrm{\mu m}$ $\pm 10\%$ according to the specifications provided by PiezoDrive, see Appendix L. This discrepancy can be attributed to the magnetic force exerted on the tunable mover, directed towards the piezoelectric actuator, serving as additional pre-loading and consequently limiting the maximum displacement range of the piezoelectric actuator.

Concurrently, at $150\,\mathrm{V}$, the central mover displaces approximately $54.61\,\mathrm{\mu m}$, which is larger than that of the piezoelectric actuator. The ratio between the displacement of the central mover and piezoelectric actuator is plotted in Figure 5.6b. The displacement ratio exhibits an increasing trend with larger displacements of the piezoelectric actuator. This phenomenon can be further optimized by either reducing the stiffness of the central mover or enhancing the maximum magnetic force output of the PMA. The observed amplification ratio between the central mover and the piezoelectric actuator is referred to as magnetic displacement amplification.

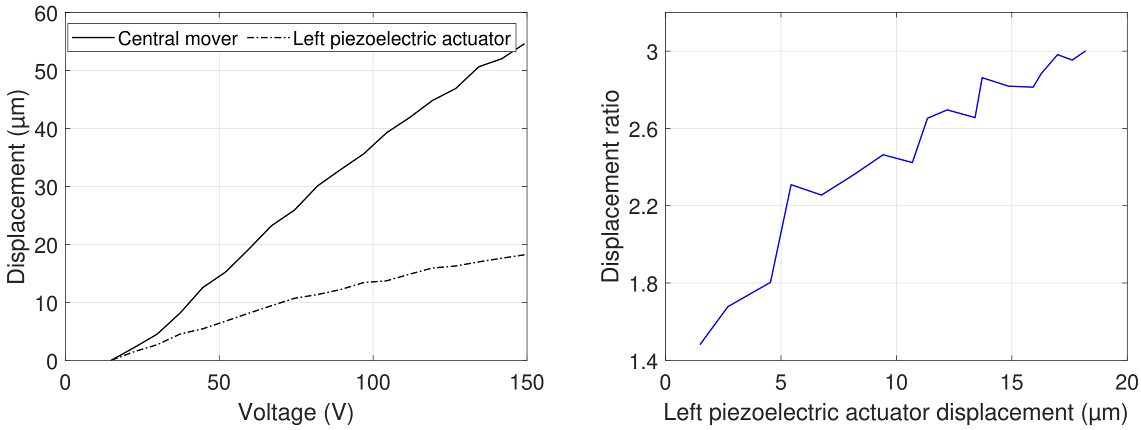

(a) Measured displacement of the central mover and left piezoelectric actuator for increasing voltage

(b) Displacement ratio between the central mover divided by the left piezoelectric actuator

Figure 5.6: Displacement behavior of the system for increasing voltage

5.3.2. Comparison analytical model and experimental results

The measured displacement of the central mover is compared to the analytical model by modifying Equation 4.8 to:

$$k_{CM}x = K_{PM}\left(x_{TL} - x_{TR} + \frac{\frac{A}{A_T} - 1}{2l_G}\left(x_{TL}^2 - x_{TR}^2\right) + \frac{x\left(x_{TL} + x_{TR}\right)}{l_G}\right) + k_a x \tag{5.1}$$

where K_{CM} is the measured stiffness of the central mover. By using this equation, the position of the central mover x is determined for increasing displacement of the left piezoelectric actuator. The calculations are based on the same actuator dimensions and specifications seen in Appendix E. Figure 5.7 shows the measured and calculated displacement of the central mover. It is important to highlight that the magnetic field strength of the magnet had to be adjusted to $423\,\mathrm{kA/m}$ to get similar displacement behavior of the central mover at the outer end of the displacement range. This is a factor of 0.56 smaller than the specifications provided by the magnet supplier [35]. This unexpected difference is crucial to investigate in future research by measuring the magnetic field strength of the magnet.

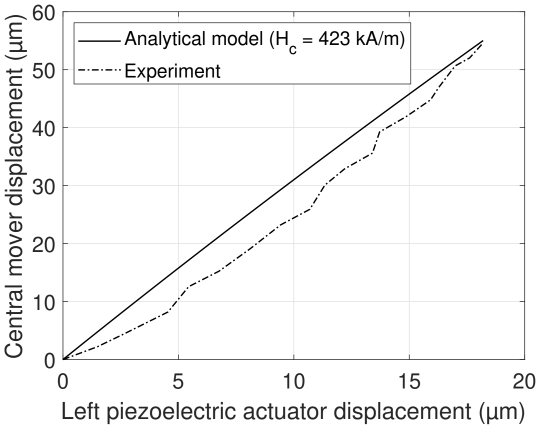

Figure 5.7: Measured displacement of the central mover compared to the analytical model

5.3.3. Open-loop frequency response

The open-loop frequency response of the system, under different voltage signals, is illustrated in Figure 5.8, covering a range of up to $100\,\mathrm{Hz}$. In the Bode plot, the amplitude corresponds to the displacement of the central mover in mm in response to the applied voltage signal in V. At lower frequencies, the horizontal line measures g_{PMA} $=2.51\,\mathrm{kV/mm}$. The frequency responses of the system for the different voltage signals exhibit similarity. The analytical model of the PMA predicted linear behavior in the case only one piezoelectric actuator is actuated with a relatively small displacement range. The first resonance peak occurs at $f = 23\,\mathrm{Hz}$, attributed to the lower stiffness of the flexures linked to the central mover. Notably, eliminating these flexures could shift the first resonance peak to significantly higher frequencies, thereby enhancing the dynamics of the actuator. However, it is crucial to emphasize that in this configuration, control becomes essential to uphold the stability of the actuator. Another option is to increase the stiffness of the flexures, but this will result in a reduction of magnetic force output on the central mover.

The open-loop frequency response of the actuator is approximated by a single mass-spring-damper system as illustrated in Figure 5.8. Instead of relying on the measured horizontal line and first resonance frequency seen in Figure 5.8, which are not known in advance, an alternative approach is adopted to estimate the frequency response of the system. It is assumed that the natural frequency of the central mover f_n approximates the first resonance peak:

$$f_n = \frac{1}{2\pi}\sqrt{\frac{k_{est}}{m_{est}}} = 21.4\,\mathrm{Hz} \tag{5.2}$$

The stiffness is estimated by:

$$k_{est} = k_{CM} - k_a(x_0) = 1.96\,\mathrm{kN/m} \tag{5.3}$$

where k_{CM} is the stiffness of the central mover and $k_a(x_0)$ is the actuator stiffness at $x = 0$ with the adjusted H_c = $423\,\mathrm{kA/m}$. The estimated stiffness reflects the parallel connection between the central mover and actuator stiffness of the actuator. The mass is estimated by:

$$m_{est} = m_{CM} + 2m_{fl} = 104.5\,\mathrm{g} \tag{5.4}$$

where m_{CM} designates the measured mass of the mover block and m_{fl} denotes the measured mass of one flexure. By using an iterative approach to get similar damping behavior as the measured frequency response, the damping coefficient is estimated by $c_{est} = 2\zeta\sqrt{k_{est}m_{est}}$ = $8\,\mathrm{Ns/m}$ with a damping ratio of $\zeta = 0.23$. The amplitude plot in Figure 5.8 shows the relatively small difference in gain at low frequency between the mass-spring-damper approximation and the measured frequency response. Figure 5.8 also indicates a relatively small phase lag between the mass-spring-damper system and the measured frequency responses. The discrepancy in phase lag is likely attributable to the hysteresis behavior in the 3D-printed PLA components.

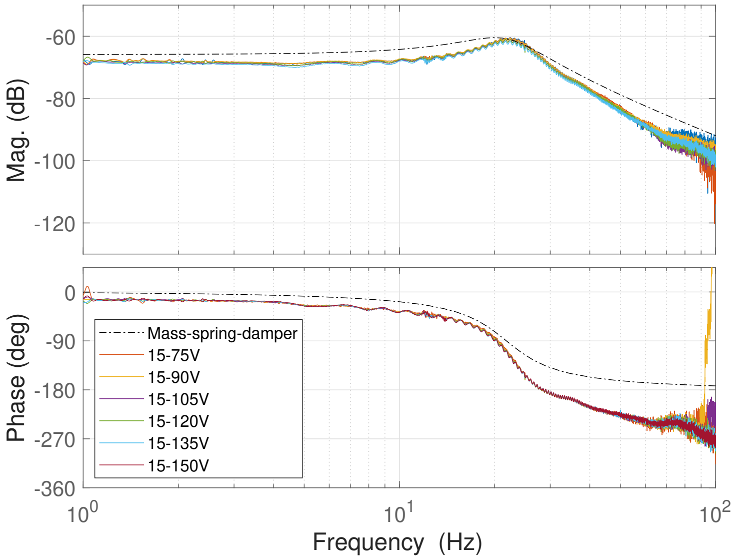

Figure 5.8: Open-loop Frequency response of the built demonstrator for different voltage amplitudes including an equivalent mass-spring-damper system

5.3.4. Open-loop time response

Figure 5.9 and Figure 5.10 show the open-loop time response of the system for three sinusoidal and three triangular voltage signals with different frequencies. The 15-150 V input signals are scaled to fit in these plots as well. The output displacement of the central mover can follow the input voltage relatively well. However, after reaching the maximum voltage of an input signal the output displacement shows a widening effect, which enlarges for higher frequencies. This phenomenon is likely a result of the hysteresis behavior exhibited by the 3D-printed PLA components. At $1\,\mathrm{Hz}$, the input voltage and output displacement of the central mover move almost together in phase. The mentioned small phase lag at low frequency is visible here as well. At $10\,\mathrm{Hz}$, the influence of the first resonance peak introduces a larger phase lag between the signals. It can be seen that the measured displacement of the central mover is not smooth. Although the supplier of the optical sensor claims to offer a maximum resolution of $0.03\,\mu\mathrm{m}$, in practice it was only $1.36\,\mu\mathrm{m}$.

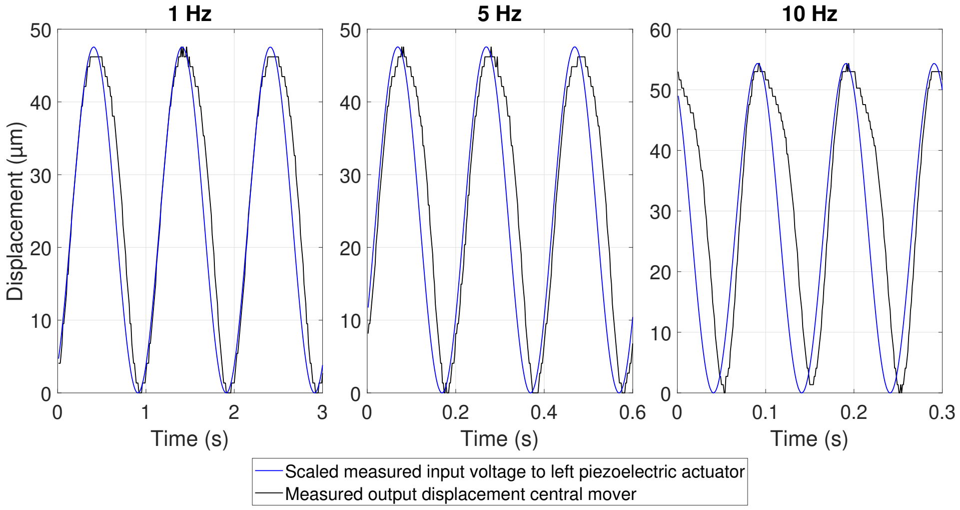

Figure 5.9: Open-loop time response of the built demonstrator for sinusoidal voltage signals with different frequencies

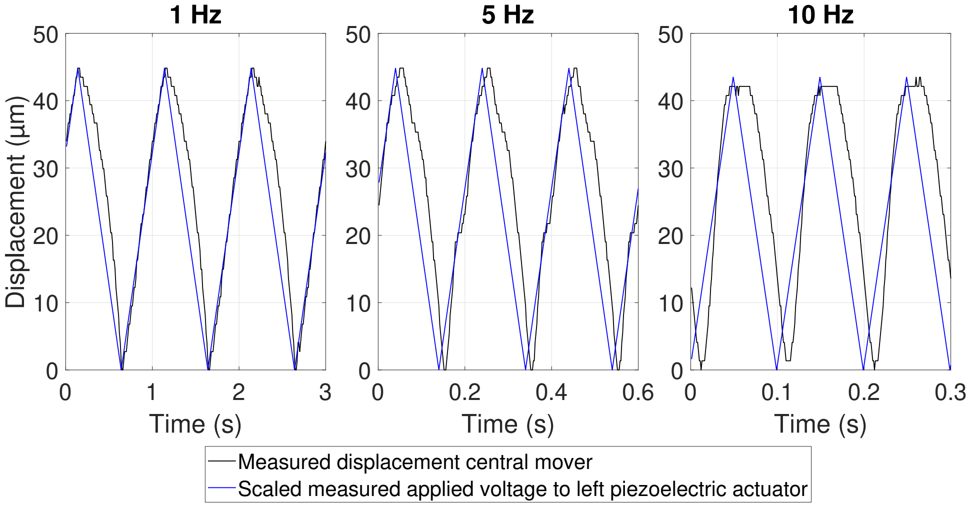

Figure 5.10: Open-loop time response of the built demonstrator for triangular voltage signals with different frequencies

Figure 5.11 shows the open-loop time response of the system for three step input signals with different frequencies. At $1\,\mathrm{Hz}$, the output displacement of the central is able to reach steady state before every new step input. This is not the case anymore for the input signal with $5\,\mathrm{Hz}$ and gets even worse for the input signal with $10\,\mathrm{Hz}$. Furthermore, large overshoot behavior is seen, which can lead to oscillations or instability in the system.

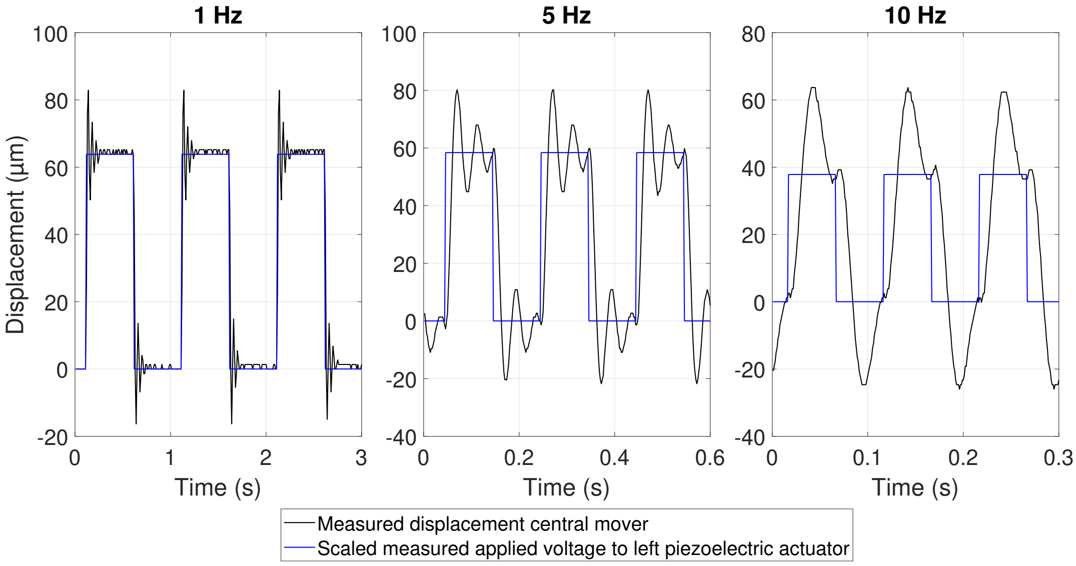

Figure 5.11: Open-loop time response of the built demonstrator for step input voltage signals with different frequencies

5.4. Conclusion chapter 5

The experimental demonstrator proofs that the central mover can undergo magnetic displacement through the motion of a piezoelectric actuator without using coils. Moreover, it establishes the existence of a ratio between these displacements, termed as magnetic displacement amplification. This ratio can be enhanced by employing flexures with reduced stiffness for the central mover or by optimizing the design of the PMA to generate greater magnetic force. The currently built PMA is capable of displacing the central mover magnetically by $54.61\,\mu\mathrm{m}$, utilizing a single piezoelectric actuator with a displacement of $18.2\,\mu\mathrm{m}$.

The open-loop frequency response of the experimental demonstrator for the different voltage amplitudes exhibits similarity below $100\,\mathrm{Hz}$, allowing for approximation by a single mass-spring-damper system. The first resonance peak arises at $23\,\mathrm{Hz}$ due to the low stiffness of the flexures linked to the central mover, which were needed to ensure open-loop stability of the experimental demonstrator. Eliminating these flexures could shift the first resonance peak to significantly higher frequencies, thereby enhancing the dynamics of the actuator. This change does require a controller to ensure the stability of the system. The open-loop time response demonstrates that, at lower frequencies, the output displacement of the central mover can effectively track an input voltage signal. Nevertheless, owing to the low first resonance peak at $23\,\mathrm{Hz}$, a substantial phase lag emerges between the two signals already at low frequencies.

6

Conclusion, recommendations, future research, potential, and applications

6.1. Conclusion

The objective of this thesis was to design, validate, and build a Hybrid Reluctance Actuator featuring a novel alternative to the coils to reduce heat dissipation. The novel alternative had to be energy-efficient in both static and dynamic operations while not contributing to the total reluctance of the actuator when uncontrolled. The innovative solution designed in this thesis, known as reluctance tuning, fulfills these specified requirements. It introduces extra air gaps in the stator of an HRA, besides the already existing air gaps next to the mover. The additional gaps, controlled by adjusting their length, alter the reluctance, causing an unbalance in the magnetic flux and inducing a magnetic force on the mover. The integration of reluctance tuning into an HRA led to the design of the Piezo-Magnetic Actuator, in short PMA, as illustrated in Figure 6.1, utilizing piezoelectric actuators to control the lengths of the added air gaps in the stator. Although the initial length of these gaps contributes to the total reluctance when uncontrolled, their impact is relatively small compared to the existing air gaps next to the mover.

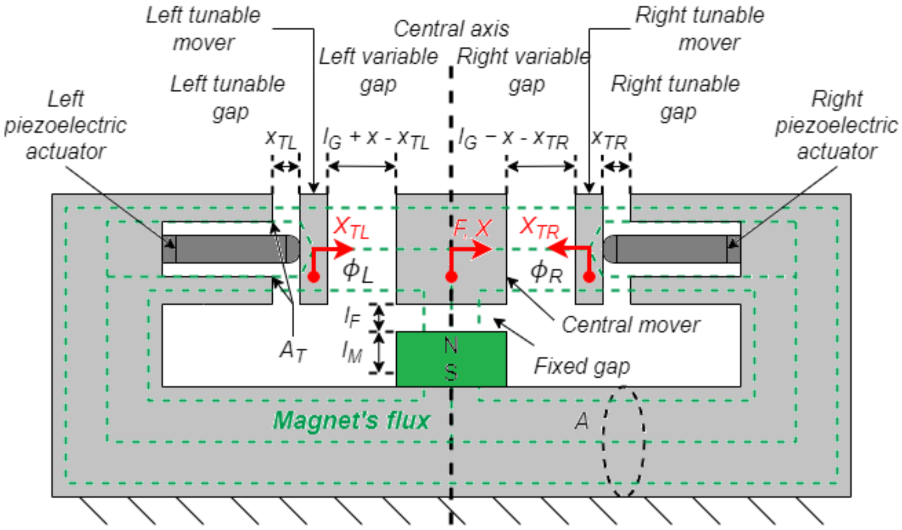

Figure 6.1: The developed PMA

Validation of the behavior of the designed actuator was achieved through an analytical model and FEA model. The analytical model revealed that the magnetic force output depends on the piezo-magnetic coefficient and actuator stiffness, exhibiting highly linear behavior for displacements of one piezoelectric actuator below $100\,\mu\mathrm{m}$. The FEA model demonstrated a 4% percentage error between the analytical model for displacements of the mover within the range of $-200\,\mu\mathrm{m}$ to $200\,\mu\mathrm{m}$, affirming that the analytical model can be used effectively.

In terms of energy efficiency, the PMA dissipates no energy in steady state to maintain the magnetic force, when disregarding the current leakage of piezoelectric actuators, while an HRA does. An energy-efficiency bandwidth metric is used to compare the heat dissipation of the PMA with that of an equivalent HRA during dynamic operations aimed at generating the same magnetic force. It shows that for relatively low peak-to-peak voltage applied to the piezoelectric actuators, the PMA is more energy efficient, even at high frequencies. However, the maximum force output of the currently designed PMA is rather low compared to an equivalent HRA.

The experimental demonstrator verified the ability of the actuator to displace the central mover through the displacement of piezoelectric actuators magnetically, and not by using coils. Moreover, it establishes the existence of a ratio between these displacements, termed as magnetic displacement amplification. This ratio can be enhanced by employing flexures with reduced stiffness attached to the mover or by optimizing the design of the PMA to generate greater magnetic force. The currently built PMA is capable of displacing the central mover magnetically by $54.61\,\mu\mathrm{m}$, utilizing a single piezoelectric actuator with a displacement of $18.2\,\mu\mathrm{m}$. The open-loop frequency response of the experimental demonstrator shows similarities for various voltage amplitudes applied to the piezoelectric actuators below $100\,\mathrm{Hz}$, enabling an approximation by a single mass-spring-damper system. The first resonance peak of the experimental demonstrator, at $23\,\mathrm{Hz}$, is attributed to the low stiffness of the flexures connected to the central mover, essential for open-loop stability. The removal of these flexures has the potential to shift the first resonance peak to much higher frequencies, thereby improving the dynamics of the developed actuator. However, implementing this change necessitates a controller to ensure the stability of the system. The open-loop time response reveals that, at lower frequencies, the displacement of the mover can accurately follow a voltage signal. However, due to the low first resonance peak at $23\,\mathrm{Hz}$, a significant phase lag arises between the two signals, even at low frequencies.

6.2. Recommendations and further research

The results of this thesis show that it is possible to design an actuator that displaces a mover magnetically without using coils. Although the results are promising, the actuator is not yet ready for implementation in the industry. For this reason, the key recommendations and future research topics are summarized and prioritized below.

6.2.1. Recommendations

1. Verify the specifications of standard parts. Strongly recommended is the verification of magnet specifications before their integration into the experimental setup. In this thesis, the magnetic field strength of the utilized magnet appears to be approximately 50% weaker than what the supplier claims. The strength of the magnet is an important factor in the actuator because it is a non-linear factor in the piezo-magnetic coefficient. Additionally, it is advisable to conduct tests on the magnetic saturation and relative permeability of the soft ferromagnetic material employed in the actuator.

2. Change the piezoelectric actuator type. The stacked piezoelectric actuators used in the experimental demonstrator effectively validated the novel working principle of PMA. However, it is recommended to switch to ring piezoelectric actuators characterized by low capacitance, low drive voltage, and a substantial displacement range. These properties contribute to minimal heat dissipation and the ability to generate a large air gap. Ring piezoelectric actuators offer advantages such as a larger surface area, facilitating more effective cooling and suitability for higher frequencies. Their larger outer diameter also provides the benefit of reduced sensitivity to tensile loads. Additionally, it is advisable to drill a hole in the stator that precisely matches the dimensions of the piezoelectric actuator, enhancing the guidance and alignment of the actuator. If necessary, custom-made piezoelectric actuators can be procured specifically for integration into the PMA. Another option is to explore the integration of motion-amplified piezoelectric actuators into the PMA. While this would necessitate a redesign of the

PMA, it holds the potential to enhance the maximum magnetic force because these mechanisms can provide a much larger displacement range over standard stack and ring piezoelectric actuators.

3. Optimize the design of the PMA. The design of the PMA is not optimized, and it is recommended to enhance the maximum magnetic force output by optimizing the design of the actuator. In this thesis, standard unlaminated construction steel was used to construct the stator, but it is suggested to improve this by using laminated pure iron to reduce the relative permeability and the impact of eddy currents. The use of a stronger flat magnet is recommended to generate a higher magnetic force on the central mover. Additionally, optimizing factors like flux leakage and fringing flux are advised. Placing the flexures of the central mover along the direction of gravity is also suggested to eliminate the moment exerted on the mover by gravity and improve the alignment. Moreover, a modification in the pre-loading technique is suggested. The tunable air gaps initially have a specific gap size due to the currently selected technique. This leads to an increase in the total reluctance of the actuator, thereby reducing the maximum magnetic force output on the central mover. For optimization, it is recommended to utilize the analytical model instead of the FEA model, as accurately simulating magnetic circuits in FEA requires a long simulation time. The FEA model should only be used to determine the flux leakage and fringing flux and to validate the final analytical model.

4. Improve sensors and data logging. In practice, the used optical sensor for measuring the displacement of the central mover had a resolution of $1.36\,\mu\mathrm{m}$. This led to poor measurement results. In order to measure the frequency response of the actuator at higher frequencies and to improve the open-loop time response, it is a must to use a position measurement sensor with higher resolution. Additionally, it is recommended to incorporate two additional position sensors, enabling simultaneous measurement of the displacements of the tunable and central movers. Handling increased data sampling concurrently necessitates a higher sample rate. Furthermore, considering the potential for flux control, it may be valuable to measure the magnetic flux in the actuator. To validate the claim of lower heat dissipation, installing temperature sensors on various components within the actuator is advised.

5. Use materials with higher magnetic saturation and relative permeability. It is recommended to investigate materials with higher magnetic saturation for use in the stator of the actuator. Reluctance tuning incorporates a stator with a reduced surface area. As the surface area of the stator decreases, there is a corresponding increase in magnetic flux density in that region. If the magnetic flux density surpasses a certain threshold, known as magnetic saturation, further reductions in surface area cease to yield any additional benefits. However, employing materials with higher magnetic saturation amplifies the impact of reluctance tuning, thereby increasing the maximum magnetic force output. Ideally, selecting materials with low relative permeability ensures that the reluctance of the stator remains as low as possible.

6. Improve manufacturing and alignment tolerances. The soft ferromagnetic components of the actuator are made by turning and drilling, resulting in manufacturing tolerances of $0.1\,\mathrm{mm}$. These relatively small tolerances still introduce asymmetry to the actuator, significantly impacting the performance of the PMA. To enhance precision, it is recommended to outsource all components for finer tolerances. Additionally, the use of 3D-printed parts made of plastics is discouraged due to their hysteresis behavior and inadequate stiffness. These parts also undergo material property changes over time, affecting the dynamics of the PMA. To address this, it is suggested to utilize non-ferromagnetic materials like aluminum for the enclosure and fixtures of the actuator. Another issue is the suboptimal alignment of the central mover within the actuator. This alignment could be improved by creating the central mover and actuator as a monolithic structure.

6.2.2. Future research

1. Apply feedback or feedforward control. All measurements conducted in this thesis were in an open-loop configuration. To enhance the performance of the actuator, it is interesting to investigate suitable control methods for the PMA. Typically, HRAs are controlled through current or flux control, and these methods remain intriguing for application in the PMA. The incorporation of piezoelectric actuators also opens the door to alternative approaches, including sensing the position of the piezoelectric actuators or implementing charge control.

2. Control the PMA with minimal or zero compensation for negative stiffness. While the flexures of the central mover contribute to open-loop stability, they reduce the dynamic performance of the constructed PMA. The main contributor to the first resonance peak at $23\,\mathrm{Hz}$ is the low stiffness of the central mover. Removing the flexures is expected to enhance the dynamics, However, in this configuration control is a must. Otherwise, the system will always collide against the stator.

3. Measure the magnetic force response of the PMA by using a load cell. At present, the examination of the open-loop behavior and dynamics of the actuator relies on measuring the displacement of the central mover for various voltage signals. Alternatively, fixing the central mover against a load cell can be employed to measure the magnetic force response of the PMA. This eliminates the low resonance frequency introduced by the flexures of the central mover, enabling more accurate measurements at higher frequencies. Additionally, it allows for ignoring the negative stiffness of the constructed PMA, which simplifies the setup.

4. Develop a PMA for a specific application. Right now, the developed PMA is a universal design and not specifically designed for any application in the high-precision industry. It is recommended to investigate potential applications that align with the strengths of the PMA and to adapt the design to excel in those applications.

5. Explore other options for displacing the tunable movers. In this thesis it was decided to use piezoelectric actuators for the displacement of the tunable movers. Although these actuators have low heat dissipation and are small in size, they have a limited displacement range. It is suggested to explore other smart materials, mechanisms, actuators, or motors to set the tunable air gaps in the stator.

6. Design a multi-DoF actuator while using the concept of reluctance tuning. The presently designed PMA is capable of magnetically displacing the central mover in a single DoF. To enhance the relevance of the actuator in industrial applications, it is recommended to explore new actuator configurations employing the principle of reluctance tuning. The application of reluctance tuning may also be intriguing in variable reluctance motors.

7. Integrate coils into the PMA In order to generate higher magnetic forces, it could be interesting to combine the PMA with coils. This will reduce the energy efficiency of the actuator, but it could make the actuator more appealing to the high-precision industry. It can use the coils for generating high dynamic forces and the reluctance tuning principle for generating low forces without heat dissipation.

8. Explore the concept of distributed actuation. Currently, only one piezoelectric actuator is actuated for simplicity and the central mover was assumed to be the point of most interest. However, the actuator actually consists of three movers that can be displaced at the same time. This opens the possibility of distributed actuation. It is important to highlight that the actuation of one mover influences the behavior of the other movers.

9. Explore the option of active piezo shim actuators. The PMA can sustain a consistent magnetic force without heat dissipation, neglecting current leakage. Nonetheless, to uphold this force consistently, voltage control is necessary. To address this challenge, the piezoelectric actuators could be substituted with active piezo shim actuators. These actuators hold their position stable without permanent control voltage.

10. Investigate the scalability in dimensions of the PMA. Some high-tech industry applications require small actuators with very low heat dissipation and contactless actuation. Therefore it is suggested to explore the performance of the actuator at different dimension scales.

6.3. Actuator potential and applications

While the currently designed PMA may not generate a high force on the central mover in its central position, it combines the strengths of both reluctance actuators and piezoelectric actuators. Reluctance actuators offer the advantage of contactless high magnetic forces but come with high heat dissipation due to the driven coils. On the other hand, piezoelectric actuators have relatively low heat dissipation but suffer from their very stiff mechanical connection with the object that needs to be displaced, resulting in poor disturbance rejection of vibrations. By integrating both types of actuators into a unified design, it becomes possible to create an actuator that by the motion of a piezoelectric actuator can apply a contactless magnetic force on a mover with minimal heat dissipation, thereby earning it the title of the contactless Piezo-Magnetic Actuator. Furthermore, piezoelectric actuators exhibit a high bandwidth, enabling the PMA to be employed at very high frequencies.

Enhancing the frequency response of the designed PMA can be achieved through two approaches: employing extremely stiff flexures or eliminating the flexures connected to the central mover. The utilization of highly rigid flexures leads to the creation of a nanopositioner with improved dynamics, whereas the removal of flexures results in increased magnetic force output, improved dynamics, and longer stroke. Nevertheless, as mentioned before, control is a must in this last configuration to guarantee the stability of the actuator.

Currently, the PMA can be characterized as an energy-efficient short-stroke reluctance actuator. Its minimal heat dissipation makes it particularly suitable for applications in vacuum, space, and cryogenic environments, where high-precision stage positioning or vibration isolation with low heat dissipation is essential. Furthermore, its suitability for electromagnetic microscopes is advantageous, given that the developed actuator does not have the flux leakage from the coils found in traditional electromagnetic actuators, which could otherwise interfere with electron beams. Additionally, there is potential for its utilization as a replacement for piezoelectric actuators in systems that necessitate contactless actuation or a larger displacement range.

A

Actuators using magnetostrictive and piezoelectric material

This appendix provides insight into actuators using magnetostrictive and piezomagnetic material. In addition, it includes the complete derivation of the magnetic force of the hybrid reluctance actuator using cores made of magnetostrictive and piezoelectric material.

A.1. Coilless rotating actuator

Geoffroy et al. introduced a coilless actuator, that uses the magnetostrictive effect to rotate a permanent magnet [44]. The actuator consists of a magnetostrictive disk of soft ferromagnetic material, two lead zirconium titanate (PZT) piezoelectric elements, and a cylindrical magnet. The magnetostrictive disk is glued on the piezoelectric elements. The magnet is placed above the magnetostrictive disk and is free to rotate, see also Figure A.1a. By applying a voltage to a piezoelectric element, the element deforms and generates stress on the magnetostrictive disk. The direction and magnitude of the stress generate a directional magnetic anisotropy in the disk, also called the easy axis. The magnet tends to align itself with the easy axis and therefore generates a torque. To generate a continuous rotation, a second piezoelectric element is used with an angle of $45°$ between the other piezoelectric elements. The combination of compressive and extensive stresses results in a varying rotating uniaxial stress, and therefore a rotating easy axis orientation. The explained principle can also be seen in Figure A.1b [44].

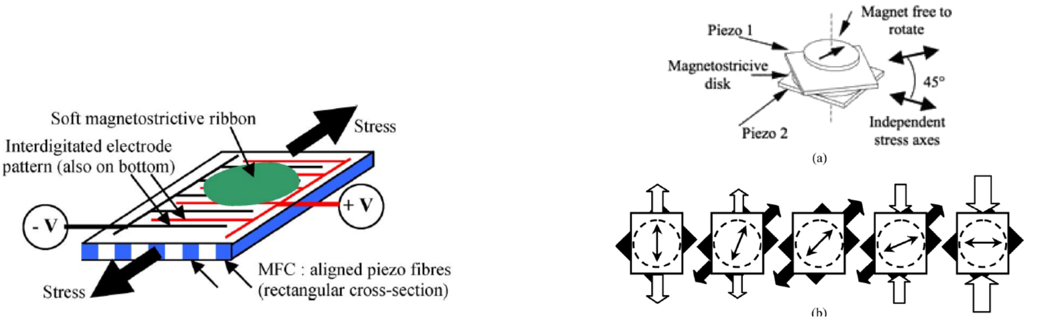

(a) Overview of all components [44]

(b) Sequence principle of the torque generation [44]

Figure A.1: Overview of the coilless rotating actuator

Figure A.2 shows the experimental results retrieved by Geoffroy et al [44]. Figure A.2a shows the measured torque when a certain voltage is applied to the piezoelectric elements. The applied voltage varies between $-600\,\mathrm{V}$ and $1200\,\mathrm{V}$, resulting in a maximum measured torque of $6\,\mu\mathrm{N\,m}$. According to

Geoffroy et, the hysteresis is only due to the piezoelectric elements. Figure A.2b shows the measured torque for a fixed alignment between the magnet and the magnetostrictive disk [44].

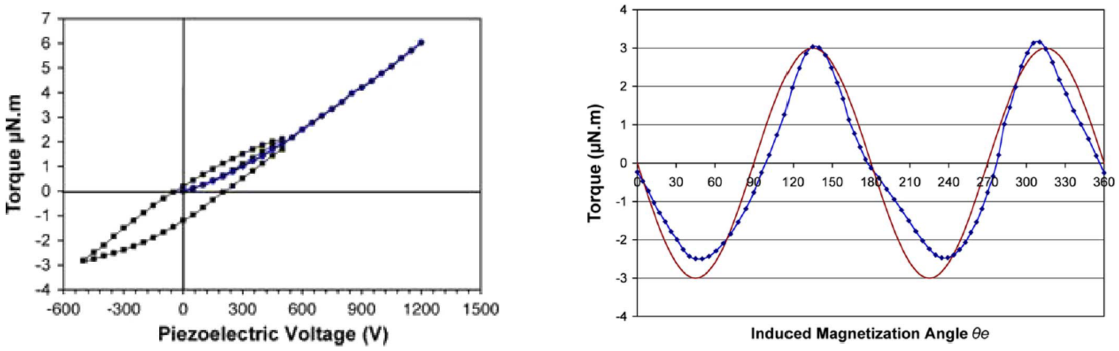

(a) Measured torque on the magnet as a function of the applied voltage [44]

(b) Measured torque on the magnet as a function of the induced magnetization direction [44]

Figure A.2: Experimental results based on the coilless rotating actuator

In this actuator, Joule heating only occurs in the conductive wires due to the transfer of charge needed to deform the piezoelectric elements. After actuation, there is no Joule heating. Eddy currents occur at higher frequencies in the iron-based disk. However, the usage of the piezoelectric elements produces mechanical, dielectric, and piezoelectric losses within the system [44].

A.2. Coilless actuator using a composite core

Ueno et al. introduced a magnetic force control device using a composite core, which is made of giant magnetostrictive material, Terfenol-D, and two stacked piezoelectric actuators [15]. Terfenol-D is characterized by its low permeability, low Young's modulus, and large piezomagnetic coefficient. The magnetic force control device can be seen in Figure A.3. The flux of the permanent magnets flows through two parallel magnetic circuits. One magnetic circuit path consists of the magnets, a soft ferromagnetic mover, and two air gaps. The other path consists of the magnets and the composite core. The composite is initially compressed by two bolts. Pre-stressing reduces the relative permeability of the magnetostrictive material. By applying a voltage on the stacked piezoelectric actuators the material deforms, which reduces the compressive stress on the magnetostrictive material. This process increases the flux in the composite core and decreases the flux in the air gaps, resulting in a decrease of force on the mover [15].

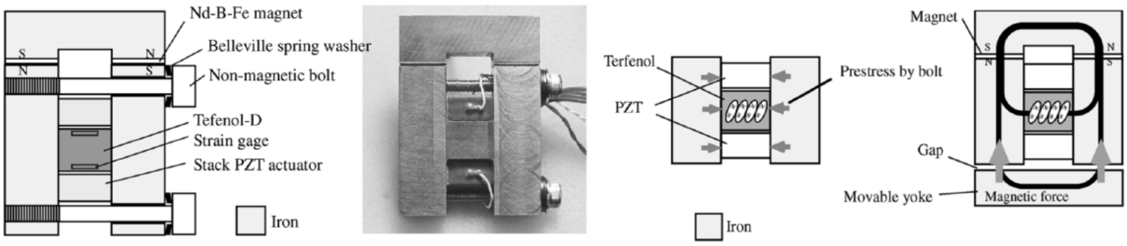

(a) Schematic overview [15]

(b) Working principle [15]

Figure A.3: The magnetic force control device

Figure A.4a shows the measured force as a function of the applied voltage for different pre-stresses and a constant air gap of $0.1\,\mathrm{mm}$. The hysteresis is mainly due to the actuation of the piezoelectric actuators. The maximum force varies from $7\,\mathrm{N}$ for $0\,\mathrm{V}$ to $3.7\,\mathrm{N}$ for $200\,\mathrm{V}$, under a pre-strain of -$240\,\mathrm{ppm}$ due to the bolts. Figure A.4b shows the measured force as a function of the gap size for constant voltage of $0\,\mathrm{V}$ and $200\,\mathrm{V}$, and for different pre-strains [15].

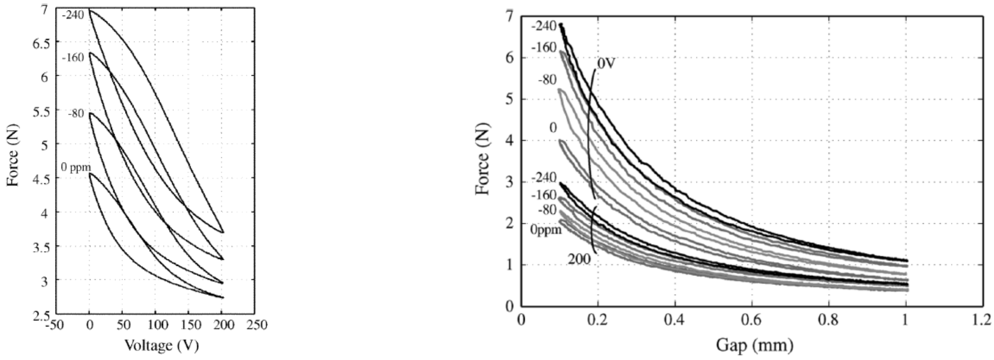

(a) Measured force as a function of the applied voltage for different pre-stresses and a constant air gap of 0, 1mm [15]

(b) The measured force as a function of the gap size for constant voltage of 0V and 200V, and for different pre-strains [15]

Figure A.4: Experimental results based on the magnetic force control device

The composite dissipates zero energy in static operation. There is no Joule heating once the piezoelectric actuators have been charged to change the force. However, during the actuation of the piezoelectric material there is a transfer of charge. This generates Joule heating. Also, the actuation of the piezoelectric material generates mechanical, dielectric, and piezoelectric losses. Based on the magnetic force control device, a linear step motor has been developed, which achieved step motion of the mover while having zero power consumption and zero heat generation in static operation [15].

A.3. Multilayer composite core

There are electrical devices that make use of a composite core, made of multiple layers of PZT/Metglas units. Such a unit consists of two layers of Metglas placed on each side of a PZT sheet as seen in Figure A.5. By applying a voltage on the electrodes of a PZT sheet, the PZT sheet will deform due to the piezoelectric effect. The deformation of the PZT sheet generates mechanical stress on the Metglas layers, this changes the relative permeability of the Metglas layers due to the magnetoelectric effect [45]. The multilayer composite is also called a magnetic flux value (MFV).

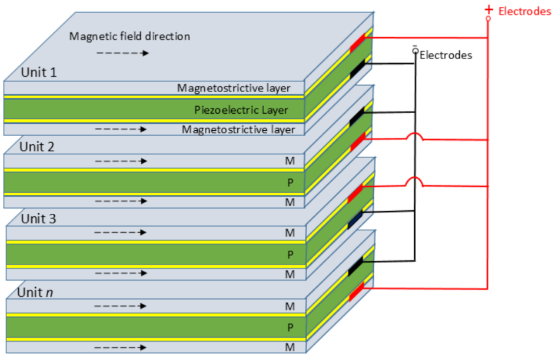

Figure A.5: Overview of a core made of multiple layers of PZT/Metglas units [46]

The multilayer composite core can be found in electrical devices, such as an adjustable-voltage-ratio (AVR) transformer [47][45], a three-phase (AVR) transformer [46], and a tunable inductor [48], see also Figure A.6. However, it seems not yet to be applied in a reluctance actuator.

The relative permeability of a Metglas layer as a function of the applied voltage on the PZT sheet is as follows [46][45]:

$$\mu_r = \frac{M_s}{H_{org} + \frac{3\lambda_s}{M_s} \times \frac{d_{31}U}{s_{31}d}} \tag{A.1}$$

where M_s is the saturation magnetization of the Metglas, H_{org} is the original magnetic anisotropy field of the Meglass when no external voltage is applied, λ_s is the saturation magnetostriction constant, d_{31}

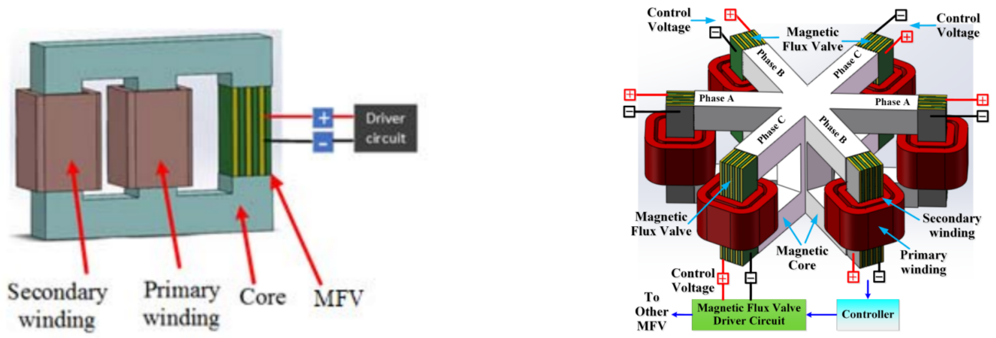

(a) A single-phase transformer based on MFV [45]

(b) A three-phase transformer based on MFV [46]

Figure A.6: Devices based on PZT/Metglas composite core

is the piezoelectric strain coefficient of the PZT sheet, s_{31} is the elasticity coefficient of the PZT sheet, d is the thickness of the PZT sheet, and U the applied voltage.

According to Equation A.1, the permeability of a Metglas layer decreases as the applied voltage increases. This has been validated in an experiment performed by Cui et al, based on a composite core made of 80 PZT/Metglas units [45]. The results can be seen in Figure A.7, which showed that the relative permeability can be adjusted to a range from 680 to 134 when varying the voltage from 0V to 300V [48]. The total reluctance of a composite core can be calculated as [45]:

$$\mathcal{R}_x = \frac{l}{\mu_0 \mu_x A} \tag{A.2}$$

where l is the length of the core, μ_0 is the permeability of air or vacuum, μ_x is the permeability of the magnetostrictive material in the core, A is the effective cross-section area of the composite core. According to this equation, a voltage applied on the PZT layer decreases the reluctance of the core.

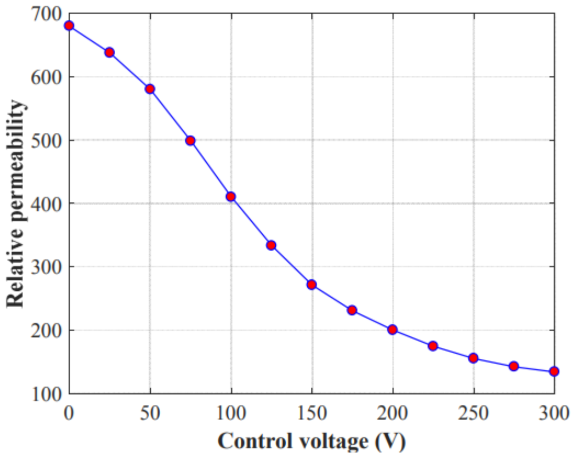

Figure A.7: Measured relative permeability by varying the applied voltage on the PZT sheets [45]

A.4. Analytical model HRA with magnetrostrictive cores

It is investigated if the integration of a composite core made of magnetostrictive and piezomagnetic material is interesting to apply in the design of a Hybrid Reluctance Actuator as depicted in Figure A.8a. To assess the magnetic force generated by the actuator, an analytical model of the magnetic circuit is developed as seen in Figure A.8b. In this model, it is assumed that the relative magnetic permeability of the soft ferromagnetic components is sufficiently large, such that the reluctance of the stator and mover can be ignored. Non-linear effects such as magnetic hysteresis and fringing flux are also neglected. In addition, the relative permeability of the magnet is assumed to be one.

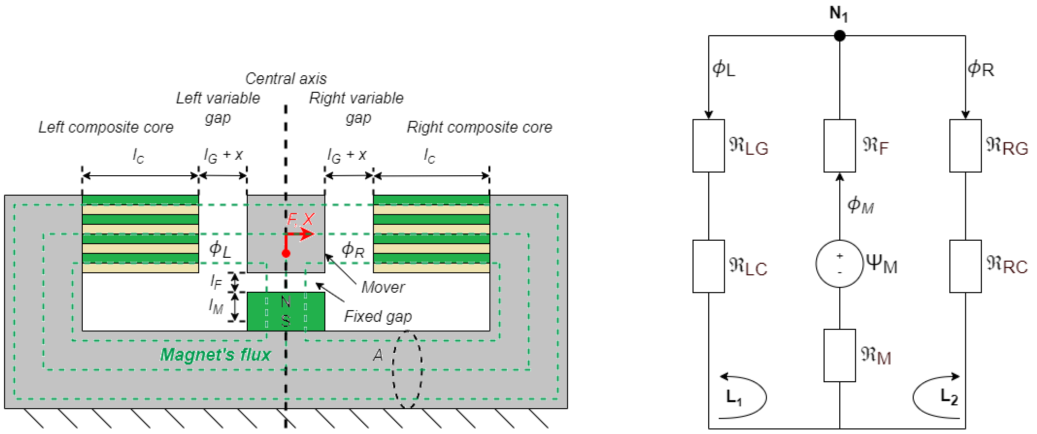

(a) Overview of the Hybrid Reluctancea Actuator and the two integrated composite cores

(b) Analytical model of the magnetic circuit of the Hybrid Reluctance Actuator with two composite cores

Figure A.8: Overview and analytical model of an Hybrid Reluctance Actuator and two integrated composite cores

The reluctance of the left air gap $\Re_{LG}$, right air gap $\Re_{RG}$, fixed air gap $\Re_F$, left composite core $\Re_{LC}$, right composite core $\Re_{RC}$, and permanent magnet $\Re_M$ are modeled as [6][3][4][45]:

$$\Re_{LG} = \frac{x_G + x}{A\mu_0}, \Re_{RG} = \frac{x_G - x}{A\mu_0}, \Re_{LC} = \frac{l_C}{A\mu_0\mu_x}, \Re_{RC} = \frac{l_C}{A\mu_0\mu_x}, \Re_F = \frac{l_F}{A\mu_0}, \Re_M = \frac{l_M}{A\mu_0} \tag{A.3}$$

where x is the variable position of the mover relative to its center position and x_G is the size of the left and right air gaps when the mover is in its center position. A, μ_0, μ_x, l_F, l_C, and l_M are the cross-section area of all components, the permeability of air or vacuum, the permeability of the composite core, the fixed air gap length, the length of the composite core, and the permanent magnet length, respectively. The magnetomotive force (MMF) of the permanent magnet Ψ_m and of one coil Ψ_c are given by [23]:

$$\Psi_M = -H_c l_M \lambda, \Psi_C = NI \tag{A.4}$$

where H_c is the coercivity field strength, l_M is the length of the permanent magnet, λ is the flux leakage factor of the permanent magnet, N is the amount of windings and I is the current in the coils.

By utilizing Hopkinson's law of magnetics, the magnetic flux of the permanent magnet ϕ_m is determined as [6][23]:

$$\phi_M = \frac{-H_c l_M \lambda}{\Re_F + \Re_M + \Re_P} \tag{A.5}$$

where $\Re_P$ is the total reluctance of the left and right air gap connected in parallel. By using Kirchhoff's circuit laws for magnetic circuits, the network equations in the closed loops and node are:

$$N_1 : \phi_M - \phi_L - \phi_R = 0 \tag{A.6}$$

$$L_1 : \phi_M(\Re_M + \Re_F) + \phi_L(\Re_{LG} + \Re_{LC}) = \Psi_M + \Psi_{LC} \tag{A.7}$$

$$L_2 : \phi_M(\Re_M + \Re_F) + \phi_R(\Re_{RG} + \Re_{RC}) = \Psi_M - \Psi_{RC} \tag{A.8}$$

Solving these equations gives the magnetic flux in the variable air gaps. The magnetic force on the mover for a single DoF in the direction of x is calculated by using the Maxwell stress tensor:

$$F_{COMPO} = \frac{(\phi_L)^2 - (\phi_R)^2}{2\mu_0 A} \tag{A.9}$$

A.4.1. Magnetic force analysis

Figure A.9 plots the derived magnetic force for increasing relative permeability of the left composite core μ_x in the range 184 to 680. The position of the mover is kept at $x = 0$. The length of the composite cores is set to $18.1\,\mathrm{mm}$ [47]. The relative permeability of the right composite core is set static to 680. The used values for the design parameters of the actuator are presented in Appendix E. Figure A.9 shows that the magnetic force on the mover reaches a maximum of $2.38\,\mathrm{N}$.

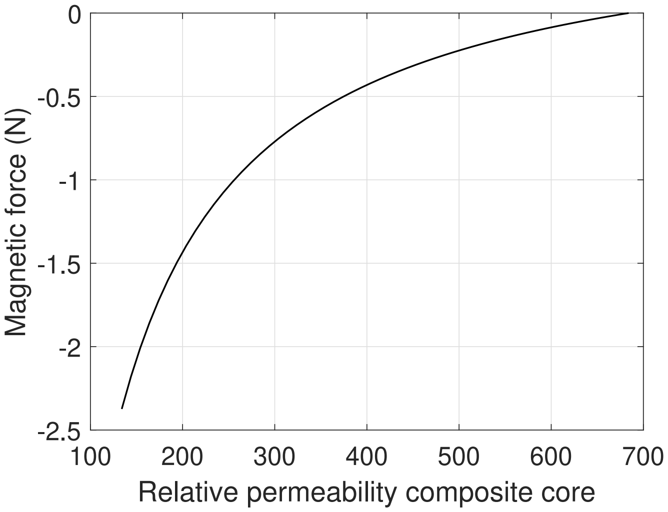

Figure A.9: Evaluation of the analytical model for increasing relative permeability of the left composite core, while keeping the position of the mover at $x = 0$

B

Analytical model Hybrid Reluctance Actuator

This appendix includes the complete derivation of the magnetic force of the HRA.

To assess the magnetic force generated by the HRA, an analytical model of the magnetic circuit is developed as seen in Figure B.1. In this model, it is assumed that the relative magnetic permeability of the ferromagnetic components is sufficiently large, such that the reluctance of the stator and mover can be ignored. Non-linear effects such as magnetic hysteresis and fringing flux are also neglected. In addition, the relative permeability of the magnet is assumed to be one.

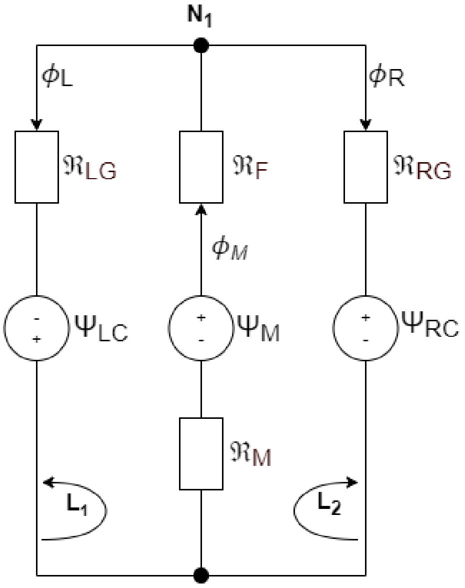

Figure B.1: Analytical model of the magnetic circuit of an HRA

The reluctance of the left air gap $\mathfrak{R}_{LG}$, the right air gap $\mathfrak{R}_{RG}$, the fixed air gap $\mathfrak{R}_F$, and the permanent magnet $\mathfrak{R}_M$ are modeled as [6][3][4]:

$$\mathfrak{R}_{LG} = \frac{x_G - x}{A\mu_0}, \mathfrak{R}_{RG} = \frac{x_G + x}{A\mu_0}, \mathfrak{R}_F = \frac{l_F}{A\mu_0}, \mathfrak{R}_M = \frac{l_M}{A\mu_0} \tag{B.1}$$

where x is the variable position of the mover relative to its center position and x_G is the size of the left and right air gaps when the mover is in its center position. A, μ_0, l_F, and l_M are the cross-section area of all components, the permeability of air, the fixed air gap length, and the permanent magnet length, respectively. The magnetomotive force (MMF) of the permanent magnet Ψ_m and of one coil Ψ_c are given by [23]:

$$\Psi_M = -H_c l_M \lambda, \Psi_C = NI \tag{B.2}$$

where H_c is the coercivity field strength, l_M is the length of the permanent magnet, λ is the flux leakage factor of the permanent magnet, N is the amount of windings and I is the current in the coils.

By utilizing Hopkinson's law of magnetics, the magnetic flux of the permanent magnet ϕ_m is determined as [6][23]:

$$\phi_M = \frac{-H_c l_M \lambda}{\Re_F + \Re_M + \Re_P} \tag{B.3}$$

where $\Re_P$ is the total reluctance of the left and right air gap connected in parallel. By using Kirchhoff's circuit laws for magnetic circuits, the network equations in the closed loops and node are:

$$N_1 : \phi_M - \phi_L - \phi_R = 0 \tag{B.4}$$

$$L_1 : \phi_M(\Re_M + \Re_F) + \phi_L \Re_{LG} = \Psi_M + \Psi_{LC} \tag{B.5}$$

$$L_2 : \phi_M(\Re_M + \Re_F) + \phi_R \Re_{RG} = \Psi_M - \Psi_{RC} \tag{B.6}$$

Solving these equations gives the magnetic flux in the variable air gaps. The magnetic force on the central mover for a single DoF in the direction of x is calculated by using the Maxwell stress tensor. In the case of a current-controlled Hybrid Reluctance Actuator, the force equation can be written to an expression that depends on the applied current I and the position x of the mover [3][4][24]:

$$F_{HRA} = \frac{(\phi_L)^2 - (\phi_R)^2}{2\mu_0 A} = K_M I + k_a x \tag{B.7}$$

where K_M is the motor constant and k_a is the actuator stiffness, given by [3]:

$$K_M = \frac{2H_c l_M \lambda A \mu_0 N I}{2x_G l_M + 2x_G l_F + x_G^2 - x^2}, k_a = \frac{2H_c^2 l_M^2 \lambda^2 A \mu_0 x_G}{(2x_G l_M + 2x_G l_F + x_G^2 - x^2)^2} \tag{B.8}$$

C

Reluctance tuning parameters

This appendix presents a table that contains the parameter values employed in the evaluation of reluctance tuning principles.

Table C.1: Parameter values for comparison reluctance principles

Denotation	Value	Comments
L_{G1}	$1\,\mathrm{mm}$	Length air gap 1
W	$20\,\mathrm{mm}$	Width of air gaps
H	$20\,\mathrm{mm}$	Height of air gaps
A	$400\,\mathrm{mm}^2$	Cross-section of air gaps
A_R	$160\,\mathrm{mm}^2$	Reduction surface area of stator
μ_0	$4\pi\times10^{-7}\,\mathrm{H/m}$	Relative permeability of air or vacuum

D

Analytical model Piezo-Magnetic Actuator

This appendix includes the complete derivation of the magnetic force of the PMA.

D.1. Network equations

To assess the magnetic force generated by the PMA, an analytical model of the magnetic circuit is developed as seen in Figure D.1. In this model, it is assumed that the relative permeability of the ferromagnetic components is sufficiently large, such that the reluctance of the stator and movers can be ignored. The direct magnetic flux path from the magnet into the surrounding air is ignored. Non-linear effects such as magnetic hysteresis, fringing flux, and saturation are also neglected. Consequently, the derived model is only valid for flux densities smaller than the saturation flux density of the stator. In addition, the relative permeability of the magnet is assumed to be one. Due to the low relative magnetic permeability of piezoelectric actuators, it is assumed that no magnetic flux passes through the piezoelectric actuators.

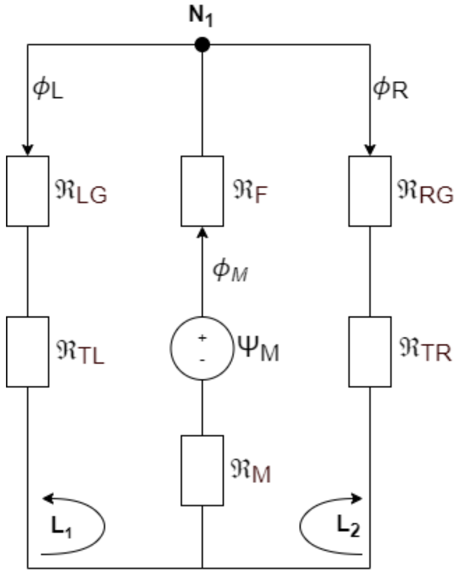

Figure D.1: Analytical model of the magnetic circuit of PMA

The reluctance of the left variable air gap $\mathfrak{R}_{LG}$, the right variable air gap $\mathfrak{R}_{RG}$, the left tunable air gap

$\Re_{TL}$, the right tunable air gap $\Re_{TR}$, the fixed air gap $\Re_F$, and the permanent magnet $\Re_M$ are modeled as:

$$\Re_{LG} = \frac{l_G + x - x_{TL}}{A\mu_0}, \Re_{RG} = \frac{l_G - x - x_{TR}}{A\mu_0}, \Re_{TL} = \frac{x_{TL}}{A_T\mu_0}, \Re_{TR} = \frac{x_{TR}}{A_T\mu_0}, \Re_F = \frac{l_F}{A\mu_0}, \Re_M = \frac{l_M}{A\mu_0} \quad \text{(D.1)}$$

where x is the variable position of the central mover relative to its center position, x_{TL} is the displacement of the left tunable mover, x_{TR} is the displacement of the right tunable mover, A is the surface area of all the components except for the tunable air gaps A_T, μ_0 is the permeability of air or vacuum, l_G is the length of the left and right variable air gap when the central mover is in its center position ($x = 0$) and both tunable movers are positioned against the stator ($x_{TL} = 0$ and $x_{TR} = 0$), l_{PR} is the initial length of tunable air gap needed for pre-loading the piezoelectric actuators, l_F is the fixed air gap length, and l_M is the permanent magnet length. By assuming a linear second quadrant BH-curve of the permanent magnet, the magnetomotive force of the permanent magnet Ψ_m is given by [23]:

$$\Psi_M = -H_c l_M \lambda \quad \text{(D.2)}$$

where H_c is the coercivity field strength, l_M is the length of the permanent magnet, λ is the flux leakage factor of the permanent magnet.

By utilizing Hopkinson's law of magnetics, the magnetic flux of the permanent magnet ϕ_m is determined as [6][23]:

$$\phi_M = \frac{-H_c l_M \lambda}{\Re_F + \Re_M + \Re_P} \quad \text{(D.3)}$$

where $\Re_P$ is the total reluctance of the left variable and tunable air gap and the right variable and tunable air gap connected in parallel. By using Kirchhoff's circuit laws for magnetic circuits, the network equations in the closed loops and node are:

$$N_1 : \phi_M - \phi_L - \phi_R = 0 \quad \text{(D.4)}$$

$$L_1 : \phi_M(\Re_M + \Re_F) + \phi_L(\Re_{LG} + \Re_{TL}) = \Psi_M \quad \text{(D.5)}$$

$$L_2 : \phi_M(\Re_M + \Re_F) + \phi_R(\Re_{RG} + \Re_{TR}) = \Psi_M \quad \text{(D.6)}$$

Solving these equations gives the magnetic flux in the variable air gaps next to the central mover.

D.2. Magnetic flux in variable right air gap

The following steps are taken to derive the magnetic flux in the variable right air gap. Divide Equation D.5 by Equation D.5:

$$\frac{\phi_L\,(\Re_{LG} + \Re_{TL})}{\phi_R\,(\Re_{RG} + \Re_{TR})} = \frac{-\left(\Re_f + \Re_M\right) + \Psi_M}{-\left(\Re_f + \Re_M\right) + \Psi_M} = 1 \quad \text{(D.7)}$$

Simplify to:

$$\phi_L\,(\Re_{LG} + \Re_{TL}) = \phi_R\,(\Re_{RG} + \Re_{TR}) \Rightarrow \phi_L = \phi_R \frac{\Re_{RG} + \Re_{TR}}{\Re_{LG} + \Re_{TL}} \quad \text{(D.8)}$$

Use Equation D.4 and substitute into Equation D.8 gives:

$$\phi_M - \phi_R = \phi_R \frac{\Re_{RG} + \Re_{TR}}{\Re_{LG} + \Re_{TL}} \quad \text{(D.9)}$$

Simplify to:

$$\phi_M = \phi_R \left(1 + \frac{\Re_{RG} + \Re_{TR}}{\Re_{LG} + \Re_{TL}}\right) \quad \text{(D.10)}$$

and rewrite to:

$$\phi_R = \phi_M \left(\frac{\Re_{LG} + \Re_{TL}}{\Re_{LG} + \Re_{TL} + \Re_{RG} + \Re_{TR}}\right) \quad \text{(D.11)}$$

The reluctance terms in the brackets can be simplified to:

$$\frac{\mathfrak{R}_{LG} + \mathfrak{R}_{TL}}{\mathfrak{R}_{LG} + \mathfrak{R}_{TL} + \mathfrak{R}_{RG} + \mathfrak{R}_{TR}} = \frac{l_G + x + x_{TL}(\frac{A}{A_T} - 1)}{2l_G + x_{TL}(\frac{A}{A_T} - 1) + x_{TR}(\frac{A}{A_T} - 1)} \tag{D.12}$$

Substituting Equation D.12 into Equation D.11 gives:

$$\phi_R = \phi_{pm}\left(\frac{x_g + x + x_{TL}(\frac{A}{A_T} - 1)}{2x_g + x_{TL}(\frac{A}{A_T} - 1) + x_{TR}(\frac{A}{A_T} - 1)}\right) \tag{D.13}$$

The found equation can be split into the following terms:

$$\phi_R = \phi_G + \phi_X + \phi_{TL} \tag{D.14}$$

where

$$\phi_G = \phi_M\left(\frac{l_G}{2l_G + x_{TL}(\frac{A}{A_T} - 1) + x_{TR}(\frac{A}{A_T} - 1)}\right) \tag{D.15}$$

$$\phi_X = \phi_M\left(\frac{x}{2l_G + x_{TL}(\frac{A}{A_T} - 1) + x_{TR}(\frac{A}{A_T} - 1)}\right) \tag{D.16}$$

$$\phi_{TL} = \phi_M\left(\frac{(\frac{A}{A_T} - 1)(x_{TL}}{2l_G + x_{TL}(\frac{A}{A_T} - 1) + x_{TR}(\frac{A}{A_T} - 1)}\right) \tag{D.17}$$

D.3. Magnetic flux in variable left air gap

The same steps earlier can be used to derive an expression for ϕ_L:

$$\phi_L = \phi_M\left(\frac{\mathfrak{R}_{RG} + \mathfrak{R}_{TR}}{\mathfrak{R}_{LG} + \mathfrak{R}_{TL} + \mathfrak{R}_{RG} + \mathfrak{R}_{TR}}\right) \tag{D.18}$$

and by simplifying the reluctance terms, Equation D.18 can be rewritten to:

$$\phi_L = \phi_M\left(\frac{l_G - x + x_{TR}(\frac{A}{A_T} - 1)}{2l_G + x_{TL}(\frac{A}{A_T} - 1) + x_{TR}(\frac{A}{A_T} - 1)}\right) \tag{D.19}$$

The found equation can be split into the following terms:

$$\phi_L = \phi_G - \phi_X + \phi_{TR} \tag{D.20}$$

D.4. Total reluctance of all gaps

$\mathfrak{R}_P$ is the total reluctance of all air gaps connected in parallel and is calculated as:

$$\frac{1}{\mathfrak{R}_P} = \frac{1}{\mathfrak{R}_{LG} + \mathfrak{R}_{TL}} + \frac{1}{\mathfrak{R}_{RG} + \mathfrak{R}_{TR}} \tag{D.21}$$

and can be rewritten to:

$$\mathfrak{R}_P = \frac{(\mathfrak{R}_{GL} + \mathfrak{R}_{TL})\,(\mathfrak{R}_{RG} + \mathfrak{R}_{TR})}{\mathfrak{R}_{LG} + \mathfrak{R}_{TL} + \mathfrak{R}_{RG} + \mathfrak{R}_{TR}} = \frac{\left(l_G + x + x_{TL}(\frac{A}{A_T} - 1)\right)\left(l_G - x + x_{TR}(\frac{A}{A_T} - 1)\right)}{A\mu_0\left(2l_G + x_{TL}(\frac{A}{A_T} - 1) + x_{TR}(\frac{A}{A_T} - 1)\right)} \tag{D.22}$$

D.5. Simplified magnetic flux equation

By utilizing Hopkinson’s law of magnetics, the magnetic flux of the permanent magnet ϕ_m is determined as [6][23]:

$$\phi_M = \frac{-H_c l_M \lambda}{\Re_F + \Re_M + \Re_P} \tag{D.23}$$

This equation can be rewritten by using Equation D.23 to:

$$\phi_M = \frac{-H_c l_M \lambda}{\frac{l_M}{A\mu_0} + \frac{l_F}{A\mu_0} + \frac{\left(l_G+x+x_{TL}(\frac{A}{A_T}-1)\right)\left(l_G-x+x_{TR}(\frac{A}{A_T}-1)\right)}{A\mu_0\left(2l_G+x_{TL}(\frac{A}{A_T}-1)+x_{TR}(\frac{A}{A_T}-1)\right)}} \tag{D.24}$$

and simplified to:

$$\phi_M = \frac{-H_c l_M \lambda A\mu_0\left(2l_G+x_{TL}(\frac{A}{A_T}-1)+x_{TR}(\frac{A}{A_T}-1)\right)}{\left(2l_G+x_{TL}(\frac{A}{A_T}-1)+x_{TR}(\frac{A}{A_T}-1)\right)(l_M+l_F)+\left(l_G+x+x_{TL}(\frac{A}{A_T}-1)\right)\left(l_G-x+x_{TR}(\frac{A}{A_T}-1)\right)} \tag{D.25}$$

D.6. The magnetic force

The magnetic force on the central mover for a single DoF in the direction of x is calculated by using the Maxwell stress tensor:

$$F = \frac{-(-\phi_L)^2 + (\phi_R)^2}{2\mu_0 A} \tag{D.26}$$

$$(-\phi_L)^2 = \phi_G^2 - 2\phi_X\phi_G + \phi_X^2 + 2\phi_G\phi_{TR} + \phi_{TR}^2 - 2\phi_X\phi_{TR} \tag{D.27}$$

$$\phi_R^2 = \phi_G^2 + 2\phi_X\phi_G + \phi_X^2 + 2\phi_G\phi_{TL} + \phi_{TL}^2 + 2\phi_X\phi_{TL} \tag{D.28}$$

Thus:

$$F = \frac{-\phi_G^2+2\phi_X\phi_G-\phi_X^2-2\phi_G\phi_{TR}-\phi_{TR}^2+2\phi_X\phi_{TR}+\phi_G^2+2\phi_X\phi_G+\phi_X^2+2\phi_G\phi_{TL}+\phi_{TL}^2+2\phi_X\phi_{TL}}{2A\mu_0} \tag{D.29}$$

This can be simplified to:

$$F = \frac{4\phi_X\phi_G - 2\phi_G\phi_{TR} - \phi_{TR}^2 + 2\phi_X\phi_{TR} + 2\phi_G\phi_{TL} + \phi_{TL}^2 + 2\phi_X\phi_{TL}}{2A\mu_0} \tag{D.30}$$

D.7. Magnetic force terms

The magnetic force expression of Equation D.30 can be split into seven terms:

$$\frac{4\phi_X\phi_G}{2A\mu_0} = \left(\frac{2H_c^2 l_M^2 \lambda^2 A\mu_0 l_G}{\left(\left(2l_G+x_{TL}(\frac{A}{A_T}-1)+x_{TR}(\frac{A}{A_T}-1)\right)(l_M+l_F)+\left(l_G+x+x_{TL}(\frac{A}{A_T}-1)\right)\left(l_G-x+x_{TR}(\frac{A}{A_T}-1)\right)\right)^2}\right)x \tag{D.31}$$

$$-\frac{2\phi_G\phi_{TR}}{2A\mu_0} = \left(\frac{-H_c^2 l_M^2 \lambda^2 A\mu_0 l_G(\frac{A}{A_T}-1)}{\left(\left(2l_G+x_{TL}(\frac{A}{A_T}-1)+x_{TR}(\frac{A}{A_T}-1)\right)(l_M+l_F)+\left(l_G+x+x_{TL}(\frac{A}{A_T}-1)\right)\left(l_G-x+x_{TR}(\frac{A}{A_T}-1)\right)\right)^2}\right)x_{TR,R} \tag{D.32}$$

$$\frac{-\phi_{TR}^2}{2A\mu_0} = \left(\frac{-H_c^2 l_M^2 \lambda^2 A\mu_0\left(\frac{A}{A_T}-1\right)^2}{\left(\left(2l_G+x_{TL}(\frac{A}{A_T}-1)+x_{TR}(\frac{A}{A_T}-1)\right)(l_M+l_F)+\left(l_G+x+x_{TL}(\frac{A}{A_T}-1)\right)\left(l_G-x+x_{TR}(\frac{A}{A_T}-1)\right)\right)^2}\right)\frac{x_{TR}^2}{2} \tag{D.33}$$

$$\frac{2\phi_X\phi_{TR}}{2A\mu_0} = \left(\frac{H_c^2 l_{pm}^2 \lambda^2 A\mu_0(\frac{A}{A_T}-1)}{\left(\left(2l_G+x_{TL}(\frac{A}{A_T}-1)+x_{TR}(\frac{A}{A_T}-1)\right)(l_M+l_F)+\left(l_G+x+x_{TL}(\frac{A}{A_T}-1)\right)\left(l_G-x+x_{TR}(\frac{A}{A_T}-1)\right)\right)^2}\right)x_{TR}x \tag{D.34}$$

$$\frac{2\phi_G\phi_{TL}}{2A\mu_0}=\left(\frac{H_C^2 l_M^2\lambda^2 A\mu_0 l_G(\frac{A}{A_T}-1)}{\left(\left(2l_G+x_{TL}(\frac{A}{A_T}-1)+x_{TR}(\frac{A}{A_T}-1)\right)(l_M+l_F)+\left(l_G+x+x_{TL}(\frac{A}{A_T}-1)\right)\left(l_G-x+x_{TR}(\frac{A}{A_T}-1)\right)\right)^2}\right)x_{TL} \tag{D.35}$$

$$\frac{\phi_{TL}^2}{2A\mu_0}=\left(\frac{H_C^2 l_M^2\lambda^2 A\mu_0\left(\frac{A}{A_T}-1\right)^2}{\left(\left(2l_G+x_{TL}(\frac{A}{A_T}-1)+x_{TR}(\frac{A}{A_T}-1)\right)(l_M+l_F)+\left(l_G+x+x_{TL}(\frac{A}{A_T}-1)\right)\left(l_G-x+x_{TR}(\frac{A}{A_T}-1)\right)\right)^2}\right)\frac{x_{TL}^2}{2} \tag{D.36}$$

$$\frac{2\phi_X\phi_{TL}}{2A\mu_0}=\left(\frac{H_C^2 l_M^2\lambda^2 A\mu_0(\frac{A}{A_T}-1)}{\left(\left(2l_G+x_{TL}(\frac{A}{A_T}-1)+x_{TR}(\frac{A}{A_T}-1)\right)(l_M+l_F)+\left(l_G+x+x_{TL}(\frac{A}{A_T}-1)\right)\left(l_G-x+x_{TR}(\frac{A}{A_T}-1)\right)\right)^2}\right)x_{TL}x \tag{D.37}$$

When looking at the seven terms, two similar terms can be identified:

$$K_{PZ}=\left(\frac{H_C^2 l_M^2\lambda^2 A\mu_0 l_G(\frac{A}{A_T}-1)}{\left(\left(2l_G+(\frac{A}{A_T}-1)x_{TL}+(\frac{A}{A_T}-1)x_{TR}\right)\left(l_M+l_F\right)+\left(l_G+x+(\frac{A}{A_T}-1)x_{TL}\right)\left(l_G-x+(\frac{A}{A_T}-1)x_{TR}\right)\right)^2}\right) \tag{D.38}$$

$$k_a=\left(\frac{2H_C^2 l_M^2\lambda^2 A\mu_0 l_G}{\left(\left(2l_G+(\frac{A}{A_T}-1)x_{TL}+(\frac{A}{A_T}-1)x_{TR}\right)\left(l_M+l_F\right)+\left(l_G+x+(\frac{A}{A_T}-1)x_{TL}\right)\left(l_G-x+(\frac{A}{A_T}-1)x_{TR}\right)\right)^2}\right) \tag{D.39}$$

Thus, the magnetic force can be rewritten to:

$$F=K_{PM}\left(x_{TL}-x_{TR}+\frac{\frac{A}{A_T}-1}{2l_G}\left(x_{TL}^2-x_{TR}^2\right)+\frac{x\left(x_{TL}+x_{TR}\right)}{l_G}\right)+k_a x \tag{D.40}$$

where K_{PM} is the piezo-magnetic coefficient and k_a is the actuator stiffness.

E

Actuator design parameters

This appendix provides an overview of the design parameter values utilized in all conducted analyses and in the development of the experimental setup.

An iterative design approach is employed to derive the design parameters for the magnetic circuit of the developed PMA. The design approach commences by selecting an available flat magnet with high coercivity and choosing standard steel for both the stator and movers. The dimensions and cross-sections of the air gaps are carefully chosen to limit the magnetic flux density in the stator with the reduced surface area to $1.5\,\mathrm{T}$ and to ensure manufacturability. Eventually, a standard 150V piezo stack actuator is chosen to fit within the stator of the actuator. The design resulted in the magnetic circuit parameters in Table E.1. It is important to highlight that the parameter design values in Table E.1 are not optimized. The flux leakage factor and fringing flux effect are investigated in the 3D FEA model, see Appendix H. This Appendix shows that the cross-section of the fixed air gap A_F and the tunable air gaps A_T are larger than their mechanical geometries. For this reason, these cross-sections are corrected to $A_{F,eff}$ = $530\,\mathrm{mm}^2$ and $A_{T,eff}$ = $212\,\mathrm{mm}^2$. These effective cross-sections and not the mechanical geometries are applied in all the conducted analyses.

Table E.1: PMA design parameters

Denotation	Value	Comments
Stator and Movers		
A	$400\,\mathrm{mm}^2$	Surface area
μ_r	1100	Relative permeability of S235JRC+C(SH) [49]
B_{sat}	$1.5\,\mathrm{T}$	Magnetic saturation of S235JRC+C(SH) [49]
Air Gaps		
A_F / $A_{F,eff}$	$400\,\mathrm{mm}^2$ / $530\,\mathrm{mm}^2$ (Appendix H)	Cross-section of the fixed air gaps
A_T / $A_{T,eff}$	$160\,\mathrm{mm}^2$ / $212\,\mathrm{mm}^2$ (Appendix H)	Cross-section of tunable air gaps
A_G	$400\,\mathrm{mm}^2$	Cross-section of variable air gaps
l_F	$2\,\mathrm{mm}$	Fixed air gap length
l_{PR}	$0.2\,\mathrm{mm}$	Initial tunable air gap length needed for pre-loading
l_G	$1\,\mathrm{mm}$	Variable air gap length
N42 Magnet		
A_M	$400\,\mathrm{mm}^2$	Surface area
l_M	$5\,\mathrm{mm}$	Magnet length
μ_r	1.05	Relative permeability [50]
B_r	$1.305\,\mathrm{T}$	(Average) remanent flux density [35]
λ	0.64 (Appendix H)	(Average) flux leakage factor

F

Settings FEA model

The created 3D model in COMSOL Multiphysics® is based on a stationary study using the physics domain magnetic fields. The geometry of the model is depicted in Figure F.1. The used dimensions for the geometry can be found in Table E.1. The actuator is positioned within a sizable air box of $300\,\mu\mathrm{m} \times 300\,\mu\mathrm{m} \times 300\,\mu\mathrm{m}$ to effectively model flux leakage and fringing flux. Small curved boundaries are avoided in the model, unless they are important for the result, to reduce local peaks and singularity. In addition, it avoids the creating of inverted mesh elements causing convergence problems.

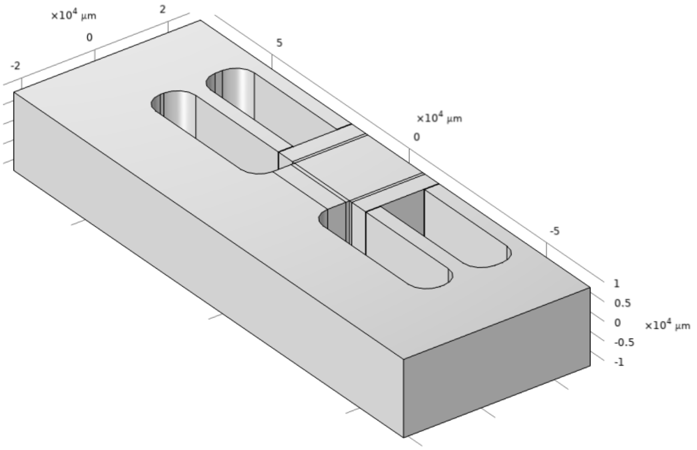

Figure F.1: 3D model with dimensions

The soft ferromagnetic components are modeled by unlaminated S235JRC+C(SH) [34] and the permanent magnet is modeled as a sintered NdFeB N42 [35]. The required properties of the materials utilized in the model can be located in Table F.1.

Table F.1: Material Properties

Denotation	Value
S235JRC+C(SH) Steel	
Relative permeability	1100
Electrical conductivity	$1\,\mathrm{S/m}$
Relative permittivity	1
Sintered NdFeB N42 Magnet	
Electrical conductivity	$1\,\mathrm{S/m}$
Recoil permeability	1.05
Remanent flux density norm	$1.305\,\mathrm{T}$
Air	
Relative permeability	1
Electrical conductivity	$0\,\mathrm{S/m}$
Relative permittivity	1

The discretization used for the magnetic field physics interface is second order Lagrange. The chosen constitutive relation for the soft ferromagnetic components is based on the relative permeability:

$$B = \mu_0 \mu_r H \tag{F.1}$$

The chosen constitutive relation for the permanent magnet is based on the remanent flux density:

$$B = \mu_0 \mu_{rec} H + B_r, B_r = ||B_r|| \frac{e}{||e||} \tag{F.2}$$

where e is the direction of magnetization. The built-in force calculate node in COMSOL is used to determine the magnetic force on the central mover. This feature uses the Maxwell stress tensor over the exterior surfaces of the set of domains to compute forces and torques [33].

In each simulation, local adaptive mesh refinement is employed to validate the model's accuracy. COMSOL initially computes the solution on an initial mesh and evaluates the error only over some subset of the entire model. The geometry of selected components in the model is then re-meshed with finer elements specifically in the regions where the error is significant. The model resolves on this new mesh. Mesh refinements continue until the model results exhibit less than a 1% variation compared to the previous mesh. When this criterion is met in two successive refinements, convergence is achieved. The initial mesh utilizes COMSOL's built-in physics-controlled mesh set to a finer resolution, leveraging the software's ability to automatically generate a mesh based on the underlying physics of the simulation. In this FEA model, local adaptive mesh refinement is applied to the mesh of the movers, air gaps, and the permanent magnet as depicted in Figure F.2.

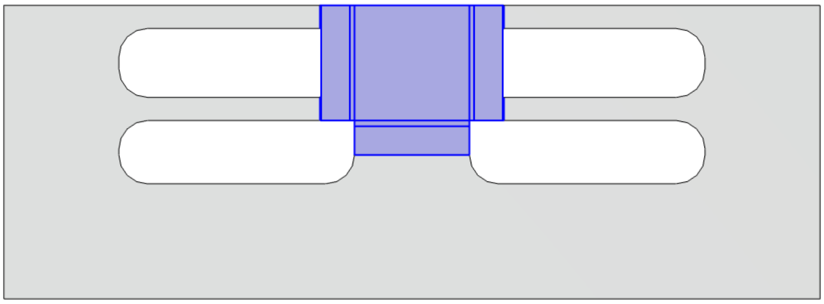

Figure F.2: Selected components in blue for the local adaptive mesh refinements

G

Finite Element Analysis model convergence results

This appendix shows the validation of convergence for each performed simulation. Figure G.1 shows the percentage error calculated between mesh refinements and it is calculated as

$$\%Error = \frac{Refinement_{i-1} - Refinement_{i}}{Refinement_{i-1}} \times 100\% \tag{G.1}$$

where i denotes the mesh refinement level and the initial mesh is indicated as mesh refinement level 0. The percentage error is calculated for the computed magnetic force on the central mover for increasing position of the left tunable mover in the range x_{TL} = [$200\,\mu\mathrm{m}$, $210\,\mu\mathrm{m}$, $220\,\mu\mathrm{m}$, $230\,\mu\mathrm{m}$, $240\,\mu\mathrm{m}$, $250\,\mu\mathrm{m}$], while varying the position x of the central mover in the range $-600\,\mu\mathrm{m}$ to $600\,\mu\mathrm{m}$ with increments of $30\,\mu\mathrm{m}$. The results clearly indicate that the percentage drops for each mesh refinement and finally reaches about 1%. Near the position of x = 0, the error increases. This can be explained by the magnetic force approaching zero, which is inevitable.

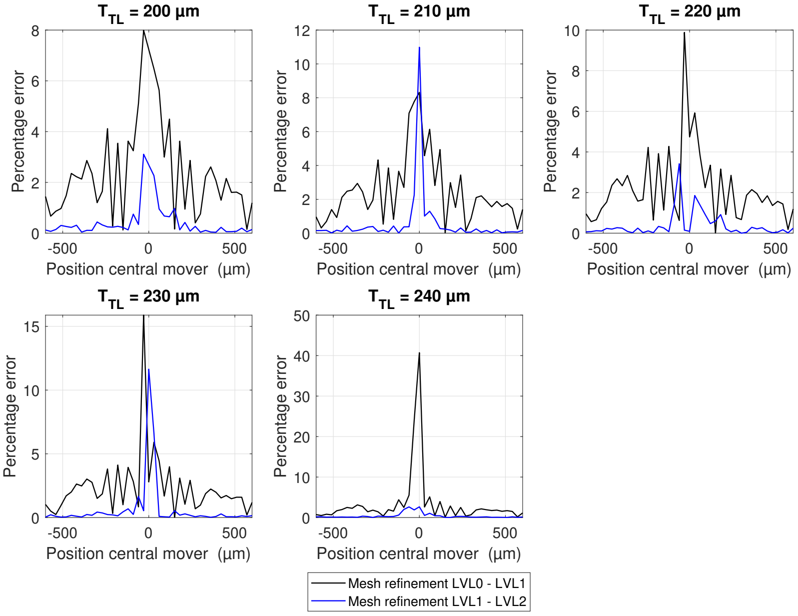

Figure G.1: Percentage error between the mesh refinements for increasing position of the left tunable mover while varying the position of the central mover

H

Magnetic saturation, flux leakage, and fringing flux

H.1. Magnetic saturation

The magnetic saturation of S235JRC+C(SH) is reported as $1.5\,\mathrm{T}$ [49]. The 3D FEA model, with the left tunable mover positioned at $T_{TL} = 240\,\mu\mathrm{m}$, is employed to validate the magnetic flux density in the stator with a reduced surface area. In Figure H.1, it is observed that when the central mover is at its center position, the magnetic flux density remains at or below $1.29\,\mathrm{T}$. In Figure H.2, with the central mover at $x = 600\,\mu\mathrm{m}$, the magnetic flux density is reaching its maximum value of $1.51\,\mathrm{T}$. This means that the magnetic saturation value in all the other simulations is lower, affirming the validity of the model.

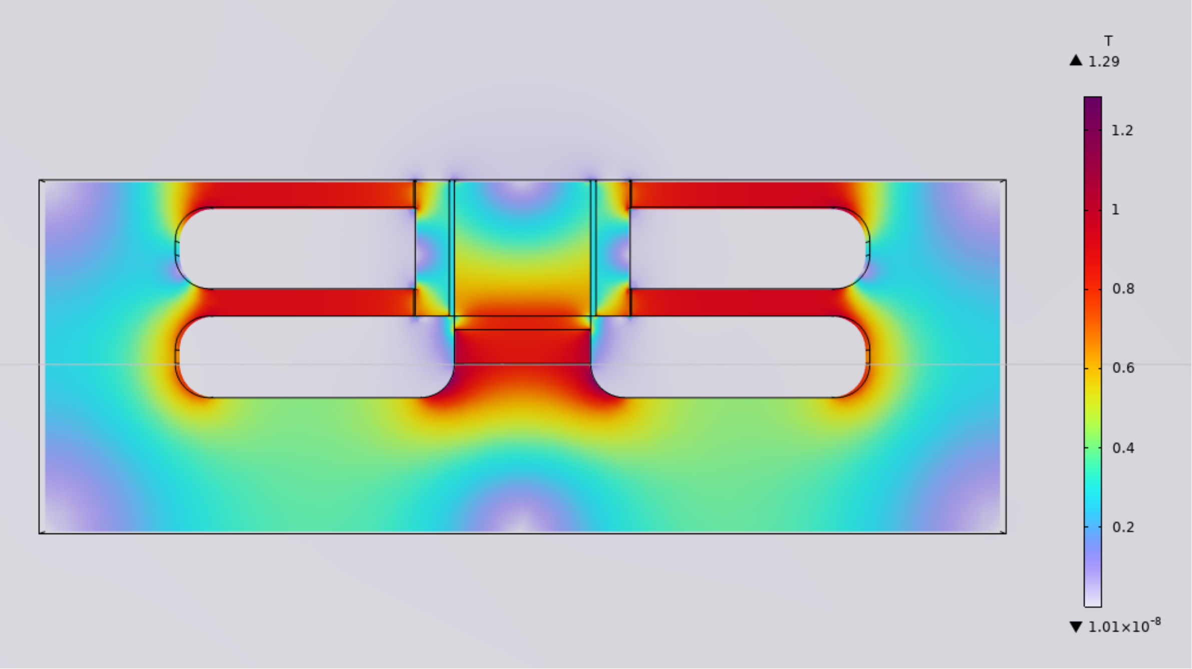

Figure H.1: The magnetic flux density in the 3D FEA model, with the left tunable mover positioned at $T_{TL} = 240\,\mu\mathrm{m}$ and the central mover is in its center position

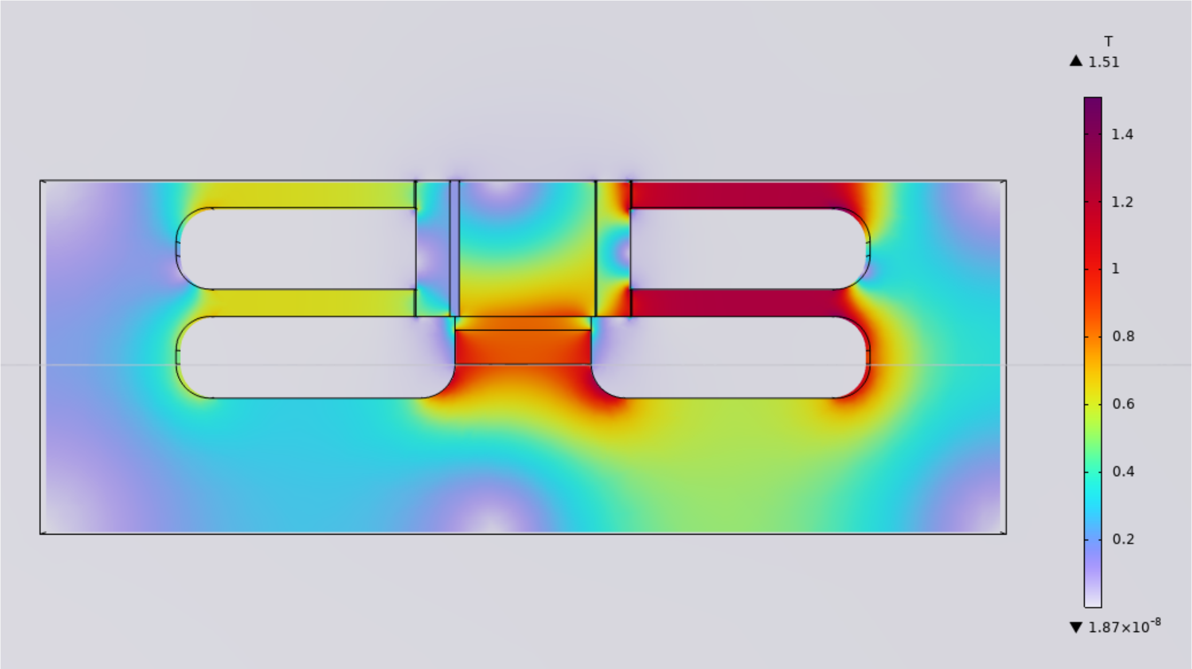

Figure H.2: The magnetic flux density in the 3D FEA model with the left tunable mover positioned at T_{TL} = $240\,\mu\mathrm{m}$ and the central mover at x = $600\,\mu\mathrm{m}$

H.2. Flux leakage

The flux leakage factor in the 3D model is determined by averaging the flux leakage of the magnet to the variable air gaps while varying the position x of the central mover in the range $-600\,\mu\mathrm{m}$ to $600\,\mu\mathrm{m}$ with increments of $30\,\mu\mathrm{m}$. The flux leakage per simulation is calculated as:

$$\lambda = \frac{-B_L A_g + B_R A_g}{B_M A_M} \tag{H.1}$$

where B_L is the average magnetic flux density in the left variable air gap, B_R is the average magnetic flux in the right variable air gap, A_g is the surface area of the variable air gaps, B_M is the average magnetic flux density in the magnet, and A_M is the surface area of the magnet. The computed flux leakage factor is 0.64.

H.3. Fringing flux

The fringing flux effect in the 3D model is depicted in Figure H.3. It is clear to see that the cross-section of the fixed air gap A_F and the tunable air gaps A_T are larger than their geometries. For this reason, these cross-sections are corrected to $A_{F,eff}$ = $530\,\mathrm{mm}^2$ and $A_{T,eff}$ = $212\,\mathrm{mm}^2$. The values of $A_{F,eff}$ and $A_{T,eff}$ are determined through an iterative process, involving a comparison between the results of the FEA model and the analytical model, aiming to minimize the difference in magnetic force on the central mover when $x = 0$.

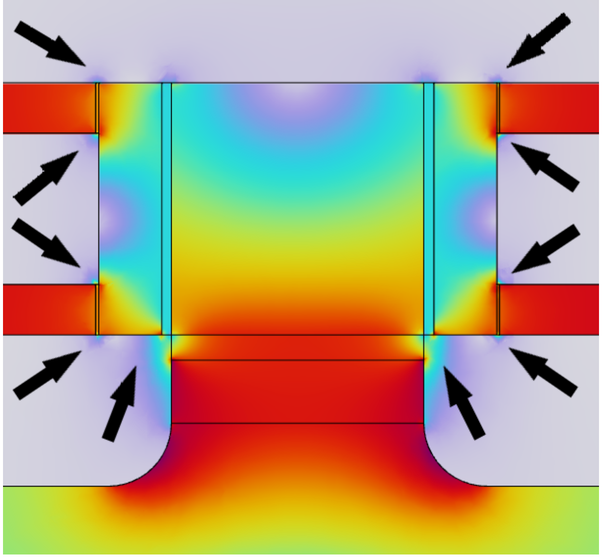

Figure H.3: Fringin flux in the 3D FEA model

I

LabVIEW model

This appendix shows the used LabVIEW block diagram and front panel for performing the experimental measurements.

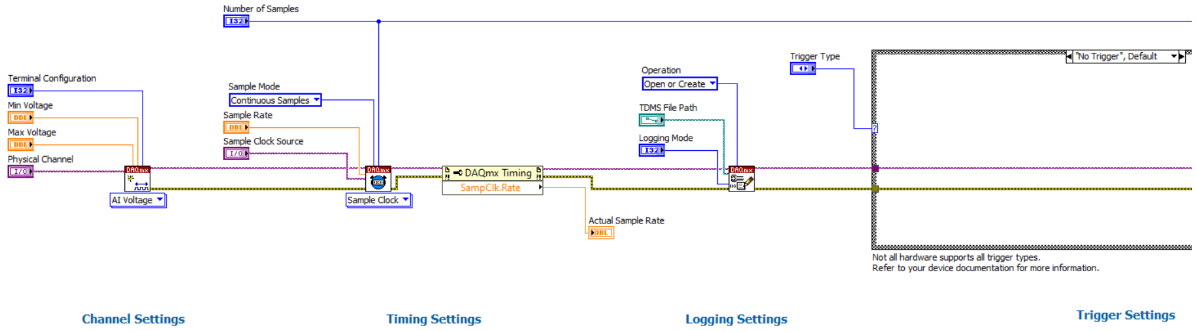

Figure I.1: The LabVIEW block diagram used for performing the experiments - part A

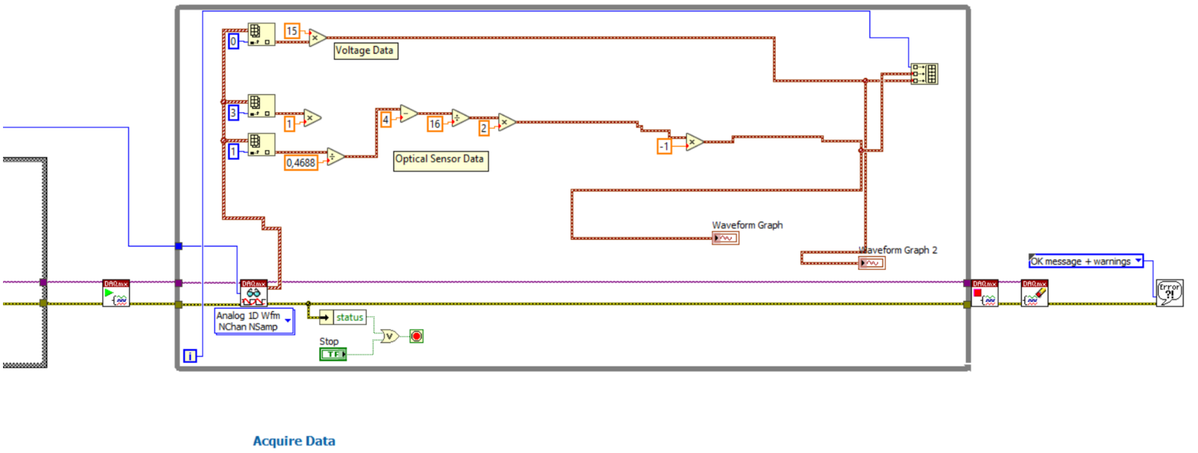

Figure I.2: The LabVIEW block diagram used for performing the experiments - part B

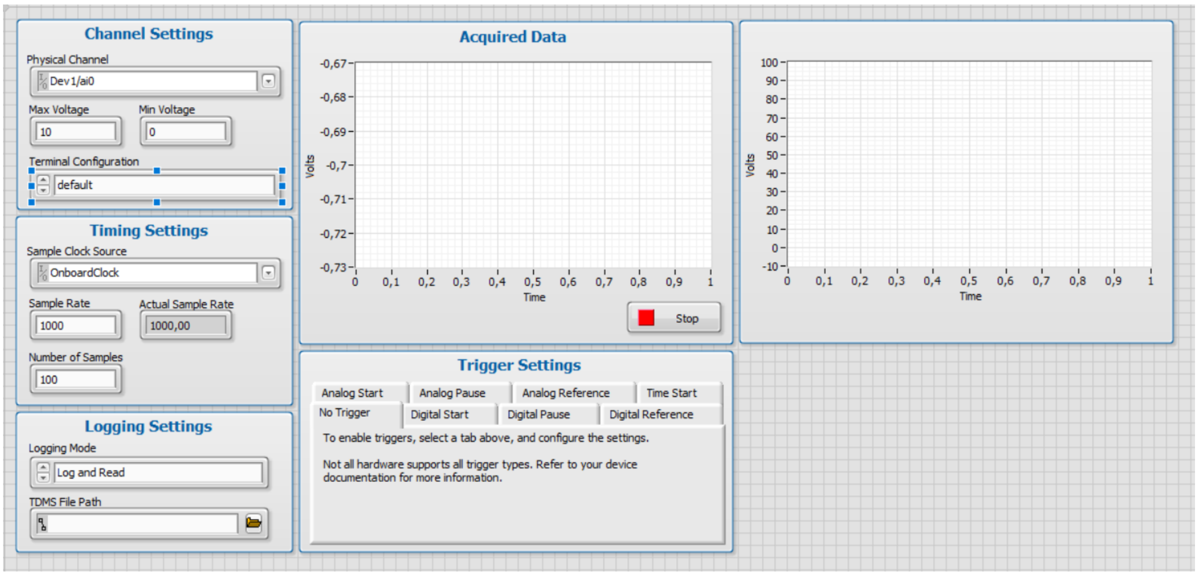

Channel Settings

Physical Channel: Dev1/ai0

Max Voltage: 10

Min Voltage: 0

Terminal Configuration: default

Timing Settings

Sample Clock Source: OnboardClock

Sample Rate: 1000

Actual Sample Rate: 1000,00

Number of Samples: 100

Logging Settings

Logging Mode: Log and Read

TDMS File Path:

Trigger Settings

To enable triggers, select a tab above, and configure the settings.

Not all hardware supports all trigger types. Refer to your device documentation for more information.

Figure I.3: The LabVIEW front panel used for performing the experiments

J

Stiffness measurement

This appendix gives an overview of how the stiffness of the central mover and tunable movers is measured.

The stiffness of the central and tunable movers is measured in the direction of the allowable motion depicted in Figure J.1a and Figure J.2a. A Futek load cell [51] is attached to a linear PI stage [52]. By displacement of the PI stage, a force F_x was measured by the load cell while measuring the displacement d_x of the PI stage. The loading and unloading of the load cell during each measurement are plotted in Figure J.1b and Figure J.2b.

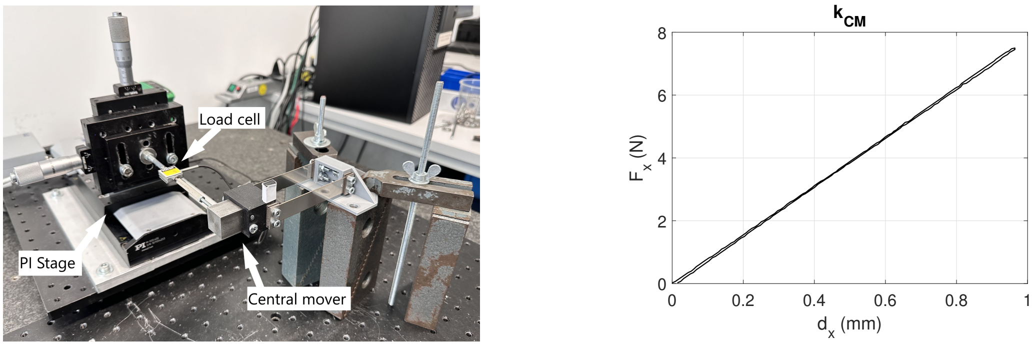

(a) Setup for measuring the stiffness of the central mover

(b) Measured stiffness of the central mover

Figure J.1: Experimental setup for measuring the stiffness of central mover

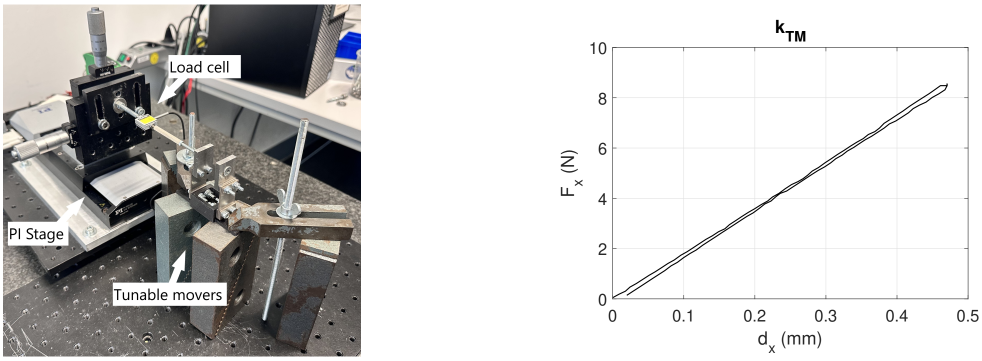

(a) Setup for measuring the stiffness of the tunable mover

(b) Measured stiffness of the tunable mover

Figure J.2: Experimental setup for measuring the stiffness of tunable movers

K

MATLAB settings and validation

This appendix gives insight into the used MATLAB settings for the estimation of the transfer functions. The estimated transfer functions are plotted over the complete measured frequency range to investigate the accuracy. Furthermore, it shows the validation for one transfer function made by MATLAB compared to a measured frequency response of the system.

K.1. MATLAB settings

The used MATLAB function to estimate the transfer functions was tfestimate. The coherence of the estimated transfer functions is verified by using the MATLAB function mscohere. Both functions need input measurement data, output measurement data, window settings, noverlap settings, frequency range, and sample rate. The used settings are shown in Table K.1

Table K.1: MATLAB settings

Denotation	Input	Comments
Window	Kaiser with $300\,000$ points and a beta of 30	To divide the data into segments
Noverlap	$180\,000$	Number of overlapped samples
Frequency range	$1\,\mathrm{Hz}$ to $500\,\mathrm{Hz}$ in $300\,000$ steps	Estimation at these frequencies
Sample rate	$5000\,\mathrm{S/s}$	Used sample rate

K.2. Complete frequency reponse

Figure K.1 show the estimated frequency responses of the system, including the complete frequency range and plotted coherence. The magnitude in the plot represents the position of the central mover in mm over the applied voltage signal in V. The plots indicates that the coherence drops significantly after approximately $100\,\mathrm{Hz}$. For this reason, it is decided that the frequency response after $100\,\mathrm{Hz}$ can not be used to accurately describe the dynamics of the system.

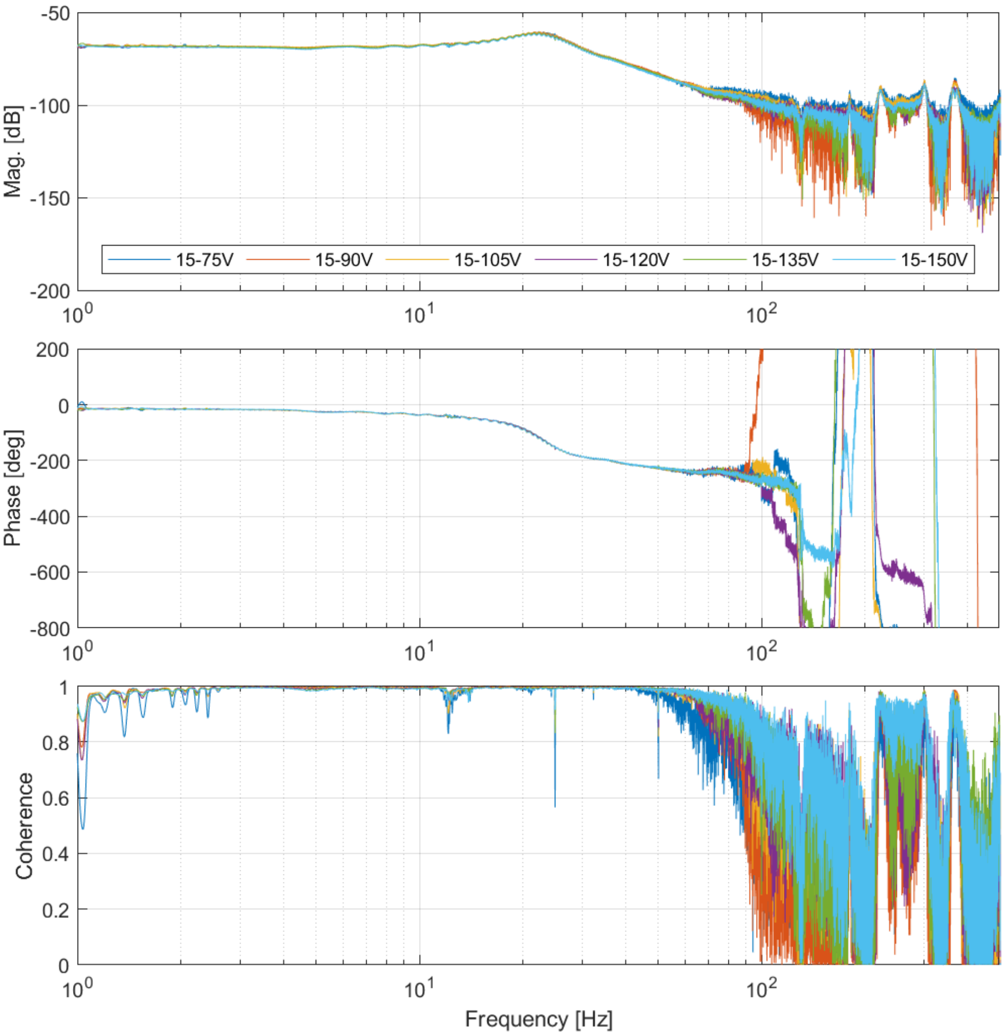

Figure K.1: The complete frequency responses of the system estimated by MATLAB for different voltage amplitudes

K.3. MATLAB validation

The gain of the transfer function estimated by MATLAB representing the $15\text{-}150\,\mathrm{V}$ signal is compared to a calculated gain based on frequency response measurement. This measurement is performed by measuring the position of the central mover x using a $15\text{-}150\,\mathrm{V}$ signal at different frequencies. The gain for each measured frequency was calculated as follows:

$$\frac{x}{V} = \frac{mean(x) - min(x)}{mean(V)} \tag{K.1}$$

Here, mean(x) denotes the average position of the central mover, calculated by averaging the measured position values over the number of samples during each frequency response. Similarly, min(x) represents the minimum position of the central mover, determined by calculating the minimum measured position values over the number of samples during each frequency response. Additionally, mean(v) signifies the average applied voltage, computed by averaging the applied voltage values over the number of samples during each frequency response.

Figure K.1 show the magnitude of the estimated transfer function by MATLAB and the calculated gain of the performed measurement. The magnitude in the plot represents the position of the central mover in mm over the applied voltage signal in V. The plot indicates that the estimated transfer function by MATLAB is highly similar to the calculated gain. For this reason, it is decided that the MATLAB tfestimate function can be used accurately to describe the frequency response of the system.

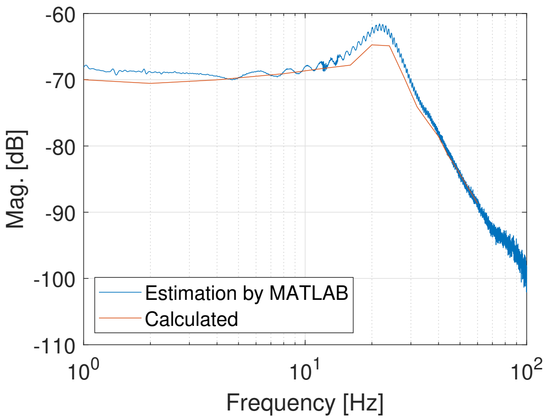

Figure K.2: Comparison of the estimated transfer function by MATLAB representing the $15\,\mathrm{V}$ to $150\,\mathrm{V}$ voltage signal to a calculated gain based on a frequency response measurement

L

PiezoDrive 150V stacked piezoelectric actuator

This appendix provides an overview of the piezoelectric actuator specifications used in the experiments.

Table L.1 shows the specifications of the used piezoelectric actuators during the experiments.

Table L.1: Specifications of the PiezoDrive SA050520 $150\,\mathrm{V}$ piezoelectric actuator [36]

Denotation	Value
Range	$31\,\mathrm{\mu m}$ ±10%
Length	$20\,\mathrm{mm}$ ±$0.05\,\mathrm{mm}$
Cross-section	$5\,\mathrm{mm}^2 \times 5\,\mathrm{mm}^2$
Capacitance	$1.8\,\mathrm{\mu F}$ ±20%
Mass	$4\,\mathrm{g}$
Blocking force	$900\,\mathrm{N}$
Stiffness	$41\,\mathrm{N/\mu m}$
Resonance frequency	$74\,\mathrm{kHz}$

According to the specifications provided by PiezoDrive, the maximum displacement d_{PZ} of the piezoelectric actuator for a specific unipolar peak-to-peak voltage is calculated as:

$$d_{PZ} = 75\% \times V_{pp} \times \frac{d_{range}}{150} \times \frac{K_{PZ}}{K_{PZ} + K_f} \pm 10\% \tag{L.1}$$

where V_{pp} is the applied peak-to-peak voltage, d_{range} is the maximum displacement range, K_{PZ}, and K_f is the stiffness of the pre-loading flexure. In the case of the PiezoDrive SA050520 piezoelectric actuator and using the $1.81 \times 10^4\,\mathrm{N/m}$ stiffness of the tunable movers, the maximum displacement is approximately 20.92 ±10%.

Bibliography

[1] A. Katalenic. *Control of reluctance actuators for high-precision positioning*. 2013. DOI: `10.6100/IR752336`. URL: `https://doi.org/10.6100/IR752336`.

[2] Philips Innovation Services. *Comparative Evaluation of Lorentz and reluctance actuators*. 2016. URL: `https://www.engineeringsolutions.philips.com/looking-expertise/high-precision-engineering/comparative-evaluation-of-lorentz-and-reluctance-actuators/`.

[3] S. Ito et al. *Long-Range Fast Nanopositioner Using Nonlinearities of Hybrid Reluctance Actuator for Energy Efficiency*. Apr. 2019, pp. 3051–3059. DOI: `10.1109/TIE.2018.2842735`.

[4] S. Ito, F. Cigarini, and G. Schitter. *Flux-Controlled Hybrid Reluctance Actuator for High-Precision Scanning Motion*. Nov. 2020, pp. 9593–9600. DOI: `10.1109/TIE.2019.2952829`.

[5] E. Csencsics et al. *Compact high performance hybrid reluctance actuated fast steering mirror system*. 2019.

[6] W.B. Hoekwater. *Design of a linearized force-flux tunable magnet actuator*. MSc Thesis, Delft University of Technology, The Netherlands, 2022.

[7] I. Mackenzie. *Design and control methods for high-accuracy variable reluctance actuators*. 2015.

[8] E.P. Furlani. *Permanent magnet and electromechanical devices: materials, analysis, and applications*. Academic Press, 2001. ISBN: 0122699513.

[9] M. Romano. *Tunable Magnets: Dynamic Flux-feedback Compensation Methods for Improved Magnetization State Tuning Performance and Minor-loop Magnetization State Tuning for the Validation and Reduction of the Break-even Tuning Interval*. MSc Thesis, Delft University of Technology, The Netherlands, 2021.

[10] A. Knaian. *Electropermanent magnetic connectors and actuators : devices and their application in programmable matter*. 2010.

[11] S.G. Viëtor. *Tunable Magnets: Modeling and Validation for Dynamic and Precision Applications*. MSc Thesis, Delft University of Technology, The Netherlands, 2018.

[12] J.D. Wiersema. *Tunable Magnet Actuators: Hysteresis Modelling for Efficient and Accurate Magnetization State Tuning*. MSc Thesis, Delft University of Technology, The Netherlands, 2022.

[13] E.P. Ronaes. *Tunable Magnet Actuators: Remnant Magnetisation State and Position Control of a Hybrid Tunable Magnet Actuator*. MSc Thesis, Delft University of Technology, The Netherlands, 2022.

[14] M. Hutter et al. *Magnetic Flux Control through Magnetic Shape Memory Alloys in Reluctance Actuators*. 2019.

[15] T. Ueno, C.S. Keat, and T. Higuchi. *Linear step motor based on magnetic force control using composite of magnetostrictive and piezoelectric materials*. 2007, pp. 11–14. DOI: `10.1109/TMAG.2006.886402`.

[16] R. Holland. *Representation of Dielectric, Elastic, and Piezoelectric Losses by Complex Coefficients*. 1967, pp. 18–20. DOI: `10.1109/T-SU.1967.29405`.

[17] M. Wild et al. *The challenge of distinguishing mechanical, electrical and piezoelectric losses*. Oct. 2018, pp. 2128–2134. DOI: `10.1121/1.5057443`.

[18] M. Wild et al. *Comparison of Two Models for Power Dissipation and Temperature in Piezoelectric Transducers*. 2018.

[19] P.A. Tipler and G. Mosca. *Physics for Scientists and Engineers*. 2008.

[20] J.R. Brauer. *Magnetic Actuators and Sensors*. 2014.

[21] X. Zhang et al. *Hysteresis and magnetic flux leakage of long stroke micro/nanopositioning electromagnetic actuator based on Maxwell normal stress*. May 2022, pp. 1–11. DOI: `10.1016/j.precisioneng.2022.01.003`.

[22] S. Zurek. *Encyclopedia Magnetica*. Dec. 2022. URL: `https://e-magnetica.pl/flux_fringing`. accessed: 26.1.2023.

[23] G. Stadler et al. *High Precision Hybrid Reluctance Actuator With Integrated Orientation Independent Zero Power Gravity Compensation*. 2022, pp. 13296–13304. DOI: `10.1109/TIE.2021.3137444`.

[24] F. Cigarini et al. *Compensation of hysteresis in hybrid reluctance actuator for high-precision motion*. 2019, pp. 477–482. DOI: `10.1016/j.ifacol.2019.11.721`.

[25] R. Munnig Schmidt et al. *The Design of High-Performance Mechatronics*. IOS Press, 2020. ISBN: 9781643680507.

[26] S.J. Murray et al. *6% magnetic-field-induced strain by twin-boundary motion in ferromagnetic Ni-Mn-Ga*. Aug. 2000, pp. 886–888. DOI: `10.1063/1.1306635`.

[27] Y. K. Yong. *Preloading Piezoelectric Stack Actuators in High-Speed Nanopositioning Systems*. Oct. 2016. DOI: `10.3389/fmech.2016.00008`.

[28] Physik Instrumente. *P-603 Inexpensive PiezoMove Linear Actuator*. 2023. URL: `https://www.physikinstrumente.com/en/products/linear-actuators/piezomove-lever-actuators/p-603-inexpensive-piezomove-linear-actuator-202800`.

[29] Thorlabs. *Discrete Piezoelectric Stacks, 5.2 µm to 100.0 µm Travel*. 2023. URL: `https://www.thorlabs.com/newgrouppage9.cfm?objectgroup_id=8040`.

[30] S. Kuiper et al. *Electromagnetic deformable mirror development at TNO*. July 2016, p. 991204. DOI: `10.1117/12.2230891`.

[31] Thorlabs. *Piezoelectric Tutorial: Piezoelectric Basic Background and Operation Tutorial*. 2023. URL: `https://www.thorlabs.com/newgrouppage9.cfm?objectgroup_id=5030`.

[32] Physik Instrumente. *Electrical Operation of Piezo Actuators*. 2023. URL: `https://www.piceramic.com/en/expertise/piezo-technology/properties-piezo-actuators/electrical-operation`.

[33] COMSOL. *Simulate real-world designs, devices, and processes with multiphysics software from COMSOL*. URL: `https://www.comsol.com`.

[34] Ijzershop. *Steel S235JRC+C(SH)*. 2023. URL: `https://ijzershop.nl/blank-vierkant/1177-1028-stalen-blank-vierkant-20-x-20mm-lengte-1000mm.html`.

[35] Supermagnete. *Data sheet article Q-20-20-05-N: Technical data and application safety*. 2023. URL: `https://www.supermagnete.nl/eng/data_sheet_Q-20-20-05-N.pdf`.

[36] PiezoDrive. *150V Piezo Stack Actuators*. 2023. URL: `https://www.piezodrive.com/actuators/150v-piezo-stack-actuators-2/`.

[37] Thorlabs. *25 mm Optical Construction Rails*. 2023. URL: `https://www.thorlabs.com/newgrouppage9.cfm?objectgroup_id=194`.

[38] Micro-Epsilon Measurement Technology. *optoNCDT 2300*. 2023. URL: `https://www.micro-epsilon.com/displacement-position-sensors/laser-sensor/optoNCDT_2300_basic/`.

[39] RS Pro. *RS PRO Arbitrary Waveform Generator, 30MHz Max, 0 MHz Min*. URL: `https://uk.rs-online.com/web/p/arbitrary-waveform-generators/1236459`.

[40] Thorlabs. *High-Voltage Piezo Amplifier*. 2023. URL: `https://www.thorlabs.com/newgrouppage9.cfm?objectgroup_id=13630`.

[41] National Instruments. *USB-6008: Multifunction I/O Device*. 2023. URL: `https://www.ni.com/nl-nl/support/model.usb-6008.html`.

[42] National Instruments. *What Is LabVIEW?* 2023. URL: `https://www.ni.com/nl/shop/labview.html`.

[43] MathWorks. *Math. Graphics. Programming*. 2023. URL: `https://nl.mathworks.com/products/matlab.html`.

[44] Olivier Geoffroy et al. *Practical and theoretical investigations of a rotating coilless actuator using the inverse magnetostrictive effect*. 2010, pp. 606–609. DOI: `10.1109/TMAG.2009.2034469`.

[45] Junwei Cui, Liyan Qu, and Wei Qiao. *A Single-Phase Electromagnetic Transformer with an Adjustable Output Voltage*. 2019.

[46] Junwei Cui, Liyan Qu, and Wei Qiao. *A Three-Phase Adjustable-Voltage-Ratio Transformer Based on Magnetic Flux Valves*. 2018.

[47] Haosen Wang, Liyan Qu, and Wei Qiao. *Adjustable-Voltage-Ratio Magneto-Electric Transformer*. 2015. DOI: `10.1109/LMAG.2015.2477483`.

[48] Junwei Cui et al. *A Tunable Inductor Based on a Magnetic Flux Valve*. 2017.

[49] M. Flankl. *Electrodynamic Energy Harvesting from Moving Conductive Surfaces*. 2018. URL: `http://www.pes.ee.ethz.ch`.

[50] M. Seher and P.B. Nagy. *On the separation of Lorentz and magnetization forces in the transduction mechanism of Electromagnetic Acoustic Transducers (EMATs)*. Dec. 2016, pp. 1–10. DOI: `10.1016/j.ndteint.2016.07.001`.

[51] Futek. *Load Cells and Force Sensors*. 2023. URL: `https://www.futek.com/store/load-cells`.

[52] Physik Instrumente. *Stages with Magnetic Direct-Drive Linear Motor*. 2023. URL: `https://www.physikinstrumente.com/en/products/linear-stages/stages-with-magnetic-direct-drive-linear-motor`.